



HAL
open science

Color characterization of a new laser printing system

Juan Manuel Martinez Garcia

► **To cite this version:**

Juan Manuel Martinez Garcia. Color characterization of a new laser printing system. Image Processing [eess.IV]. Université de Lyon, 2016. English. NNT : 2016LYSES032 . tel-01907849

HAL Id: tel-01907849

<https://theses.hal.science/tel-01907849>

Submitted on 29 Oct 2018

HAL is a multi-disciplinary open access archive for the deposit and dissemination of scientific research documents, whether they are published or not. The documents may come from teaching and research institutions in France or abroad, or from public or private research centers.

L'archive ouverte pluridisciplinaire **HAL**, est destinée au dépôt et à la diffusion de documents scientifiques de niveau recherche, publiés ou non, émanant des établissements d'enseignement et de recherche français ou étrangers, des laboratoires publics ou privés.



Thèse

**COLOR CHARACTERIZATION OF A NEW
LASER PRINTING SYSTEM
CARACTÉRISATION DES COULEURS D'UN
NOUVEAU SYSTÈME D'IMPRESSION LASER**

Présentée le 16 Septembre 2016

à l'École Doctorale ED488 Science Ingénierie Santé

Programme doctoral en Image Vision Optique

Faculté des Sciences et Techniques

Pour l'obtention du grade de

DOCTEUR DE L'UNIVERSITÉ JEAN MONNET par

Juan Manuel MARTINEZ GARCIA

Mme. Clotilde BOUST, Chef du département d'imagerie à « Centre de recherche et de restauration des musées de France (C2RMF) », examinatrice

M. Jon Yngve HARDEBERG, Professeur à « Norwegian University of Science and Technology », rapporteur

M. Manuel MELGOSA, Professeur à « Universidad de Granada », rapporteur

M. Alain TREMEAU, Professeur à « Université Jean Monnet », directeur de thèse

M. Mathieu HEBERT, Maître de Conférences à « Université Jean Monnet »,
co-encadrant

Laboratoire Hubert Curien UMR-CNRS 5516

Saint-Etienne, 2016



ACKNOWLEDGMENTS

First of all, I would like to thank my supervisors Alain Trémeau and Mathieu Hébert, for their guidance and unconditional support during these last three years. Alain and Mathieu's professional and personal qualities allowed me to pursue my objectives with determination as well as enthusiasm.

I want to thank all the member of the PHOTOFLEX project who directly or indirectly contributed to the results I could obtain, especially:

- Nicolas Crespo-Monteiro, for his repeated help with the printing of the samples I used for my characterizations
- Francis Vocanson, for his help with the elaboration of all the printing supports I used for my experiments
- Anthony Cazier, for his help and advice with the several optical setups we assembled for the measurement of different kinds of samples
- Renée Charrière, for her help regarding camera calibration and with several other experiments, and
- Nathalie Destouches for her valuable input during the different discussions about the project.

I also want to thank all the other members who made possible the production and printing of the PICSLUP samples, with whom I didn't get the chance to work directly but without whom none of my research goals could have been achieved.

I am also very grateful to the jury members Jon Hardeberg and Manuel Melgosa for the time they spent reading my manuscript and for they valuable and constructive suggestions, and also Clotilde Boust for her insightful questions during the defense.

Finally, I want to thank Thomas Houllier and Hayk Yepremian for their help with the preparation and measurements using the hyperspectral imaging system.

This work was supported by the French National Research Agency (ANR) within the program "Investissements d'Avenir" (ANR-11-IDEX-0007), in the framework of project PHOTOFLEX n°ANR-12-NANO-0006 and the LABEX MANUTECH-SISE (ANR-10-LABX-0075) of Université de Lyon.

ABSTRACT

Recent progresses in nanotechnologies enabled the coloration of glass plates coated with titanium dioxide containing silver by laser irradiation. The colored samples display very different colors when obtained by reflection or transmission of light; in specular or off-specular directions; and with or without polarizing filters. This new laser printing technology, that we call PICSLUP (for Photo-Induced Colored Silver LUster Printing system), enables the production of gonioapparent color images.

The goal of this study is to perform a multi-geometry photometric and color characterization of this complex system. This task posed technical challenges due to the system being in a development stage, especially a low availability of the printing material; and due to the photometric properties of the prints: high translucency, high specularity and strong goniochromaticity.

In order to overcome these constraints, our first approach was based on color characterization by microscope imaging. The data set used consisted in printing an exhaustive number of micrometric color patches, produced by varying the different laser printing parameters: exposure time, laser wavelength, laser power, and laser focusing distance. To achieve accurate color measurements with samples produced with the PICSLUS system, we successfully developed a color calibration method especially tailored for highly specular materials, whose accuracy is good in comparison to previous studies in the literature on camera color calibration. From the colors obtained, we could estimate the color gamut in the $0^\circ:0^\circ$ specular reflection geometry and study the influence of the different printing parameters as well as polarization.

Although the measurements with microscope imaging in the $0^\circ:0^\circ$ specular geometry were very useful to study the properties of the colors produced by the PICSLUP technology, they were not sufficient to fully characterize the system, since the samples exhibit very different colors according to the respective positions of the viewer and the light source. With this in mind, we assembled a geometry-adjustable hyperspectral imaging system, which allowed us to characterize a representative subset of the colors that can be produced with the system. The samples were measured from both recto and verso faces, in the $0^\circ:0^\circ$ transmission, $15^\circ:15^\circ$ specular reflection, and $45^\circ:0^\circ$ off-specular reflection illumination/observation geometries. From these measurements, the color gamuts of the system were estimated in the different geometries. The volumes delimited by the colors obtained were concave and contained many sparse regions with very few samples. In order to obtain more continuous, dense and convex color gamut volumes, we successfully tested the generation of new colors by juxtaposing printed lines of different primaries with halftoning techniques.

In order to circumvent the need to physically characterize all the different color that can be produced with halftoning using the numerous primaries available, we also tested and fitted existing halftoning prediction models, and obtained a satisfactory accuracy. The use of halftoning not only increased the number colors that can be produced by the system in the different geometries, but also increased the number of different primaries that can be produced when we consider as a whole the set of colors produced by the same printed patch in multiple geometries.

Finally, based on the different properties demonstrated by the samples produced by the PISCLUP system, we explored some imaging and security features with colors obtained from our characterization, and propose further potential applications for this new goniochromatic laser printing technology.

RÉSUMÉ

Grâce aux progrès récents dans le domaine des nanotechnologies il est maintenant possible de colorer des plaques de verre avec du dioxyde de titane contenant de l'argent par irradiation laser. L'une des caractéristiques de ce procédé est que le rendu couleur des échantillons produits diffère quand ceux-ci sont observés en réflexion (spéculaire ou diffuse) ou en transmission, ainsi que quand on polarise la lumière. Ce nouveau procédé d'impression laser que l'on a appelé PICSLUP (pour Photo-Induced Colored Silver LUster Printing system) permet de produire des images couleur gonio-apparentes.

L'objectif de cette thèse est de caractériser l'apparence couleur (d'un point de vue colorimétrique et photométrique, et ce selon plusieurs géométries d'observation) de plaques de verre colorées par ce procédé. Ce qui pose de nombreux challenges techniques du fait que le système d'impression utilisé est encore en cours de développement et pas souvent accessible, du fait également de plusieurs spécificités photométriques (surface fortement translucide, fortement spéculaire, forte gonio-chromaticité). Afin de lever de toutes ces contraintes techniques notre première approche a été de caractériser la couleur grâce à un imageur monté sur un microscope. Nous avons pour cela généré par impression laser (avec le système PICSLUS) tout un ensemble d'échantillons couleur en faisant varier de manière exhaustive différents paramètres d'impression (temps d'exposition du faisceau laser, longueur d'onde, distance focale). Afin d'obtenir des mesures couleur précises nous avons ensuite développé une méthode de calibrage couleur spécifique dédiée à la mesure de surfaces fortement spéculaires. La précision de cette méthode de calibrage, appliquée aux échantillons créés par le système PICSLUP, est comparable à celles relevées dans l'état de l'art.

À partir des couleurs obtenues on peut estimer la gamme des couleur (color gamut) qui peut être obtenue par ce système d'impression, en particulier pour la géométrie spéculaires $0^\circ:0^\circ$, et étudier l'influence des différents paramètres d'impression ainsi que l'effet de la polarisation. Quoique les mesures réalisées sous microscope avec la géométrie spéculaire $0^\circ:0^\circ$ soient particulièrement utile pour étudier les propriétés colorimétriques et photométriques produites par le système PICSLUP, ces mesures ne sont pas suffisantes pour caractériser complètement ce système. En effet, l'apparence couleur des échantillons produits varie également en fonction de la géométrie d'éclairage et d'observation, il est donc nécessaire de caractériser le système PICSLUP selon d'autres géométries que la seule géométrie $0^\circ:0^\circ$. Nous avons donc développé une autre méthode de caractérisation basée sur l'utilisation d'un imageur hyperspectral à géométrie ajustable, ce qui nous a permis de caractériser un ensemble donné d'échantillons couleur produits par le système PICSLUP. Ces échantillons ont été

mesurés, en recto-verso, en transmission (avec la géométrie $0^{\circ}:0^{\circ}$), en réflexion spéculaire (avec la géométrie $15^{\circ}:15^{\circ}$), et en réflexion hors spéculaire (avec la géométrie $45^{\circ}:0^{\circ}$).

Grâce à ces mesures on a pu estimer pour différentes géométries d'observation les changements de gamme des couleurs qui peuvent être obtenus par le système PICSLUP. Le volume qui circonscrit chacune de ces gammes de couleur peut être modélisé par une forme concave qui contient beaucoup de zones éparses, ce qui revient à dire que certaines couleurs ne peuvent être directement obtenues par impression. Afin d'obtenir une forme convexe, plus dense quelque soit la zone d'étude considérée, nous avons testé avec succès une nouvelle méthode d'impression qui consiste non plus à imprimer des aplats (zones uniformément colorées par juxtaposition de lignes laser identiques) mais à imprimer des demi-tons (par juxtaposition de lignes laser de différentes couleurs). Cette méthode est basée sur le principe de l'halftoning et sur un nombre limité de primaires couleur pré-sélectionnées.

TABLE OF CONTENTS

ACKNOWLEDGMENTS	3
ABSTRACT	5
RÉSUMÉ.....	7
LIST OF FIGURES	13
LIST OF TABLES	21
RÉSUMÉ DES CHAPITRES	23
1 INTRODUCTION.....	25
1.1 PICSLUP TECHNOLOGY	26
1.2 OUTLINE	28
1.3 PUBLICATIONS	29
2 COLOR SCIENCE FUNDAMENTALS.....	31
2.1 WHAT IS COLOR?.....	31
2.2 LIGHT.....	32
2.3 INTERACTION BETWEEN LIGHT AND SURFACES.....	33
2.4 PHOTOMETRY OF SURFACES	34
2.5 HUMAN VISUAL SYSTEM.....	35
2.6 COLOR ATTRIBUTES	36
2.7 COLORIMETRY	36
2.7.1 <i>The 2° CIE RGB system</i>	37
2.7.2 <i>The 2° CIE XYZ system</i>	39
2.7.3 <i>XYZ tristimulus values of materials</i>	40
2.7.4 <i>Chromaticity diagram</i>	41
2.8 UNIFORM COLOR SPACES.....	42
2.8.1 <i>The CIE 1976 UCS chromaticity diagram</i>	43
2.8.2 <i>The CIELAB color space</i>	43
2.9 COLOR DIFFERENCE EVALUATION	44
2.10 THE sRGB COLOR SPACE	46

2.10.1 Transformation from XYZ to sRGB	46
2.11 LIMITATIONS OF COLORIMETRY	47
2.12 CONCLUSION.....	49
3 PHOTOMETRIC CHARACTERIZATION OF THE PICSLUP TECHNOLOGY.....	51
3.1 SAMPLE PRODUCTION CONSTRAINTS	51
3.2 OPTICAL MEASUREMENT CONSTRAINTS	53
3.2.1 High specularity.....	53
3.2.2 Gonioappearance.....	54
3.2.3 Size of samples.....	55
3.3 CONVENTIONAL MEASUREMENT STRATEGIES.....	55
3.4 CONCLUSION.....	56
4 COLOR CHARACTERIZATION BY MICROSCOPE CAMERA.....	57
4.1 MICROSCOPE CAMERA COLOR CALIBRATION.....	57
4.2 MICROSCOPE PRINTING AND IMAGING SYSTEM	59
4.3 SAMPLES USED FOR THE CALIBRATION	60
4.4 GROUND TRUTH COLORS OF CALIBRATION SETS.....	61
4.5 EXTRACTION OF MEASURED COLORS FROM CAMERA IMAGES.....	62
4.6 COLOR TRANSFORMATION	63
4.6.1 Polynomial transformation.....	64
4.6.2 Applying the color calibration.....	65
4.7 COLOR CALIBRATION METHODS	65
4.7.1 Adjustment of exposure time and color channel gains	66
4.7.2 Ground truth measurement.....	66
4.7.3 First method: Diffuse learning set and exposure time decrease	66
4.7.4 Second method: Diffuse learning set and lamp power decrease	67
4.7.5 Third method: Specular learning set	67
4.7.6 Fourth method: Optical bench with $0^\circ:0^\circ$ geometry	67
4.8 COLOR CALIBRATION RESULTS.....	68
4.8.1 Influence of the polynomial order.....	70
4.8.2 Influence of the color temperature of the illuminant	70
4.9 CONCLUSION ON COLOR CALIBRATION.....	71
4.10 EXTRACTION OF COLOR INFORMATION FROM CALIBRATED IMAGES	72

4.11 COLOR GAMUT IN THE 0°:0° SPECULAR REFLECTION GEOMETRY	74
4.12 INFLUENCE OF POLARIZATION AND PRINTING PARAMETERS	74
4.13 CONCLUSION	77
5 CHARACTERIZATION BY HYPERSPECTRAL IMAGING.....	79
5.1 HYPERSPECTRAL IMAGING SETUP.....	79
5.2 EXPOSURE TIME AND WHITE REFERENCE	80
5.3 HYPERSPECTRAL IMAGES IN TRANSMISSION.....	81
5.4 HYPERSPECTRAL IMAGES IN SPECULAR REFLECTION.....	82
5.5 HYPERSPECTRAL IMAGES IN OFF-SPECULAR REFLECTION.....	83
5.6 IMAGE REGISTRATION OF NARROWBAND-FILTER IMAGES.....	85
5.7 COLOR VISUALIZATION OF HYPERSPECTRAL IMAGES	88
5.8 EXTRACTION OF SPECTRAL INFORMATION FROM PRINTED AREAS.....	89
5.9 PRACTICAL ASPECTS OF THE HYPERSPECTRAL IMAGING SYSTEM	91
5.10 CONCLUSION.....	92
6 COLOR GAMUT AND EXTENSION BY HALFTONING.....	93
6.1 PICS LUP COLOR GAMUT ESTIMATION.....	93
6.2 MULTIPLE COLORS DISPLAYED BY A SINGLE PATCH	97
6.3 HALFTONING.....	99
6.4 FIRST EXPERIMENTS WITH HALFTONE SAMPLES.....	100
6.5 ADVANCED EXPERIMENTS WITH HALFTONE SAMPLES	103
6.5.1 Selection of halftoning primaries.....	103
6.5.2 Halftone samples.....	104
6.5.3 Measurement configurations and spectral predictions.....	105
6.6 COLOR GAMUT EXTENSION BY USING HALFTONING.....	108
6.7 CONCLUSION.....	111
7 CONCLUSIONS AND FUTURE WORK	113
7.1 PRINTING SPECIAL EFFECT IMAGES	114
7.2 FUTURE WORK.....	118
7.3 POTENTIAL APPLICATIONS.....	120
APPENDIX 1: FILM ELABORATION AND PRINTING.....	123
APPENDIX 2: CALCULATION OF RGB TO XYZ TRANSFORMATION MATRICES	125
BIBLIOGRAPHY	127

LIST OF FIGURES

Figure 1.1: Lycurgus cup by reflection (left) and transmission (right) of light.	25
Figure 1.2 Optical scheme of the PICLSUP system used for microscopic laser inscription and imaging.	26
Figure 1.3: Image of the same area from a printed sample at different scales made by scanning electron microscopy where the nanoparticles are well aligned.	27
Figure 1.4: Microscope images of areas printed with varying laser focuses on the horizontal direction (100 μm period), and varying translation speeds on the vertical direction (50 μm period).	28
Figure 1.5: Sample printed with the PICSLUP system, observed from two different directions under the same illumination conditions. The colors of the squared areas (printed with different laser settings) change dramatically depending on the illumination/observation geometries or whether a polarizer is used.	28
Figure 2.1: The electromagnetic spectrum.	32
Figure 2.2: Relative spectral power distribution of typical daylight given by the standard illuminant D65.	32
Figure 2.3: Relative spectral sensitivity of the S, M and L cones, according to Stockman et. al. ³¹	36
Figure 2.4: RGB color matching functions for the 2° CIE Standard Observer, obtained from the average of 17 observers matching each wavelength by modulating the three CIE RGB primaries assessed with a 2° field of view. ³⁶	38
Figure 2.5: XYZ color matching functions for the 2° CIE Standard Observer, obtained from a mathematical linear transformation applied to the CIE RGB system.	39
Figure 2.6: Comparison between the \bar{y} color matching function and the photopic luminous efficacy function $V(\lambda)$. ³⁰	40
Figure 2.7: Chromaticity diagram of the CIE XYZ color specification system. The wavelengths of the monochromatic lights used to generate the spectrum locus are shown within the curve.	42
Figure 2.8: Ellipses representing the average just noticeable color differences (JND) obtained by David MacAdam ⁴⁰ in 1942. For clarity, the ellipses are depicted at 10 times their size.	42

- Figure 2.9: Example of simultaneous contrast. The small squares in the centers have the same color but the one on the left appears to be brighter than the one on the right. 47
- Figure 2.10: Example of simultaneous contrast. The perceived vertical rectangles were made using the same color, yet the one on the left appears to be brighter than the one on the right. 48
- Figure 3.1: Glass support coated with the TiO₂ printable material, after been printed several times with different laser settings. Each of the squares in the grid have an area of 2 mm × 2mm. 52
- Figure 3.2: Microscopic image of a sample printed by the PICSLUP system..... 53
- Figure 3.3: BRDF in the incidence plane of four different materials, where θ_i is the incident angle of light with respect to the normal of the surface. The curves represent the relative amount of light reflected in every direction in the incidence plane, the incident direction of light being shown by the dashed line. (a) Perfectly diffusing material, (b) Perfectly specular material, (c) Roughened metal, and (d) Very glossy paper. (Image used with permission of Mathieu Hébert).⁶² 54
- Figure 3.4: Sample printed with the PICSLUP system, observed from two different directions under the same illumination conditions. The colors are normalized according to a calibrated mirror. 54
- Figure 3.5: X-rite Color i7® (left) X-rite i1 Pro® (right) spectrophotometers used for reflection and transmission measurements in specific geometries. 56
- Figure 3.6: STIL REFLET® gonio-spectrophotometer..... 56
- Figure 4.1: Example of materials with different specularities. 58
- Figure 4.2: Simplified illustration of the reflective components of materials. Diffuse materials have a large diffuse component and a small specular component, whereas specular materials have a strong specular component and a very small diffuse component. 59
- Figure 4.3: Optical scheme of the PICSLUP system used for microscopic laser inscription and imaging..... 60
- Figure 4.4: Diffuse/matte (left) and specular (right) calibration samples. 60
- Figure 4.5: Color sample sets used in this study displayed in the CIE Chromaticity diagram (left) and in the a*-b* plane of the CIELAB color space (right). The CIELAB L* values of the samples range from 22.2 to 96.4 units. For clarity, the illuminant used for these plots was D65. 61
- Figure 4.6: (a) Non-uniform irradiance on a sample from the learning set consisting of a ROSCO green filter on top of the calibrated mirror. (b) Area considered for the average color extraction of the samples in the learning set consisting of ROSCO color filters on top of the calibrated mirror. The area corresponds to pixels with color difference lower than 5 CIE94 units with respect to the pixel with the highest CIELAB L* value. 63

Figure 4.7: Optical setup based on the $0^{\circ}:0^{\circ}$ geometry used to obtain the spectral measurements of the samples in order to obtain the ground truth color values with the fourth method.	68
Figure 4.8: Average calibration results regarding the testing set, by assuming different color temperatures of a black body illuminant with the third and fourth calibration methods.	71
Figure 4.9: Microscope images containing 4 rows and 5 columns of printed lines for a total of 20 different combinations of laser parameters per image.	72
Figure 4.10: Different stages in the color extraction from one of the lines in the left image of Figure 4.9. (a) Step 1: Image cropped around the target line. (b) Step 2: Image blurred to reduce noise. (c) Steps 3 to 9: Different steps to separate the line from the background. (d) Step 10: Pixels to be extracted and average from the original image.	73
Figure 4.11: Colors obtained with a controlled combination of elaboration parameters, and measured by a color-calibrated microscope in the $0^{\circ}:0^{\circ}$ illumination/observation geometry. The colors are represented in the CIELAB color space by assuming a D65 illuminant. The reference colors in the background of the left image were calculated by fixing a lightness value L^* of 50 units.	74
Figure 4.12: Color gamut of the PICSLUP system in the $0^{\circ}:0^{\circ}$ geometry (red) compared to the color gamut of two typical printing systems (blue): (a,b) offset printer, and (c,d) inkjet printer. The reference colors in the background of the plots were calculated with a D65 illuminant and a lightness value L^* of 50 units.	75
Figure 4.13: Color variation in the CIELAB a^*b^* -plane of 9 different samples observed in the $0^{\circ}:0^{\circ}$ geometry, when rotating a polarizer between 0° and 180° . In each curve, 0° and 90° correspond to the left and right extrema, respectively.	75
Figure 4.14: Color change in the CIELAB a^*b^* -plane of PICSLUP prints as a function of wavelength (one wavelength λ per row), focusing conditions (the same focusing on each column), and speed (varies in each CIELAB a^*b^* -plane), for TE (red curve) and TM (blue curve) polarizations.	76
Figure 5.1: Scheme of the hyperspectral imaging system.	80
Figure 5.2: Spectral transmittances of the 31 interferential bandpass filters.	80
Figure 5.3: Scheme of the hyperspectral imaging system for the measurement of samples in transmission mode	81
Figure 5.4: Images of a sample printed by the PICSLUP system (c,d) and images obtained with no sample placed in the holder (b,d), obtained with the intensity camera in transmission mode by using different filters: 460 nm (a,b), and 600 nm (c,d).	82
Figure 5.5: Scheme of the hyperspectral imaging system for the measurement of samples in specular reflection mode	82

- Figure 5.6: Image of a sample printed by the PICSLUP system (left) and of the white reference used (right), obtained in specular reflection mode by using the 470 nm filter..... 83
- Figure 5.7: Scheme of the hyperspectral imaging system for the measurement of samples in off-specular reflection mode 84
- Figure 5.8: (Left) Image in off-specular reflection of sample printed with the PICSLUP system with many different laser parameter combinations. (Right) Illustration of a typical spectral reflectance of PICSLUP samples in off-specular reflection, and the reflectance of the white reference used..... 84
- Figure 5.9: Image of a sample printed by the PICSLUP system (left) and of the white reference used (right), obtained in off-specular reflection mode by using the 580 nm filter..... 85
- Figure 5.10: Images obtained by the hyperspectral system in transmission mode by using the 400 nm filter (a) and the 420 nm filter (b). Both images are combined in image (c) to highlight their misalignment. 86
- Figure 5.11: Example of images aligned by using our image registration method. The images on the left correspond to the reference used for the registration, the ones on the center correspond to the current image being registered, and the ones on the right to the comparison of both images in each stage of the process. (a) Original images used as input. (b) Edge detection and dilation. (c) Holes in images are filled. (d) Remove small objects. (e) Obtain and apply the image registration transformation. (f) Final registered image..... 87
- Figure 5.12: sRGB color images rendered from the hyperspectral images obtained from two different samples (a, b) in three different measurement geometries. The white defects in the specular reflection images are discussed in Section 5.8. The areas of the squares are: 1 mm × 1 mm in sample (a), and 2 × 2 mm in sample (b)..... 88
- Figure 5.13: Image of the white reference used for the specular reflection measurements. The printed markings (from previous unrelated experiments due to unavailability of a new white reference with similar reflective properties) can influence some images obtained with the system, but their effect is excluded for spectral measurements. 89
- Figure 5.14: Areas enumerated prior to the spectral information extraction. 89
- Figure 5.15: Defects present in areas of the printed samples (a, b, c) or in the same areas of the white reference used (d, e)..... 90
- Figure 5.16: (Left) Selected image area with defects detected by our method. (Right) Histogram of the image analyzed with the following highlighted values: (yellow) median, (blue) maximum frequency histogram bin, (red) mean, and (green) limits of the acceptance range A 90
- Figure 5.17: Rejection of background pixels by the defect removal algorithm due to their difference 91

Figure 6.1: Microscope image of one of the large patches made by printing numerous consecutive lines.	94
Figure 6.2: Image in off-specular reflection of areas printed with a laser wavelength of 488 nm, and laser powers of 300 mW (left group) and 400 mW (right group).....	95
Figure 6.3: Colors obtained in transmission mode of the front side of the samples	95
Figure 6.4: Colors obtained in transmission mode of the back side of the samples	95
Figure 6.5: Colors obtained in the 15°:15° specular reflection mode of the front side of the samples	96
Figure 6.6: Colors obtained in the 15°:15° specular reflection mode of the back side of the samples	96
Figure 6.7: Colors obtained in the 45°:0° off-specular reflection mode of the front side of the samples	96
Figure 6.8: Colors obtained in the 45°:0° off-specular reflection mode of the back side of the samples	97
Figure 6.9: Colors displayed by six different printed patches in all the geometrical configurations tested. The colors were obtained from hyperspectral measurements assuming a D65 illuminant.	98
Figure 6.10: Measured spectral reflectance factor (specular and off-specular modes) and transmittance factor of fulltone primaries printed with PICS LUP and a halftone made with these primaries, and spectrum of the halftone patch predicted with the Yule-Nielsen modified Spectral Neugebauer model with the fitted parameters a and n values indicated above the plots.....	101
Figure 6.11: 2D and 3D representations of the measured colors in the specular and off-specular reflectance modes and the transmittance mode of fulltone primaries printed with PICS LUP and a halftone made with these primaries. The reference colors in the background of the 2D view were calculated by fixing a lightness value L^* of 50 units.....	102
Figure 6.12: Microscopic images of areas printed using the parameters selected for the halftoning primaries. The primaries are presented in the same order as in Table 7.....	103
Figure 6.13: Image of the squares printed for halftoning prediction testing, captured with the hyperspectral imaging system described in Chapter 5.	104
Figure 6.14: Specification of squares printed for halftoning evaluation. The squares on the leftmost column were printed by using only one primary, while the other 25 were printed by combining the primaries in the parenthesis in the proportions shown.	104
Figure 6.15: Microscopic image of a two-color halftone with a coverage of 2 lines of Primary 1 (blue) for each line of Primary 5 (yellow).	105
Figure 6.16: Measured and predicted spectra of the first halftoning square, located in the first row and second column of the sample, for the following configurations: (top	

row) transmission, (middle row) specular reflection, (bottom row) off-specular reflection. The left plots correspond to front side, while the right plots correspond to back side of the sample. The color differences between the measured and the predicted spectra, assuming a D65 illuminant, are displayed in the top-left corner of each plot. 106

Figure 6.17: Histograms of the CIE94 color differences obtained between measured and predicted spectra using the Neugebauer model for the 25 primary combinations studied. A global average of 2.04 CIE94 units was obtained. 107

Figure 6.18: Histograms of the CIE94 color differences obtained between measured and predicted spectra for the 25 primary combinations studied, using the Yule-Nielsen modified Spectral Neugebauer model with optimized n parameter. A global average of 1.95 CIE94 units was obtained. 108

Figure 6.19: Colors obtained in specular reflection mode using the optimized YNSN model for the exhaustive halftoning mixture of primaries described above. 109

Figure 6.20: Estimated color gamut volume for the front side of PICSLUP samples in the $15^\circ:15^\circ$ specular reflection geometry. 109

Figure 6.21: Estimated color gamut volume for the back side of PICSLUP samples in the $15^\circ:15^\circ$ specular reflection geometry. 109

Figure 6.22: Estimated color gamut volume for the front side of PICSLUP samples in the $0^\circ:0^\circ$ transmission geometry. 110

Figure 6.23: Estimated color gamut volume for the back side of PICSLUP samples in the $0^\circ:0^\circ$ transmission geometry. 110

Figure 6.24: Estimated color gamut volume for the front side of PICSLUP samples in the $45^\circ:0^\circ$ off-specular reflection geometry. 110

Figure 6.25: Estimated color gamut volume for the back side of PICSLUP samples in the $45^\circ:0^\circ$ off-specular reflection geometry. 111

Figure 7.1: Image printed by the PICSLUP system captured in different geometrical configurations: (left) $0^\circ:0^\circ$ transmission, (center) $15^\circ:15^\circ$ specular reflection, and (right) $45^\circ:0^\circ$ off-specular reflection. The area of the image is 1×1 cm. 114

Figure 7.2: Hidden pattern designed with colors measured from two squares from the ones printed in Section 6.1, displayed in the $0^\circ:0^\circ$ transmission recto (left) and $15^\circ:15^\circ$ specular reflection recto (right) configurations. 115

Figure 7.3: Diagram of printed areas with four sets of hypothetical parameters selected in order to produce two vertical rectangles on Configuration 1 and two horizontal rectangles in Configuration 2. 115

Figure 7.4: Colors produced by the four parameter sets selected in the $45^\circ:0^\circ$ off-specular reflection recto (left) and $0^\circ:0^\circ$ transmission recto (right) configurations. 116

Figure 7.5: Spatial arrangement designed with the four parameter sets selected to produce our 2-geometry pattern. 116

-
- Figure 7.6: Resulting colors displayed by the 2-geometry pattern designed in the $45^\circ:0^\circ$ off-specular reflection recto (left) and $0^\circ:0^\circ$ transmission recto (right) configurations. 117
- Figure 7.7: Same sample displayed in Figure 5.12 Sample (b), observed with small angles with respect to the surface plane in the following configurations: Off-specular reflection verso with the approximately the same position for illumination and observation (left), and transmission recto with diffuse illumination from behind (right). 119
- Figure 7.8: Microscope images of printed of samples printed on paper substrates (A): observed in off-specular reflection ((a) and (b)) and in specular reflection ((c) and (d)); and printed on plastic PET substrates (B): observed in regular transmission ((a) and (b)) and in specular reflection ((c) and (d)). 119

LIST OF TABLES

Table 1: Some of the geometries recommended by the CIE for reflectance measurements.	34
Table 2: Chromaticity coordinates of the RGB primaries and white reference for the sRGB color space.....	46
Table 3: Dimensions of matrix M and vector A, and elements of vector A depending on the polynomial order. Note that A has only one row of elements.	64
Table 4: Overview of the four calibration methods used in this study.	68
Table 5: Average CIE94 results obtained with each of the four methods by assuming an A illuminant (i.e. a black body illuminant of 2856 K temperature).....	69
Table 6: Average CIE94 results obtained with each of the four methods by assuming a black body illuminant of 1800 K temperature.	71
Table 7: Printing parameters and CIELAB coordinates of the printing primaries used for the extended evaluation of halftoning predictions. The CIELAB values were measured with the hyperspectral imaging system in the specular reflection mode.....	103

RÉSUMÉ DES CHAPITRES

Ce mémoire est structuré de la manière suivante. Le premier chapitre introduit les principes sur lesquels repose la technologie d'impression étudiée, appelée PICSLUP (acronyme anglais de "Photo-Induced Colored Silver Luster Printing System"), ainsi que notre motivation à caractériser les couleurs que ce procédé peut générer.

Le chapitre 2 rappelle les notions fondamentales en sciences de couleurs et en photométrie, notamment celles relatives à l'interaction entre la lumière et les matériaux. Nous abordons la manière dont le système visuel perçoit les couleurs et introduisons les lois de base de la colorimétrie, les principaux espaces colorimétriques, et passons brièvement en revue les limites de la colorimétrie pour décrire parfaitement la perception des couleurs.

Le chapitre 3 expose les défis photométriques et techniques que nous avons dû relever pour caractériser les couleurs de surfaces colorées par le procédé PISCLUP. Nous présentons des moyens de mesure conventionnels et d'autres plus élaborés qui sont décrit plus en détail dans les chapitres suivants.

Dans le chapitre 4, nous exposons une première méthode de caractérisation des couleurs de ces échantillons basée sur de l'imagerie par microscope, permettant une caractérisation, dans une géométrie de réflexion spéculaire selon la normale des surfaces (géométrie $0^\circ:0^\circ$), de milliers d'échantillons micrométriques produits avec différents paramètres de commande du procédé. Une méthode de calibrage colorimétrique de la caméra a été spécialement développée pour s'accorder avec le caractère très spéculaire des échantillons étudiés. Les mesures effectuées selon cette méthode ont permis d'estimer la gamme de couleurs reproductibles par le procédé en réflexion normale spéculaire et d'analyser l'influence de plusieurs paramètres d'impression, notamment la polarisation de la lumière, sur les couleurs obtenues.

Dans le chapitre 5, nous exposons une autre approche basée un banc d'imagerie hyperspectrale que nous avons assemblé, et qui nous a permis d'obtenir les facteurs de réflexion et de transmission d'échantillons selon des angles d'éclairage et d'observation variables. Les données spectrales collectées ont ensuite permis de reconstruire les images en couleur de ces échantillons sous un illuminant choisi et d'analyser plus avant la gamme de couleurs reproductibles par le procédé dans d'autres configurations angulaires que celle permise par le microscope.

Dans le Chapitre 6, nous explorons la possibilité d'élargir les gammes de reproduction des couleurs dans chacune de ces configurations angulaires par l'utilisation de demi-tons. Avec le banc d'imagerie hyperspectrale, nous avons mesuré les facteurs spectraux de réflexion et de transmission d'échantillons imprimés en demi-tons, et nous

avons cherché à les prédire à partir de celles des couleurs primaires incorporées dans les couleurs en demi-tons, grâce à des modèles tels que les modèles de Neugebauer et de Yule-Nielsen.

Enfin, le chapitre 7 conclut le mémoire avec une discussion sur les potentielles applications du procédé PICSLUP et les sujets d'investigation qui mériteraient d'être poursuivis à l'issue de ce travail doctoral.

1

INTRODUCTION

In ancient history, glassworkers were already capable of producing colored glasses with dramatic color changes depending on the position of the light source with respect to the observer. It is the case, for example, of the Lycurgus cup (Figure 1.1) exhibited at the British Museum of London, which looks green by reflection of light and red by transmission of light.¹ It was discovered that this color change is due to the presence of gold and silver nanoparticles within the glass substrate,² which cause a wavelength dependent light absorption by a physical phenomenon called surface plasmon resonance.³ Metal nanoparticles are also responsible for the colored gloss effects displayed by lusterwares,^{4,5} ceramics coated by a metallic glaze, characteristic of the ancient Islamic art and of the Art Nouveau.



Figure 1.1: Lycurgus cup by reflection (left) and transmission (right) of light.

The progresses in photonics, and more recently in nanotechnologies, did not only permit to discover the reason of these surprising color effects, but also to reproduce them with modern technologies, especially lasers.

The work of this thesis is mainly focused on the color characterization and color management of a new printing technique that we call PICSLUP, which is based on these physical principles. While pursuing these goals, several interesting challenges were

encountered which resulted in contributions to unexplored areas in color characterization and innovations in color imaging technologies.

1.1 PICSLUP technology

The PICSLUP technology (Photo-Induced Colored Silver Luster Printing system) developed within the PHOTOFLEX project in the Laboratory Hubert Curien, Saint-Etienne, France, enables the production of gonioapparent color images on clear supports also prepared in the laboratory (TiO_2 coated glass plates⁸). The PHOTOFLEX project (ANR-12-NANO-0006) aims at extending the printing technology to flexible supports such as plastic⁶ and paper⁷ substrates. This PhD work and the PHOTOFLEX project are funded by the French National Research Agency within the program “Investissements d’Avenir” (ANR-11-IDEX-0007) and the LABEX MANUTECH-SISE (ANR-10-LABX-0075) grant of Université de Lyon,

Before printing, the supports are coated with a mesoporous film of amorphous titania, elaborated by a sol-gel process, and loaded with silver salt. This film is transparent and colorless, but it contains many small silver nanoparticles of about 1–3 nm in diameter.⁸ A diagram of the printing system can be seen in Figure 1.2, where an Ar-Kr continuous-wave laser is used at different wavelengths in the visible range: 488 nm, 514 nm, 530 nm and 647 nm.

Before printing, the supports are coated with a mesoporous film of amorphous titania, elaborated by a sol-gel process, and loaded with silver salt. This film is transparent and colorless, but it contains many small silver nanoparticles of about 1–3 nm in diameter.⁸ The printing equipment is installed on a microscope which also allows the observation of the printed areas thanks to a digital camera and adapted optics. A diagram of the printing system can be seen in Figure 1.2, where an Ar-Kr continuous-wave laser is used at different wavelengths in the visible range: 488 nm, 514 nm, 530 nm and 647 nm.

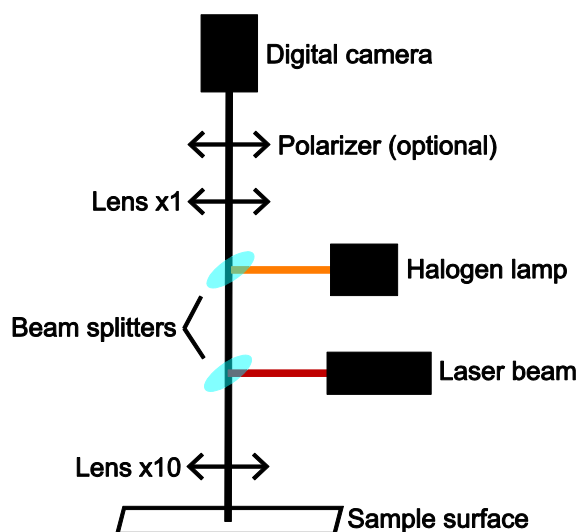


Figure 1.2 Optical scheme of the PICSLUP system used for microscopic laser inscription and imaging.

Due to the localized surface plasmon resonance of these nanoparticles, the film slightly absorbs light. When the film is irradiated by a laser beam with enough power, the small absorbance of the film is sufficient to induce a high increase of temperature, which favors the nanoparticle growth. An interesting interference effect, which sets up within the film itself between the incident field and guided modes excited by scattering on the growing nanoparticles,⁹ then occurs and promotes the organized growth of nanoparticles along lines periodically spaced parallel to the incident laser polarization. This anisotropy at the nanometer scale, shown in Figure 1.3, gives the sample a dichroic spectral behavior, i.e. polarization sensitive colors.^{10,11} The nanoparticles are located at the interface between the TiO₂ film and the glass support, which then creates interferences when illuminated by white light, between this particle plane and the air-coating interface. Diffraction by the aligned nanoparticles also creates particular colors at grazing angle in certain samples. Thus, the multiple colors displayed by one sample in different illumination and viewing conditions come from a combination of absorption by plasmon resonance, interferences, and diffraction.

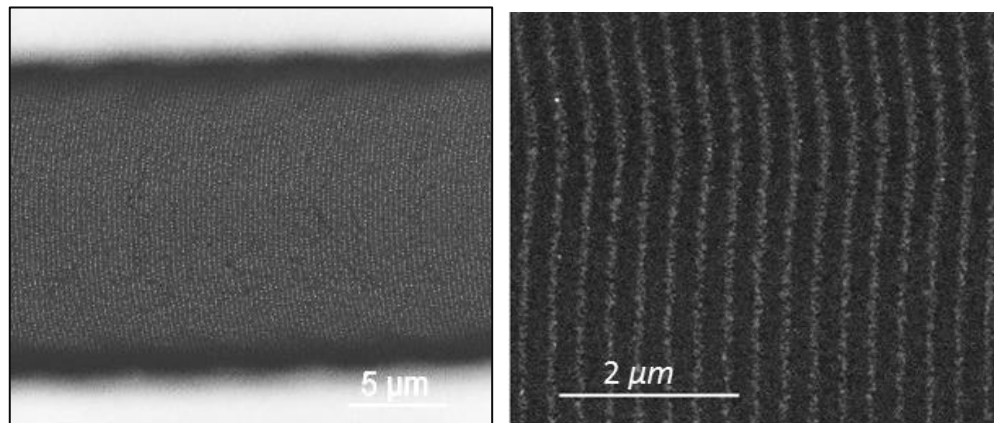


Figure 1.3: Image of the same area from a printed sample at different scales made by scanning electron microscopy where the nanoparticles are well aligned.

The final colors of a printed area are determined by several physical parameters: the nanoparticle shape, size and spatial organization, as well as the film thickness and refractive index that evolve during the laser treatment. All these final physical parameters depend on the exposure conditions, i.e. the laser power, focusing and wavelength, and the scanning speed of the laser on the sample. By varying these experimental parameters, several colors can be created in each point of the surface as in continuous-tone photographic printing. Figure 1.4 shows microscopic images of a printed surface captured by a calibrated RGB camera.

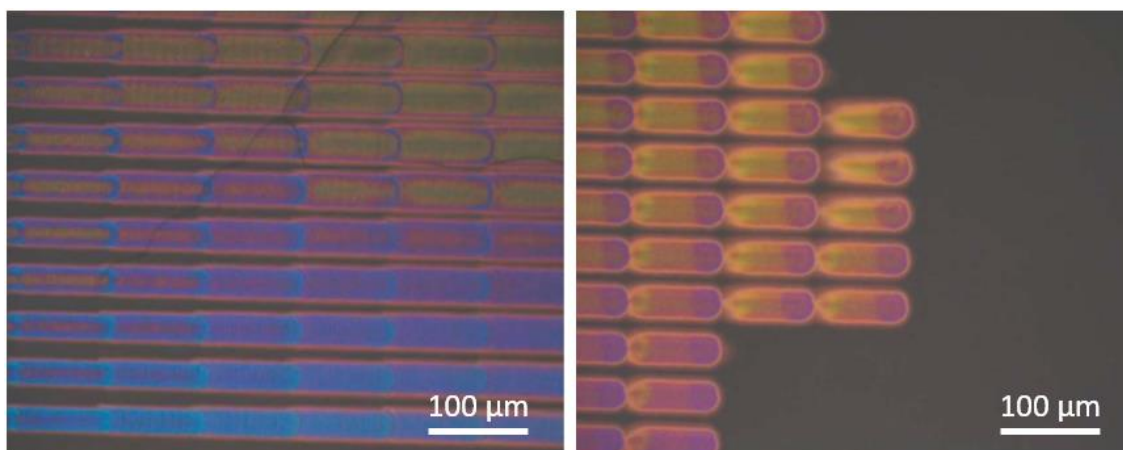


Figure 1.4: Microscope images of areas printed with varying laser focuses on the horizontal direction (100 μm period), and varying translation speeds on the vertical direction (50 μm period).

The colored areas combine the gonioapparent properties of both lusterware and stained glass: the colors perceived by reflection or transmission of light, in or out of the specular direction, are completely different. An example of these effects can be seen in Figure 1.5, where the same sample under the same illumination is seen from a different position, resulting in a dramatic change in the colors of the printed areas. Also, due to the self-alignment of nanoparticles, both reflected and transmitted colors may vary with the polarization of light.

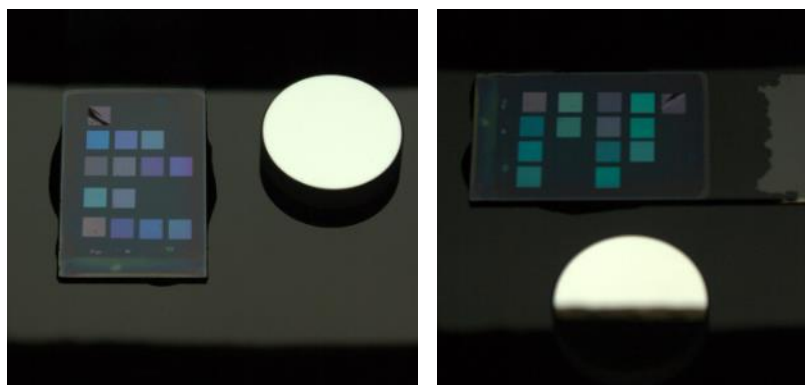


Figure 1.5: Sample printed with the PICSLUP system, observed from two different directions under the same illumination conditions. The colors of the squared areas (printed with different laser settings) change dramatically depending on the illumination/observation geometries or whether a polarizer is used.

1.2 Outline

The dissertation is outlined as follows. Chapter 2 introduces the fundamentals of color science and the interactions between light and materials with some general notions of radiometry and photometry. It then proceeds to describe how we perceive color thanks to our human visual system, and gives an introduction to colorimetry, popular color spaces and a brief review of the limitations colorimetry has to fully explain the colors we perceive.

In Chapter 3, we give an overview of the main photometric and technical challenges we faced when characterizing the color of the samples produced by the PICSLUP technology, and we present some conventional measurement strategies as well as introducing some more elaborated methodologies that are explained in detail in the subsequent chapters.

In Chapter 4, we present our first characterization approach based on microscope imaging for an exhaustive color characterization of the technology in the $0^\circ:0^\circ$ specular reflection geometry. In order to do this, we produced thousands of micrometric lines by varying the printing parameters of the system and developed a color calibration method for the microscope camera adapted to the specular properties of the samples. The measurements done with this strategy allowed us to estimate the range of colors that can be produced by the system in specular reflection, and to study the change of the colors displayed in this geometry due to the use of polarization and certain variations of the printing parameters.

In Chapter 5, we present a different approach based on a hyperspectral imaging system we assembled, which allowed us to obtain the spectral reflectance/transmittance factors of PICSLUP samples in adjustable angles of observation and incidence of light. From the spectral information we could reconstruct full color images of the samples with desired illuminants, and further analyze the range of colors produced by the printed samples in several measurement geometries considered.

In Chapter 6, we explore the use of halftoning techniques in order to produce new colors from the ones measured by the hyperspectral imaging system. Additionally, we evaluated the prediction of the colors obtained from selected primaries by using the Yule-Nielsen modified Spectral Neugebauer model, which allows us to predict the colors that can be produced by the technology with the combination of measured primaries before these combinations have been printed.

Finally, in Chapter 7 we present the conclusions of the dissertation, with a discussion of potential applications of the PICSLUP technology and proposals for future work based on the results presented in this report.

1.3 Publications

The following research papers were accepted by international peer-reviewed journals and conferences during the doctoral program:

- I. Daouda Keïta Diop, Lionel Simonot, Juan Martínez-García, Mathieu Hébert, Yaya Lefkir, Grégory Abadias, Philippe Guérin, David Babonneau and Nathalie Destouches. **“Spectral and color changes of Ag/TiO₂ photochromic films deposited on diffusing paper and transparent flexible plastic substrates,”** Applied Spectroscopy, (accepted) 2016. (Impact factor: 2.01).
- II. Juan Martínez-García, Mathieu Hébert, Alain Trémeau, Nicolas Crespo-Monteiro, and Nathalie Destouches. **“Multi-color Properties of Silver Glaze Images Photo-engraved on Glass Plates,”** 23rd Color and Imaging Conference (CIC23), Society for Image Science and Technology (IS&T), 2015.¹²

- III. Juan Martínez-García, Mathieu Hébert, and Alain Trémeau. **“Color calibration of an RGB digital camera for the microscopic observation of highly specular materials,”** Electronic Imaging Conference, International Society for Photonics and Optics (SPIE), **2015**.¹³
- IV. Nathalie Destouches, Juan Martínez-García, Mathieu Hébert, Nicolas Crespo-Monteiro, Guy Vitrant, Zeming Liu, Alain Trémeau, Francis Vocanson, Florent Pigeon, Stéphanie Reynaud, and Yaya Lefkir. **"Dichroic colored luster of laser-induced silver nanoparticle gratings buried in dense inorganic films,"** Journal of the Optical Society of America B 31, C1-C7, **2014**. (Impact factor: 1.98).¹¹
- V. Manuel Melgosa, Juan Martínez-García, Luis Gómez-Robledo, Esther Perales, Francisco M. Martínez-Verdú, and Thomas Dauser. **"Measuring color differences in automotive samples with lightness flop: A test of the AUDI2000 color-difference formula,"** Optics Express 22, 3458-3467, **2014**. (Impact factor: 3.48).¹⁴

N.B. Paper V was not related to the PhD. Thesis but was published during the PhD. appointment period (from sept. 2013 to sept. 2016).

2

COLOR SCIENCE FUNDAMENTALS

2.1 What is color?

The nature of *color* seems to be deceptively obvious for anyone with a normally functioning visual system, but, just like other perception related qualities, it is very difficult to define without referencing itself indirectly by using terms like “blue” and “green”, which would not be very useful for someone that has not experienced a color sensation.

Some definitions of color describe it as a subjective sensation, relying on the interpretation of stimuli by our visual system; while other definitions rely on the physical interactions between light and materials, which describe color as an intrinsic property of objects. The following is a simple definition given by the Oxford Dictionary¹⁵:

“The property possessed by an object of producing different sensations on the eye as a result of the way it reflects or emits light.”

One commonly accepted technical definition was given by the Committee on Colorimetry of the Optical Society of America in 1940, as cited by Hardeberg¹⁶:

“Color consists of the characteristics of light other than spatial and temporal inhomogeneities; light being that aspect of radiant energy of which a human observer is aware through the visual sensations which arise from the stimulation of the retina of the eye.”

This definition highlights the importance of the physical and the psychological aspects of color perception, which will be described in more detail throughout the rest of this chapter.

2.2 Light

Light is the type of radiation in the form of electromagnetic waves that can be perceived by the human eye. Electromagnetic radiation can be described as a wave and classified according to its wavelength, i.e. the distance between the wave's peaks (see Figure 2.1). The visible portion of the electromagnetic spectrum in vacuum corresponds approximately to the wavelengths in the range from 360 nm to 830 nm, between the ultraviolet and infrared radiations.

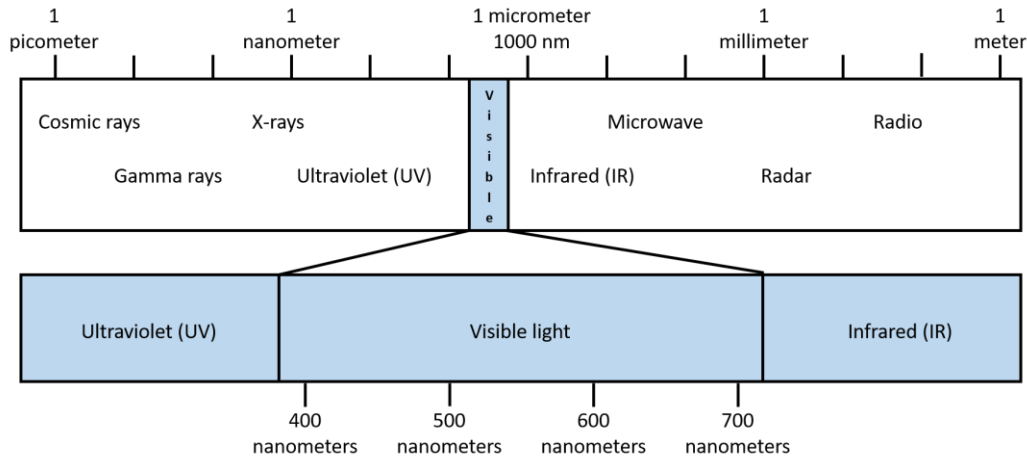


Figure 2.1: The electromagnetic spectrum.

Isaac Newton showed in 1671 that white light, such as sunlight, is composed of a collection of colored lights, which he called the spectrum.¹⁸ His experiment consisted in inserting sunlight into a prism resulting in its separation in roughly seven color components: violet, indigo, blue, green, yellow, orange and red. He further proved that these components could be reunited back into white light. Further advances in the field demonstrated that light is actually composed of an infinite range of wavelength-dependent components, and that light can be described in terms of the relative power emitted at each of its wavelengths, which is commonly referred to as the spectral power distribution (SPD). Figure 2.2 shows the relative spectral power distribution of typical daylight. By convention, the magnitudes are normalized by scaling the values such that the power at 560 nm is defined as a unit.¹⁹

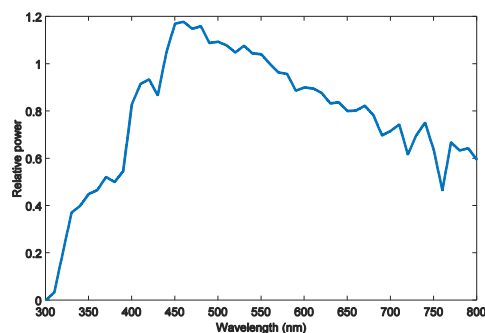


Figure 2.2: Relative spectral power distribution of typical daylight given by the standard illuminant D65.

2.3 Interaction between light and surfaces

Light can be altered when it strikes the surface of objects and propagates within the materials. This transformation depends on the particular structure of the material illuminated and the changes occur in a wavelength-dependent manner. Some of the phenomena that take place during these interactions are the following:

- **Surface reflection:** When light strikes a surface, more precisely, the interface between air and the material, it is partly reflected, while the rest of the light is refracted into the material. If the air-material interface is flat, the reflection and refraction directions of light are given according to the direction of the incident light, by Snell's law²¹; the proportions of the reflected and refracted fluxes are given by Fresnel formulas,²² according to the orientation and the polarization of the incident light. When the interface is rough the incident light is scattered in various directions.
- **Absorption:** While propagating within a material, light can be partially or totally absorbed by it, which results in a reduction of visible light. Absorption can vary throughout different wavelengths in the visible spectrum, resulting in perceptible color changes of the light. For purely absorbing materials, light rays propagate along straight lines and are exponentially attenuated according to Beer's law²³ as a function of the distance travelled. Metallic nanoparticles may also absorb light selectively according to the wavelength because of an electronic phenomenon at their surface called plasmon resonance.³
- **Scattering:** In turbid media, the propagation of light is not along straight lines but is scattered in many directions, making the material translucent or opaque.
- **Wave optics phenomena:** Some materials with nearly regular structure can have a color appearance, even though the material components are clear or achromatic, because of wave effects when the light propagates in them.²⁴ These colors, sometimes called "structural colors" in opposition with colors due to absorption within the matter,²⁵ include interferences and diffraction. Interferences denote wave effects occurring within thin layers of material, such as mother of pearl, soap bubble, oil on water, human hair, and PICSLUP prints. The waves reflected by the front and back interfaces of the layer add each other and form a new wave whose amplitude is magnified or decreased according to the wavelength and the layer's thickness. In PICSLUP prints, interference occurs between the air-TiO₂ interface and TiO₂-glass interface where the silver nanoparticles are mainly located. Diffraction denotes wave effects produced by materials with periodical structure, such as thin engraved lines in CDs and gratings, thin cones in butterfly wings, and lines of nanoparticles in PICSLUP prints. Each component of the grating transforms a planar wave into spherical ones whose amplitude add, and make waves with magnified amplitude in some directions and reduced amplitude in other directions, these directions depending on the wavelength.

The physical stimuli perceived by our eyes when we observe objects in a scene (also called *color stimuli*) are the result of light interacting with their surfaces and being successively altered by these optical phenomena.

2.4 Photometry of surfaces

The result of the optical phenomena previously mentioned is that part of light illuminating the object returns to the same side as the light source, i.e., it is reflected. The fraction of reflected light is characterized by various photometric concepts according to the application: (spectral, angular, or polarized) reflectance, reflectance factor, or BRDF.

- **Reflectance:** The term *reflectance* denotes any ratio of reflected flux to incident flux being relative to a same surface element. Reflectance is therefore a ratio of exitance to irradiance. It is a dimensionless quantity depending possibly on wavelength, direction, polarization and position on the surface. Reflectance also depends on the measuring geometry, i.e. the solid angles fulfilled by the incident flux (ω_i) and the captured part of reflected flux (ω_r). For example, the reflectance of a perfect mirror illuminated at 45° from its normal is non-zero only when the detector is located in the specular direction, and zero elsewhere. Geometry must therefore be specified for every reflectance. Judd²⁶ then Nicodemus²⁷ defined nine geometries where each of the incident and outgoing fluxes and fulfill a solid angle being either small (directional), large (conical) or equal to the whole hemisphere (hemispherical). A list of geometries recommended by the CIE for color characterization of rather diffusing surfaces, especially in the color reproduction domain, is listed in Table 1. The shortcut notation for a geometry is $\omega_i:\omega_r$, where directional light is specified by the incident angle, and hemispherical solid angle is specified by the letter *d*.

Table 1: Some of the geometries recommended by the CIE for reflectance measurements.

Appellation	Illumination	Capture
Diffuse / 8° geometry, specular component included (di: 8°)	Lambertian	Radiance (8°)
Diffuse / 8° geometry, specular component excluded (de: 8°)	Lambertian	Radiance (8°)
Diffuse / diffuse geometry (d:d)	Lambertian	Integrating sphere
Alternative diffuse geometry (d: 0°)	Lambertian	Radiance (0°)
45° annular / normal geometry (45° a: 0°)	Directional	Radiance (0°)
45° directional / normal geometry (45° x: 0°)	Directional	Radiance (0°)

- **Reflectance factor:** As most instruments contain one detector which is used to capture the reflected flux, the incident flux cannot be measured directly. It is measured indirectly by using a reference white reflector. The object to assess and the reference white reflector are illuminated and observed with the same

geometry. The ratio \hat{R} of the flux Φ measured from the object to the flux Φ_{ref} measured from the white diffuser is called *reflectance factor*²⁸:

$$\hat{R} = \frac{\Phi}{\Phi_{ref}} \quad (1)$$

Reflectance factor and reflectance coincide only in the case of very diffusing reflectors; reflectance factor thus provides a good approximation of reflectance (also called albedo) for matte papers and other nearly Lambertian reflectors. It is less relevant however for non-Lambertian reflectors such as glossy papers, mirrors or satin paintings. In some cases, the sample reflects more light towards the detector than the perfect diffuser and the reflectance factor overpasses one.²⁹ As for reflectance, the measurement geometry must be specified, and similar notations are used to denote geometries.

- **Bi-directional reflectance distribution function (BRDF):** This function has been introduced by Nicodemus²⁷ who considered that the reflection process of light by a surface is embodied in the fundamental equation relating the elemental irradiance dE_i coming from a direction (θ_i, φ_i) and the radiance $dL_r(\theta_r, \varphi_r)$ reflected into a direction (θ_r, φ_r) :

$$dL_r(\theta_r, \varphi_r) = f_R(\theta_i, \varphi_i; \theta_r, \varphi_r) dE_i(\theta_i, \varphi_i) \quad (2)$$

where function $f_R(\theta_i, \varphi_i; \theta_r, \varphi_r)$ depends upon the incidence and reflection angles. As reflectance and reflectance factor, it may also depend upon wavelength, polarization and position on the surface.

All these concepts have an equivalent in transmission: transmittance, transmittance factor, and Bi-directional transmittance distribution function (BRDF).

2.5 Human visual system

We are able to see the world around us thanks to our visual system. The lenses in our eyes focus the light reflected by the objects in our environment onto a layer in the back of our eyeballs called the retina, which contains photoreceptors of two kinds: rods and cones.³⁰ Rods are mainly responsible for vision in dark conditions (scotopic vision) while cones are additionally active in vision during bright conditions (photopic vision). Cones are mainly located in a very small area in the center of the retina called the fovea, whereas rods are distributed all around the retina.

An observer with normal vision has three types of cones: S, M and L, which have higher sensitivities in the short, medium and long wavelengths, respectively (see Figure 2.3). Unlike rods, that consist of only one type of pigment and only perceive different levels of intensity of light, cones are able to perceive finer variations in the spectral power distribution of the stimulus received. These signals integrated by the three types of sensors and subsequent cognitive processing result in our color sensations.

The human vision system is also capable of adjusting to a wide range of illuminance levels, being able to observe objects under very dim moonlight and under direct sunlight, which corresponds to a range from approximately 0.0003 lux to 100.000 lux. This adaptation is done partly by an adjustment of the size of the pupil and also by the dynamic adjustment of the response of the photoreceptors, which contribute to a very high dynamic range in comparison to electronic detectors.

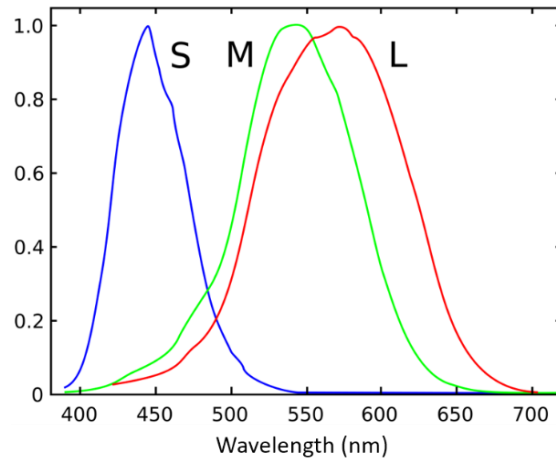


Figure 2.3: Relative spectral sensitivity of the S, M and L cones, according to Stockman et. al.³¹

2.6 Color attributes

According to the American Society for Testing and Materials (ASTM) and the International Commission on Illumination (CIE, for Commission Internationale de l'Éclairage), the colors of uniformly illuminated objects can be described by using the following three attributes (as quoted from the standards)¹⁹:

Hue: *Attribute of a visual perception according to which an area appears to be similar to one of the colors, red, yellow, green, and blue, or to a combination of adjacent pairs of these colors considered in a closed ring.*³²

Lightness: *Attribute by which a perceived color is judged to be equivalent to one of a series of grays ranging from black to white.*³³

Chroma: *Attribute of color used to indicate the degree of departure of the color from a gray of the same lightness.*³³

For example, a strawberry is of a red hue, with medium-low lightness and high chroma; and a lemon is of a yellow hue, with medium lightness and low chroma.

2.7 Colorimetry

Colorimetry is the part of color science related to the quantitative specification of the color of given physical stimulus with the following goals proposed by Wyszecki and Stiles³⁴:

1. *When viewed by an observer with normal color vision, under the same observing conditions, color stimuli with the same specification look alike,*
2. *Color stimuli that look alike have the same specification, and*
3. *The numbers comprising the specification are continuous functions of the physical parameters defining the spectral radiant power distribution of the stimulus.*

Several studies in the last centuries produced specifications fulfilling these rules by developing perceptual color matching experiments based on altering the ratio of the intensities of red, green and blue monochromatic lights superposed onto the same area in order to match the color of a separate target light.³⁵

The findings from these experiments were summarized by Hermann Grassmann in what are known as Grassmann's Laws¹⁶ in 1853:

1. *Three independent variables are necessary and sufficient to psychophysically characterize a color (called tristimulus values).*
2. *The result of an additive mixture of colored light depends only on the psychophysical characterization, and not on the spectral composition of the colors.*
3. *Linearity: If the components of a mixture of color stimuli are moderated with a given factor, the resulting psychophysical color is moderated with the same factor.*

The ratios obtained by these additive mixture experiments were enough to specify the physical stimulus perceived by the human visual system but these ratios were dependent on the particular light sources employed in the experiments. In order to make the communication of color values comparable between different experiments, the CIE proposed the 2° RGB color specification system,³⁶ described below, as a standard.

2.7.1 The 2° CIE RGB system

The CIE RGB system based on a field of view of 2°, consists in the following monochromatic lights as primaries: Red at 700 nm, Green at 546.1 nm and Blue at 435.8 nm, selected due to their excellent repeatability.¹⁹ When the ratio of these lights is modulated in order to match each wavelength of the visible spectrum, a direct relation is established between the amounts of each light used for the match (tristimulus values) and the respective responsivities of our photoreceptors to each wavelength. By using the results obtained in the color matching experiments of Wright³⁷ and Guild,³⁸ their average \bar{r} , \bar{g} , and \bar{b} curves were obtained (see Figure 2.4), called the RGB color matching functions for the 2° CIE Standard Observer.¹⁹ To illustrate the meaning of these curves, let's see the example of matching a monochromatic light at 600 nm. In this case the

average of observers produced this match with a combination of 0.1 of green primary and 0.3 of red primary.

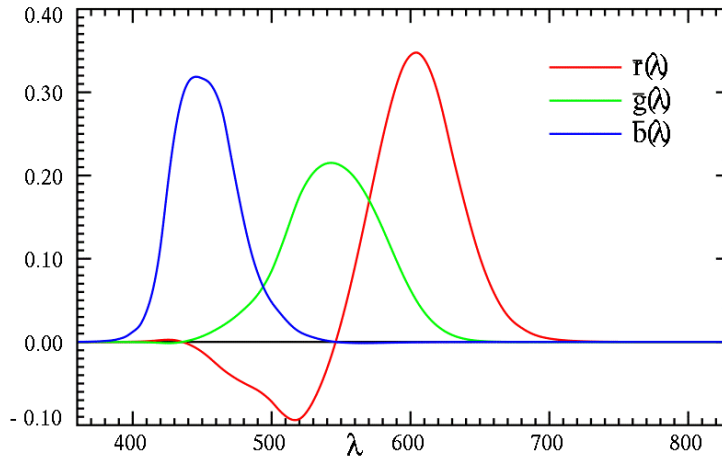


Figure 2.4: RGB color matching functions for the 2° CIE Standard Observer, obtained from the average of 17 observers matching each wavelength by modulating the three CIE RGB primaries assessed with a 2° field of view.³⁶

An interesting aspect to note about these curves is that each of them have a portion of negative values, which might seem illogical, since it would mean that a negative amount of energy from the given primary was used for the match. The reason for this to happen is that for each wavelength to be matched, the only way to obtain the same amount of saturation is to use a primary light made of precisely that wavelength. Thanks to the linearity expressed in Grassmann Law's,¹⁶ another way to obtain this match is to add some amount of light from one of the three RGB primaries to the monochromatic target and then match this new reference with a combination of the other two primaries. The tristimulus values for this match are expressed with a negative value for the primary added to the target, and the two positive values used from the other two primaries. For example, as can be seen in Figure 2.4, we need to have 0.06 of green and blue primaries in order to match a monochromatic light at 495 nm combined with 0.06 red primary.

The RGB color matching functions define a three-dimensional color space where any physical color stimulus can be precisely described by the amount of R, G and B primaries used, and allows us to have a visual representation of the distribution of colors.

In order to obtain such RGB values from the spectral radiant power distribution C_λ of a color stimulus, the following functions are used:

$$R = \int_{vis\ \lambda} C_\lambda \bar{r}_\lambda d\lambda \quad (3)$$

$$G = \int_{vis\ \lambda} C_\lambda \bar{g}_\lambda d\lambda \quad (4)$$

$$B = \int_{vis\ \lambda} C_\lambda \bar{b}_\lambda d\lambda \quad (5)$$

where \bar{r} , \bar{g} , and \bar{b} correspond to the curves shown in Figure 2.4, and the integration is performed in the visible range of the electromagnetic spectrum, i.e., from 360 nm to 830 nm.

2.7.2 The 2° CIE XYZ system

The fact that each of the \bar{r} , \bar{g} , and \bar{b} color matching functions contains negative values posed a costly constraint for spectrophotometer manufacturers that aimed to automate the color measurement process.¹⁹ This led to the development of a new system called the 2° CIE XYZ system, obtained from a mathematical linear transformation applied to the 2° CIE RGB tristimulus values³⁹. The calculation of the transformation matrix depends on the illuminant used and is explained in detail in Appendix 2. The following matrix corresponds to the one used by the CIE according to the equi-energy illuminant E, which has a constant relative power of 1 throughout the whole visible spectrum:

$$\begin{pmatrix} X \\ Y \\ Z \end{pmatrix} = \begin{pmatrix} 2.7689 & 1.7517 & 1.1302 \\ 1.0000 & 4.5907 & 0.0601 \\ 0.0000 & 0.0565 & 5.5943 \end{pmatrix} \begin{pmatrix} R \\ G \\ B \end{pmatrix} \quad (6)$$

Conversely, the 2° CIE RGB tristimulus values can be obtained from 2° CIE XYZ values by using the inverse transformation. The matrix according to the E illuminant is as follows:

$$\begin{pmatrix} R \\ G \\ B \end{pmatrix} = \begin{pmatrix} 0.4185 & -0.1587 & -0.0828 \\ -0.0912 & 0.2524 & 0.0157 \\ 0.0009 & 0.0025 & 0.1786 \end{pmatrix} \begin{pmatrix} X \\ Y \\ Z \end{pmatrix} \quad (7)$$

This transformation, in addition to removing the negative values from the color matching functions, also has the property that the \bar{y} color matching function (see Figure 2.5) is almost identical to the $V(\lambda)$ photopic luminous efficacy function³⁰ which represents the perceived intensity according to radiance emitted in a given wavelength. A comparison of both of these curves is shown in Figure 2.6.

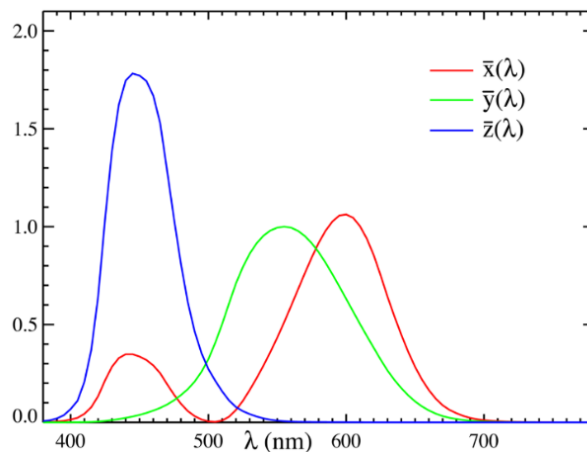


Figure 2.5: XYZ color matching functions for the 2° CIE Standard Observer, obtained from a mathematical linear transformation applied to the CIE RGB system.

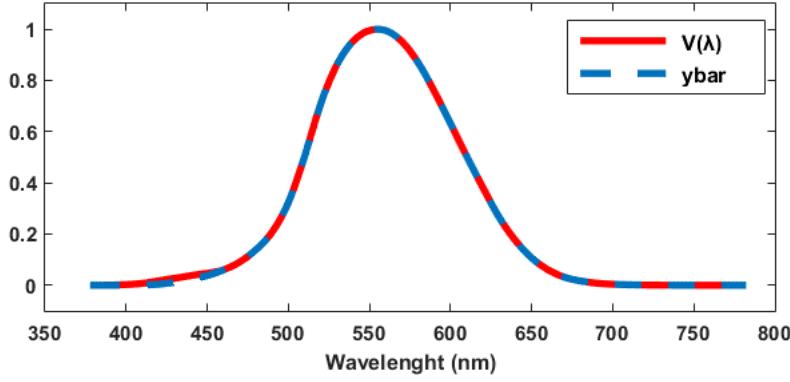


Figure 2.6: Comparison between the \bar{y} color matching function and the photopic luminous efficacy function $V(\lambda)$.³⁰

In order to calculate the XYZ tristimulus values directly from the spectral radiant power distribution C_λ of a color stimulus, a similar process to the calculation of the RGB values is used:

$$X = \int_{vis} C_\lambda \bar{x}_\lambda d\lambda \quad (8)$$

$$Y = \int_{vis} C_\lambda \bar{y}_\lambda d\lambda \quad (9)$$

$$Z = \int_{vis} C_\lambda \bar{z}_\lambda d\lambda \quad (10)$$

where \bar{x} , \bar{y} , and \bar{z} correspond to the curves shown in Figure 2.5, and the integration is performed in the visible range of the electromagnetic spectrum, i.e., from 360 nm to 830 nm.

2.7.3 XYZ tristimulus values of materials

As we saw earlier in this chapter, the color stimuli that are perceived by our visual system are the result of spectral interactions between light and materials. In practice, a continuous measurement of the color signal is not available, but rather a series of discrete measurements from the light source and the spectral properties of the materials. By using these measurements and the color matching functions as inputs, a good approximation of the XYZ values is calculated with the following summations¹⁹:

$$X = k \sum_\lambda S_\lambda R_\lambda \bar{x}_\lambda \Delta\lambda \quad (11)$$

$$Y = k \sum_\lambda S_\lambda R_\lambda \bar{y}_\lambda \Delta\lambda \quad (12)$$

$$Z = k \sum_\lambda S_\lambda R_\lambda \bar{z}_\lambda \Delta\lambda \quad (13)$$

$$k = \frac{100}{\sum_\lambda S_\lambda \bar{y}_\lambda \Delta\lambda} \quad (14)$$

The summations are performed in the visible range of the electromagnetic spectrum, i.e., between 360 nm and 830 nm, where S_λ is the Spectral Power Distribution of the light illuminating the material; R_λ is the spectral reflectance factor of the material,

or transmittance factor if the material is transparent and is illuminated in transmission; \bar{x}_λ , \bar{y}_λ and \bar{z}_λ are the color matching functions for the CIE Standard Observer; $\Delta\lambda$ is the wavelength interval in nanometers used for the measurements (normally below 10 nm to improve the accuracy of the values calculated); and k is a factor which normalizes the tristimulus values according to the lightness of the light source, setting its Y value to 100 and as a result, the Y values of the materials are in the range between 0 and 100 (except for some cases where fluorescence occurs).

2.7.4 Chromaticity diagram

One common representation for color values derived from the three-dimensional XYZ color space is its projection onto a two-dimensional space called chromaticity diagram obtained from the following equations³⁹:

$$x = X/(X + Y + Z) \quad (15)$$

$$y = Y/(X + Y + Z) \quad (16)$$

$$z = Z/(X + Y + Z) \quad (17)$$

The obtained values are called chromaticity coordinates. Although they are three, it can be noted that $x + y + z = 1$. Thus, only two of them are needed to describe a color. By convention the x and y coordinates are kept, maintaining roughly the hue and chroma of the colors, while losing most of the information related to their lightness. Because of the projection on the x - y plane, the magnitudes of the variables are lost and only their ratio is maintained. However, all the information can be preserved if one of the XYZ tristimulus values is kept. When this is needed, the value Y , which is associated with the luminance of a stimulus, is commonly conserved and the color is described in terms of xyY coordinates. The most common representation of the chromaticity diagram includes a curve called the spectrum locus (see Figure 2.7), formed by the coordinates of the colors produced by monochromatic stimuli throughout the visible spectrum. As the most saturated colors can be produced by monochromatic lights, the coordinates of most colors can be placed within the spectrum locus.

The chromaticity diagram is convenient for lighting systems, especially when light emitted by lamps with different SPDs are mixed. The chromaticity of the resulting light is given by a linear combination of the individual chromaticities of the lamps, weighted by their respective powers. In the diagram, the point of the resulting light is a barycenter of points representing the different lamps. For surfaces, the chromaticity concept is often used for communication, since it is convenient to display colors in a two-dimensional graph. However, chromaticity is not suitable for surfaces as lightness is often crucial for good representation of their color.

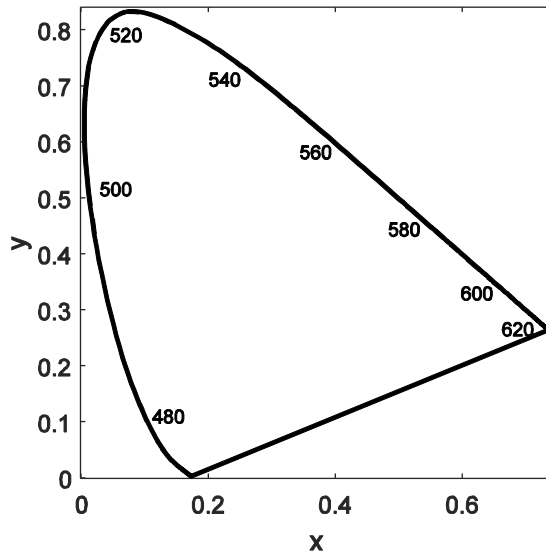


Figure 2.7: Chromaticity diagram of the CIE XYZ color specification system. The wavelengths of the monochromatic lights used to generate the spectrum locus are shown within the curve.

2.8 Uniform color spaces

The main disadvantage of the RGB or XYZ color spaces is that the distribution of colors in them is perceptually non-uniform, i.e. equal steps of separation between colors in different regions generally do not correspond to the same perceptual difference between the colors. The non-uniformity in the XYZ color space is evidenced by the experiments of David MacAdam,⁴⁰ in which observers were given two colors, one fixed and the other adjustable, and they were asked to change the adjustable color until the difference between both colors was not perceptible. This process was repeated for many fixed colors with several adjustable colors each. The results of these experiments are shown in Figure 2.8, where the elliptical patterns represent all the colors (with a fixed lightness) that are perceptibly similar to the fixed color centers.

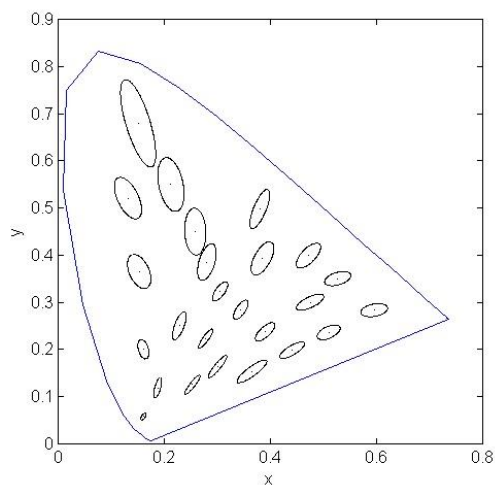


Figure 2.8: Ellipses representing the average just noticeable color differences (JND) obtained by David MacAdam⁴⁰ in 1942. For clarity, the ellipses are depicted at 10 times their size.

From this plot it can be noted that the threshold commonly called *just noticeable difference* (JND) varies widely throughout the whole x - y chromaticity diagram. This color-difference non-uniformity also appears with differences of lightness, especially due to the fact that our sensitivity to light is not linear. All these non-uniformities motivated the development of new chromaticity diagrams and ultimately of more uniformly distributed three-dimensional color spaces.

2.8.1 The CIE 1976 UCS chromaticity diagram

The CIE 1976 Uniform Chromaticity Scale (UCS) diagram³⁶ provides an improved uniformity in the u' - v' space with very simple transformations from the x - y chromaticity coordinates:

$$u' = \frac{4x}{-2x+12y+3} \quad (18)$$

$$v' = \frac{9y}{-2x+12y+3} \quad (19)$$

The u' - v' coordinates can also be obtained directly from the XYZ tristimulus values by using the following formulas:

$$u' = \frac{4X}{X+15Y+3Z} \quad (20)$$

$$v' = \frac{9Y}{X+15Y+3Z} \quad (21)$$

2.8.2 The CIELAB color space

In 1976, the CIE proposed the three-dimensional CIELAB color space³⁶ which to date still remains the most popular system for color specification. It consists of the axes L^* (a predictor of lightness); and, a^* and b^* , represents a chromatic plane corresponding to the opponent colors green-red and blue-yellow, respectively. One of the main advantages of the CIELAB system is the improved uniformity in the lightness axis accomplished by a non-linear compression that resembles our lightness perception.

The CIELAB coordinates can be obtained from XYZ tristimulus values:

$$L^* = 116 * f(Y/Y_n) - 16 \quad (22)$$

$$a^* = 500[f(X/X_n) - f(Y/Y_n)] \quad (23)$$

$$b^* = 200[f(Y/Y_n) - f(Z/Z_n)] \quad (24)$$

where

$$f(t) = \begin{cases} t^{1/3} & \text{if } t \geq 0.008856 \\ 7.787 t + \frac{16}{116} & \text{otherwise} \end{cases} \quad (25)$$

and the variables with n as subscript correspond to the tristimulus values of the reference white point.

Coordinates in the CIELAB space can be represented in a cylindrical manner in order to have a specification of the three color attributes: lightness, chroma and hue, where lightness is given by the L^* , chroma by C_{ab}^* , and hue by h_{ab} :

$$C_{ab}^* = \sqrt{a^{*2} + b^{*2}} \quad (26)$$

$$preH_{ab} = \begin{cases} \arctan(b^*/a^*) & \text{if } a^* > 0 \\ \arctan(b^*/a^*) + \pi & \text{if } a^* < 0 \text{ and } b^* \geq 0 \\ \arctan(b^*/a^*) - \pi & \text{if } a^* < 0 \text{ and } b^* < 0 \\ \pi/2 & \text{if } a^* = 0 \text{ and } b^* > 0 \\ -\pi/2 & \text{if } a^* = 0 \text{ and } b^* < 0 \\ \text{undefined} & \text{if } a^* = 0 \text{ and } b^* = 0 \end{cases} \quad (27)$$

$$h_{ab} = (2\pi + preH_{ab}) \bmod 2\pi \quad (28)$$

The detailed calculation of the h_{ab} allows to accurately obtain the quadrant and hue of the color. The same result can be obtained with the function *atan2*, included in many modern programming languages, with the parameters (b^* , a^*).

2.9 Color difference evaluation

Previously in this chapter, we have seen how colorimetry allows us to precisely measure two given homogeneous color stimuli and determine if they visually match under the same observation conditions.³⁰ After this problem was solved, another one naturally gained importance: if two color stimuli do not match, what is the magnitude of the perceived color difference between them? This is the main question that color-difference formulas try to answer, i.e., they try to estimate the magnitude of the visually perceived difference between two color samples from their objectively measured values.

Color-difference formulas are mathematical equations providing a value number ΔE from the tristimulus values of two color samples, taking also into account in some cases the specific illuminating and viewing conditions under which the two color samples are visually observed. The main goal of most color-difference formulas is that the quantity ΔE is in good agreement with the visually-perceived color differences ΔV obtained by a set of observers, considering pairs of color samples in any region of the color space observed under any viewing condition (e.g. different light sources, luminance levels, backgrounds, etc.). It can be noted that ΔV is the average subjective answer from human observers, related to the output of our human visual system, whereas ΔE is obtained by objective physical color measurements usually performed by instruments. Obtaining successful color-difference formulas is a challenging task because human visual color processing is not well known in many aspects.

An important aspect to take into account when developing and using color-difference formulas is the effect of the observation conditions or "parametric effects" which has been found to be very significant in previous studies.⁴² In order to obtain a more consistent set of experimental results from different sources that could be effectively used in conjunction and compared with each other, the CIE (Commission Internationale de L'Éclairage) proposed a number of reference conditions to be used,⁴³ which include:

spectral distribution of the light source, illuminance, color of the background, separation between the samples compared, photometric properties of samples used,¹⁴ among others.

The perceived visual difference (also called ΔV) is a subjective magnitude provided by an observer after assessing two color stimuli. The two most commonly used methods to obtain these perceived differences are called "anchor pair" and "grey scale". In the anchor pair method⁴⁴ the observer simply answers to the question of whether the color difference of the color pair that is being assessed is larger or smaller than the color difference of a reference (anchor) neutral color pair. On the other hand, the grey scale method⁴³ consists of having the observers evaluate the color difference of a color pair regarding a set of neutral color pairs with increasing color differences.

The visually perceived color difference can slightly vary between different observers,⁴⁵ therefore, it is important to have several normal vision observers in a psychophysical experiment for the purpose of adjusting, developing or evaluating color-difference formulas.

As it was previously mentioned, color-difference formulas receive as input the instrumentally measured tristimulus values of two homogeneous color samples and from them estimate the visually perceived color difference. Even though this objective has not been completely fulfilled yet, since it represents a very difficult task regarding the human vision and cognitive system whose processes are still being studied, significant advances have been made in this approximation in the last decades, making color-difference formulas a good tool in many applications, such as to estimate if two stimuli are perceptibly different or to estimate if such difference is acceptable for a given scenario.

Some color spaces have been designed³⁰ in order to transform the XYZ values to a more evenly uniform space regarding visual perception, among which the CIELAB³⁶ color spaces, described in the previous section, is recommended by the CIE.

The CIELAB color space has special importance since numerous commonly used color-difference formulas are based on it, i.e., they transform the tristimulus values to the $L^*a^*b^*$ space prior to making additional transformations and calculations to estimate the color difference between two color stimuli. Some of the most relevant color-difference formulas based on the CIELAB color space are:

- The CIELAB color-difference formula,³⁶ which is simply the Euclidean distance between the two colors in the CIELAB color space:

$$\Delta E = \sqrt{(\Delta L^*)^2 + (\Delta a^*)^2 + (\Delta b^*)^2} \quad (29)$$

- CIE94⁴⁶:

$$\Delta E_{94} = \sqrt{\left(\frac{\Delta L^*}{k_L}\right)^2 + \left(\frac{\Delta C_{ab}^*}{k_C(1+0.045\sqrt{C_{ab,1}^*C_{ab,2}^*})}\right)^2 + \left(\frac{\Delta H_{ab}^*}{k_H(1+0.015\sqrt{C_{ab,1}^*C_{ab,2}^*})}\right)^2} \quad (30)$$

where k_L , k_C , and k_H , are parametric factors conventionally set to 1;

- and more complex formulas such as CMC⁴⁷, and CIEDE2000⁴⁸.

Currently, CIEDE2000 is the standard color-difference formula recommended by the CIE and the International Organization for Standardization (ISO), however, this formula still presents several problems (such as low accuracy in the blue and very dark regions)⁵⁰⁻⁵¹ and there is still plenty of room for improvement in the development of color-difference formulas. Throughout this thesis, the CIE94 color-difference formula will be frequently used as it offers a better correlation to human perception than CIELAB, it is the most used formula for halftone color prediction studies, and has a low computational cost in optimization algorithms in comparison to CIEDE2000.

2.10 The sRGB color space

sRGB⁵² is one of the most popular color spaces for digital multimedia applications, such as monitors and printers, proposed jointly by Hewlett-Packard and Microsoft in 1996. The space is based on the D65 illuminant as a white reference and the following RGB primaries in the x-y chromaticity diagram:

Table 2: Chromaticity coordinates of the RGB primaries and white reference for the sRGB color space.

Chromaticity	Red	Green	Blue	White point (D65)
x	0.6400	0.3000	0.1500	0.3127
y	0.3300	0.6000	0.0600	0.3290
z	0.0300	0.1000	0.7900	0.3583

2.10.1 Transformation from XYZ to sRGB

Since the sRGB colors space is based on the D65 illuminant, the first step is to convert the XYZ tristimulus from their illuminant used into the D65 illuminant. This can be done with a *chromatic adaptation transform* (CAT), such as a Bradford transform.⁵³ Once the XYZ values have been adapted to D65, the following step is to apply a linear transformation to them by means of a matrix multiplication:

$$\begin{bmatrix} R_{linear} \\ G_{linear} \\ B_{linear} \end{bmatrix} = \begin{bmatrix} 3.2406 & -1.5372 & -0.4986 \\ -0.96889 & 1.8758 & 0.0415 \\ 0.0557 & -0.2040 & 1.0570 \end{bmatrix} \begin{bmatrix} X \\ Y \\ Z \end{bmatrix} \quad (31)$$

Afterwards, a non-linear operation (gamma curve) is applied to each of the RGB values obtained. In the following equation, C_{linear} represents R_{linear} , G_{linear} , or B_{linear} , and C_{srgb} represents R_{srgb} , G_{srgb} , or B_{srgb} , which are the final sRGB values:

$$C_{srgb} = \begin{cases} 12.92 C_{linear} & \text{if } C_{linear} \leq 0.0031308 \\ \left(1.055 C_{linear}^{\frac{1}{2.4}}\right) - 0.055 & \text{if } C_{linear} > 0.0031308 \end{cases} \quad (32)$$

2.11 Limitations of colorimetry

Even though colorimetry has made important advances during the last century, there are many color appearance phenomena that cannot be described by measured tristimulus values, especially when the colors assessed are not homogeneous patches and they are not observed in controlled viewing conditions. A common example of such phenomena is *simultaneous contrast*, identified by Chevreul in the mid-19th century,⁵⁴ which states that the color appearance of a given area is affected by the colors in its proximity. An example of this effect is shown in Figure 2.9, where the small squares in the centers were produced with the same color but the one on the left appears brighter than the one on the right.



Figure 2.9: Example of simultaneous contrast. The small squares in the centers have the same color but the one on the left appears to be brighter than the one on the right.

Initially, this effect was thought to be produced by a physiological response in our retina called *lateral inhibition* where the intensity of the signal received by some cells inhibits the response of other neighboring cells. However, another example presented by White,⁵⁵ shown in Figure 2.10, proved that this was not the only reason behind this effect, since according to it, the grey vertical rectangle on the right, which is adjacent to brighter areas, should be perceived as darker than the one on the left.

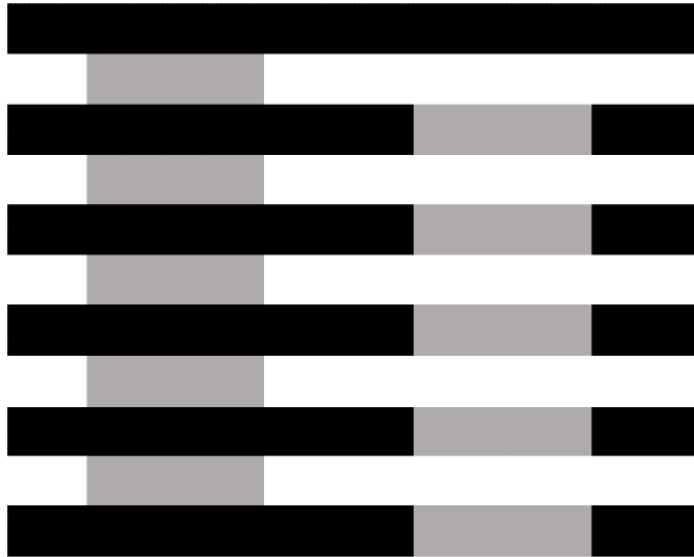


Figure 2.10: Example of simultaneous contrast. The perceived vertical rectangles were made using the same color, yet the one on the left appears to be brighter than the one on the right.

There are many other effects that influence the appearance of colors and are not considered by basic colorimetry, including:

- **Bezold effect**⁵⁶: Apparent color spread to neighboring areas;
- **Hunt effect**⁵⁷: Increase of colorfulness with luminance;
- **Stevens effect**⁵⁸: Contrast increases with luminance;
- **Bezold–Brücke hue shift**⁵⁹: Change of hue with luminance;
- **Abney effect**⁶⁰: Change of hue with the addition of white light;
- **Helmholtz–Kohlrausch effect**⁶¹: Brightness increases with saturation;
- among others.

In additions to these phenomena, adaptation and other vision mechanisms also come into play, and can dramatically influence the appearance of colors measured/observed if not taken into account:

- **Lightness adaptation**: Adaptation to changes in the intensity of light. Adaptation to low levels of lightness can take up to 30 minutes, while adaptation to bright levels takes approximately 5 minutes.
- **Chromatic adaptation**: The response curves of each of the cones types change in order to adapt to different chromaticities of illumination.
- **Color constancy**: Objects colors are perceived as unchanged even with different illuminations.
- **Memory colors**: The preexisting notion of the color of objects due to previous experience influences the colors we perceive.

The influence of many of these effects and mechanisms have been taken into account to some extent in recent color spaces and color-difference formulas. However, these models have been developed under very strict observation conditions, and require

the same level of rigorousness when they are used for their outcomes to be accurate. Some of these conditions considered are: spectral shape of illuminant, illuminance level, uniformity and color of background, uniformity of samples, texture of samples, field of view covered by the samples, separation between the samples (in the case of color-difference formulas), among others. The conditions required may not always be fulfilled depending of the type of samples used and observation geometries studied, which can have an influence in the accuracy of the different models.

The appearance of colors depends on many factors and the existing models are very useful to estimate the sensations they produce. However, there is plenty of room for improvement in terms of perfectly modelling the complexity of our human visual system.

2.12 Conclusion

Color perception is the result of a very complex process involving the interaction of light with different materials, the selective absorption of the modified light by the cells in our retina, and an intricate neural and cognitive process. The fundamentals of how this process is realized, as well as the different methods and systems that have been developed throughout the years in order to specify and measure color, have been illustrated in this chapter, giving us a good base upon which we can develop the ideas and methods presented in this thesis work.

3

PHOTOMETRIC CHARACTERIZATION OF THE PICSLUP TECHNOLOGY

The PICSLUP printing technology, presented in Chapter 1, is not yet in a manufacturing phase, but it is rather a prototype. The preparation of the printing support, the printing time, and many other aspects, are not optimized. The reproducibility of the colors, the printing resolution, and further problems such as printing under too high laser power, are still investigated. This makes some difficulties for exhaustive and precise characterization of the prints. However, the main characterization difficulties are introduced by the photometric properties of the prints themselves, due to their high specularity, high translucency and their goniochromaticity. Conventional instruments and tools for color reproduction could not be used, and other solutions had to be found instead, which constituted a significant part of the research effort reported here. In this chapter, we propose to review the main experimental issues related to the printing process itself, and optical characterization of the prints.

3.1 Sample production constraints

With a printing system such as PICSLUP whose optical phenomena underlying the color appearance are so different from conventional ink printing, the best method for an exhaustive characterization of the printing system would have been to print many color patches, one per set of command parameters of the printing system, i.e., by incrementing regularly each of the command parameters:

- exposure time (tuned by laser scanning speeds between 300 and 30000 $\mu\text{m/s}$),
- laser power, between 185 and 600 mW
- laser wavelength: 488, 514, 530, and 647 nm.
- laser focusing distance: between 0 and 4 mm from the focal plane

However, the PICSLUP printing process has not been optimized yet and the production of color charts is very time consuming. This led us to adopt selection strategies, or to reduce dramatically the size of the printed samples, with important consequences on the color characterization of the printing system.

The printable films consist of glass slides measuring 75 mm by 25 mm (see Figure 3.1), with a partial coating of TiO_2 which are made by a complex and costly sol-gel synthesis process (see Appendix 1) which also limits the availability of samples that can be produced for characterization. Moreover, uncertainty regarding the reproducibility of the sol-gel coating led to the preference of color charts printed on the same glass slide.



Figure 3.1: Glass support coated with the TiO_2 printable material, after been printed several times with different laser settings. Each of the squares in the grid have an area of $2 \text{ mm} \times 2 \text{ mm}$.

The PICSLUP technology prints micrometric lines with a width between 15 and 50 μm , depending on the focusing distance, and has constant printing speed which varies between 50 $\mu\text{m/s}$ and 30 mm/s, making the printing of a big areas a very long process. As an example, it takes approximately 8 hours to print an area of $1 \times 1 \text{ cm}$, with a speed of 1000 $\mu\text{m/s}$, with a line width of 20 μm , as the ones shown in Figure 3.2.

Due to these printing constraints, we decided to print a large number of patches of small size, and a reduced number of patches of medium/large size. The main color charts produced are:

- **Microscopic patches:** 10656 lines with a width lower than 50 μm and length of 100 μm , printed on 2 glass plates, with an exhaustive variation of all the printing parameters,
- **Middle-size patches:** 330 patches with an area of $1 \times 1 \text{ mm}$, printed on 3 glass plates, with a selected set of printing parameters.
- **Large patches:** 52 patches with an area of $6 \times 6 \text{ mm}$, printed on 10 glass plates, with varied command parameters.

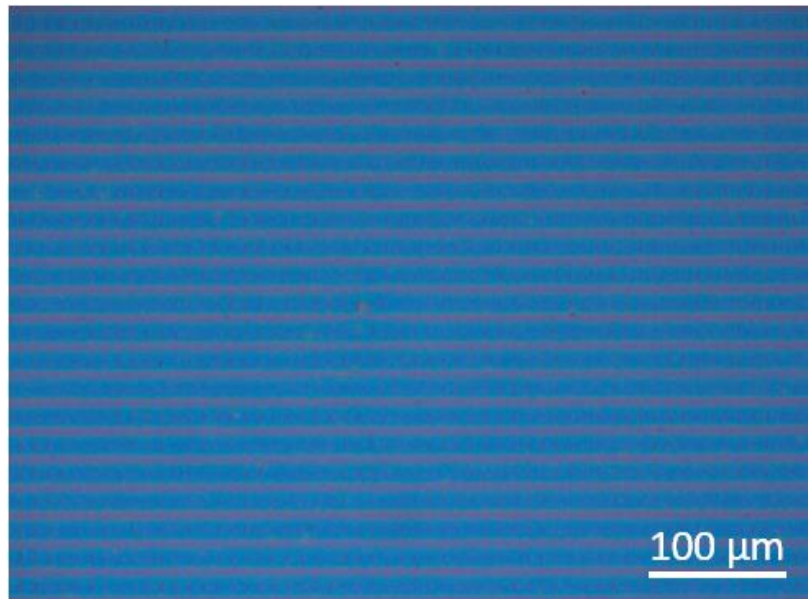


Figure 3.2: Microscopic image of a sample printed by the PICSLUP system.

3.2 Optical measurement constraints

The glass lusters printed with PICSLUP have a very different visual aspect from paper prints, especially due to their high specularity and their gonioappearance, which need high angular precision in the photometric measurements. For this reason, and also because of the small size of the color patches, the usual color characterization tools for color reproduction assessment are therefore not adapted.

3.2.1 High specularity

Objects can reflect light in different ways, depending on their particular properties and structure. In Figure 3.3 we can see how light is reflected from four different types of materials: perfectly diffusing material, perfectly specular material, roughened metal, and very glossy paper. The glass samples produced by the PICSLUP system are highly specular, having a strong specular component as in Figure 3.3 (b) and very small contribution in the rest of the hemisphere.

The specular properties of the samples make the measurements in the specular direction of light (opposite to the light incidence with respect to the normal of the sample) difficult, since the light intensity changes dramatically around the proximity of this direction, thus very precise optical alignments are necessary to obtain accurate results. Furthermore, the high specularity also makes measurement in off-specular configurations challenging, since the light intensity can be extremely low for certain geometries, requiring the use of very powerful light sources to reduce noise in the measurements.

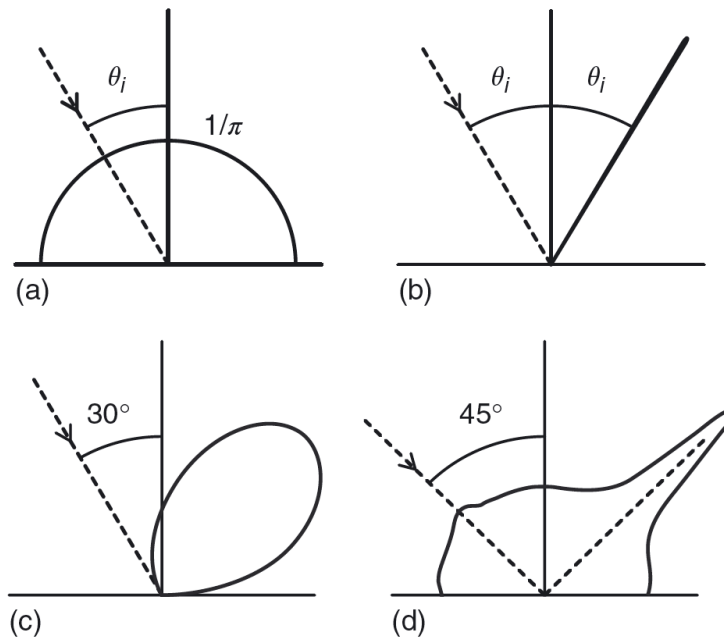


Figure 3.3: BRDF in the incidence plane of four different materials, where θ_i is the incident angle of light with respect to the normal of the surface. The curves represent the relative amount of light reflected in every direction in the incidence plane, the incident direction of light being shown by the dashed line. (a) Perfectly diffusing material, (b) Perfectly specular material, (c) Roughened metal, and (d) Very glossy paper. (Image used with permission of Mathieu Hébert).⁶²

3.2.2 Gonioappearance

As it was mentioned in Chapter 1, the images produced by the PICSLUP system are gonioapparent, i.e., their color changes with the variation of the angle of illumination or observation (see Figure 3.4). This is due to the interferential properties, and is especially noticeable in the surrounding of their specular direction of light, where, not only the intensity of light but also the color of the sample can change dramatically, making precise optical alignment very important.

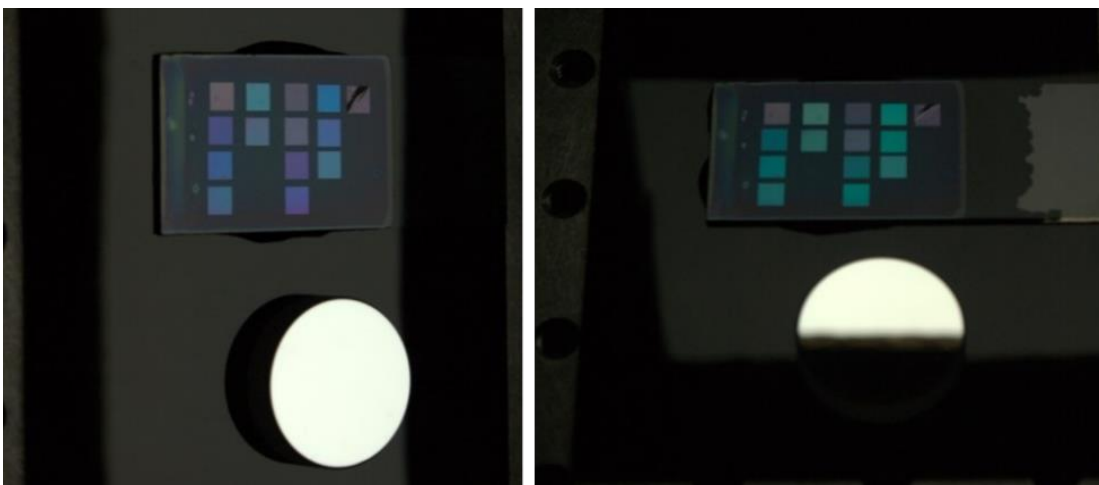


Figure 3.4: Sample printed with the PICSLUP system, observed from two different directions under the same illumination conditions. The colors are normalized according to a calibrated mirror.

3.2.3 Size of samples

The color charts listed in Section 3.1 rely on patches of the following sizes: $100 \times \sim 30 \mu\text{m}$ which needed measurement by microscope, $1 \times 1 \text{ mm}$ adapted to high resolution hyperspectral imaging, and $6 \times 6 \text{ mm}$ adapted to macroscopic measurement by commercial spectrophotometers. We propose to present here these commercial instruments as they are classical tools for the color characterization of printed surfaces. The color measurement by microscope and the hyperspectral bench needed more development and will be presented respectively in Chapters 4 and 5.

3.3 Conventional measurement strategies

Several spectrophotometers or spectro-colorimeters, most often based on the $45^\circ:0^\circ$ or the $d:8^\circ$ geometries, have been developed for industrial applications these last two decades. The advantage of these instruments compared to self-made measurement benches is their calibration process which is optimized. Their drawback is the minimum area that they can measure. Moreover, they are optimal for diffusing surfaces or materials, but generally not for specular ones. Among the instruments available at the Hubert Curien Laboratory, the following ones were used:

The **X-rite Color i7® spectrophotometer** was used to measure samples with a diameter larger than 6 mm in two different geometries: $d:8^\circ$ ⁶³ for the reflectance factor (Lambertian illumination by an integrating sphere, and detection at 8° from the sample's normal by including the specular component), and $0^\circ:0^\circ$ for the transmittance factor (since the samples are mainly nonscattering, even though the sample is illuminated by Lambertian light with the integrating sphere, only the radiance normal to the sample can reach the detector).⁶³

The **X-Rite i1 Pro® spectrophotometer** was used to measure samples with a diameter larger than 6 mm using a 45° annular illumination with normal observation ($45^\circ a:0^\circ$) geometry.⁶⁴

Due to the minimum size limitation and the unavailability of samples larger than 6 mm, these two measurement methods were not sufficient to exhaustively characterize the spectra or colors of the PICSLUP system in the given configurations. Nevertheless, they were useful to perform measurements on selected samples with larger printed areas.

The **STIL REFLET® gonio-spectrophotometer** was used to make measurements of samples with a diameter larger than 3 mm. The device allows adjustable angles of illumination and observation. Unfortunately, due to the high specularity of the samples, the intensity of the light reflected outside of the specular direction was too low to enable accurate measurements. Moreover, the precision in angle position, and the collimation of the incident beam of light were not sufficient.



Figure 3.5: X-rite Color i7® (left) X-rite il Pro® (right) spectrophotometers used for reflection and transmission measurements in specific geometries.

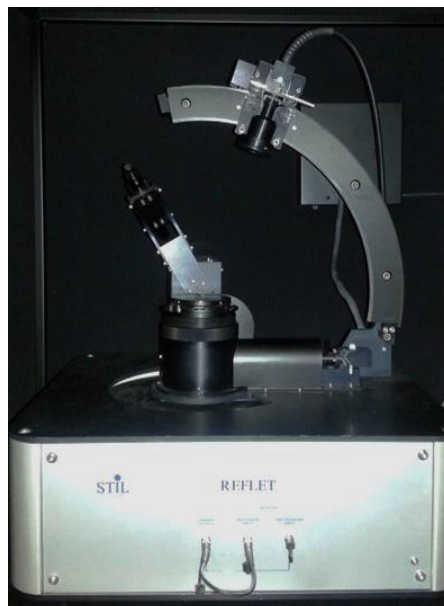


Figure 3.6: STIL REFLET® gonio-spectrophotometer

3.4 Conclusion

The photometric and sample production constraints presented in this chapter posed enormous difficulties to perform a complete color characterization of the samples produced by the PICSLUP system by using conventional measurement methods. Therefore, more elaborated characterization methods based on microscope imaging and hyperspectral imaging are introduced in the following chapters.

4

COLOR

CHARACTERIZATION BY

MICROSCOPE CAMERA

For an exhaustive characterization of the printable colors, a lot of micrometric samples were produced, whose color can be measured only by microscope. The Olympus BX51M microscope used for the laser engraving, shown in Figure 1.2, is also equipped by a IDS UI-2240-C 8-bit RGB digital camera. This allowed us to simultaneously capture the colors obtained by the combination of different laser parameters. However, most microscopes are not optimized for color measurement, especially the one whose nominal application is not the color reproduction. In our case, the microscope presented a strong color deviation due to the lighting systems and the optics. In order to achieve accurate color measurements, we successfully developed a color calibration method described in this chapter. The method allows to transform the raw images obtained from the imaging system into the sRGB⁵² digital color standard, which can be further converted into the XYZ or the CIELAB space.

4.1 Microscope camera color calibration

Imaging acquisition systems, such as cameras or scanners, allow their users to obtain colored spatial information from a scene or object with practical and inexpensive devices. However, the data provided by such systems have to be properly processed in order to obtain accurate color information, because the signals generated by them (normally RGB) are device dependent, i.e., the values obtained from the same scene may be different between different devices. Moreover, the colors recorded by them can also differ from the ones perceived by our eyes, because the spectral responses of the camera sensors are not a linear transformation of the spectral response of the human visual system modeled by the CIE color-matching functions.⁶⁵

In order to have accurate color reproduction and communication, color calibration has to be performed, which consists in building a transformation law between the RGB colors obtained with the device from a set of colored samples (learning samples), and the device-independent values such as CIE-XYZ³⁶ or CIELAB⁶⁶ derived from spectral measurements of the same samples, also referred to as the ground-truth values.

An important factor to obtain accurate color calibration is that the color chart used as learning set and the objects to be captured must be observed under the same lighting conditions and with the same capture settings for the imaging device. As a consequence, in order to prevent saturation or quantization error due to light signal, the color chart and the objects need to have comparable reflectance in the selected illumination-observation geometry. Most of the color charts commercially available, such as GretagMachbeth ColorChecker® or the Calibr8 ColorChart®, are Lambertian, or at least very diffusing. They are therefore not adapted to calibrate devices intended to observe specular surfaces, since their reflectance near the specular direction is generally much higher than the reflectance of a diffuse material. An example of this problem is presented in Figure 4.1. The distribution of reflected light into different components is illustrated in Figure 4.2. Unless the linearity of the responses of the imaging system can be guaranteed and the exposure time adjusted accordingly; the colors of specular samples observed after it has been calibrated using a diffuse color chart, will appear brighter than what they would actually be perceived by the human visual system and in many cases information can be lost due to saturation of the sensors. This problem is especially present in the 0°:0° illumination/observation geometry of a microscope camera since the observation angle is located precisely on the specular reflection angle, where the intensity of the light reflected is maximal.



Figure 4.1: Example of materials with different specularities.

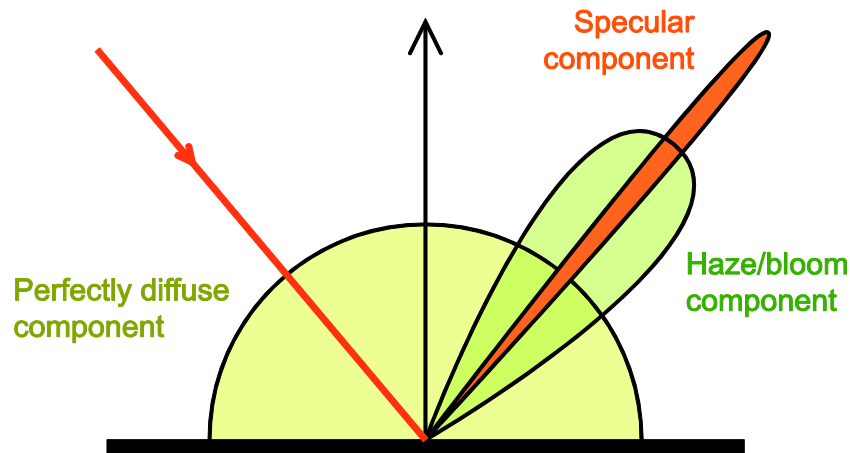


Figure 4.2: Simplified illustration of the reflective components of materials. Diffuse materials have a large diffuse component and a small specular component, whereas specular materials have a strong specular component and a very small diffuse component.

The first difficulty to overcome when calibrating a device for the observation of specular samples is the unavailability of specular color charts. Besides matte color charts, semi-glossy or glossy color charts such as the GretagMacbeth ColorChecker SG® are not suitable either, because the light reflected by their surface, i.e. the gloss, is mostly achromatic, and it is known that a wide number of well distributed colors are necessary for a good color calibration using polynomial transformations.⁶⁷ Moreover, none of the existing color charts is homogenous enough at the microscopic scale to enable the calibration of a microscope camera. We thus tested four different methods to calibrate an imaging system mounted on a microscope that overcome the aforementioned limitations and show that one of them is an efficient alternative to classical calibration methods, with a comparable accuracy. The metric we will use to express the accuracy of our results is the CIE94⁴⁶ color-difference formula, which is one of the most commonly used metrics in literature regarding color calibration and is in better agreement with the human visual system than its widely used predecessor, the CIELAB color-difference formula.⁶⁶

4.2 Microscope printing and imaging system

The imaging device used in our study is illustrated in Figure 4.3. The system consists of an IDS UI-2240-C 8-bit RGB digital camera mounted on an Olympus BX51M microscope, equipped with an Olympus U-TV1x-2 eyepiece with 1× magnification and a 10× objective lens (MPLN from Olympus). The IDS uEye Cockpit software was used with all its automatic corrections disabled to obtain the RGB images. The samples were illuminated at 0° (normal to their surface) by a halogen lamp with a power of 100 W. This imaging system is used for the microscopic laser inscription of samples that exhibit strong and colored specular reflections, and thus require the type of calibration presented in this study to correctly capture the colors displayed by the samples. The system has an additional optical entry for the laser beam used for the inscription of the samples, and two Melles Griot BTF-VIS-50-5001 M-C 50-50 beam splitters corresponding to this entry and to the one of the halogen lamp.

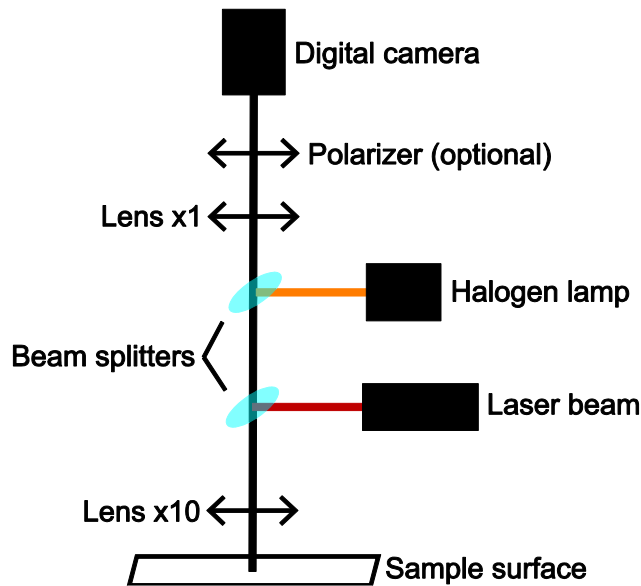


Figure 4.3: Optical scheme of the PICLSUP system used for microscopic laser inscription and imaging.

4.3 Samples used for the calibration

As the imaging system is intended for the observation of highly specular samples, different calibration methods were tested with a set of specular samples specifically defined for this study (testing set). In order to obtain a color chart with colored specular reflections, we used 50 colored ROSCO Supergel® filters and a Newport 10D20AL.2® calibrated mirror. Each of the samples of this color chart is made by placing one of the color filters on top of the calibrated mirror, which allows them to have a strong colored specular reflection. These samples exhibit an adequately regular surface since the microscope is focused on the mirror, which is very homogeneous at microscopic scale.

The color sets used for the learning phase of the calibration vary depending on the method used. There were two different sets of colors used for this purpose: a diffuse color chart and a specular color chart. The diffuse chart was made of 48 pieces of Munsell Matte Color Sheets used in a previous study carried out in our laboratory,⁶⁸ composed of 24 colors of similar appearance to the colors of the standard X-Rite ColorChecker® and 24 additional different colors to increase the color space sampling (shown in Figure 4.4 left).



Figure 4.4: Diffuse/matte (left) and specular (right) calibration samples.

The specular learning color chart was defined using the same procedure as the specular testing set, i.e., by placing colored filters on top of the Newport calibrated mirror, but with a different batch composed of 72 LEE Swatch Book – Numeric Edition® colored filters. The samples ground truth colors in the CIE Chromaticity diagram and in the CIELAB color space are displayed in Figure 4.5. As it can be seen, for each color set, there are a large number of well-distributed samples throughout the color space, which is necessary to obtain a reliable calibration. For example, the absence of dark colors in the calibration set can lead to calibrated images with bad black levels and reduced contrast. In our case, even though there are black or relatively dark samples in the sets, they reflect between 10% and 20% of the incoming light since it is very difficult to obtain an almost perfectly absorbing material. With this limitation in mind, a virtual perfect black was included in the set by assuming a camera response of zero for each channel and a flat spectral of zero to obtain its ground truth color.

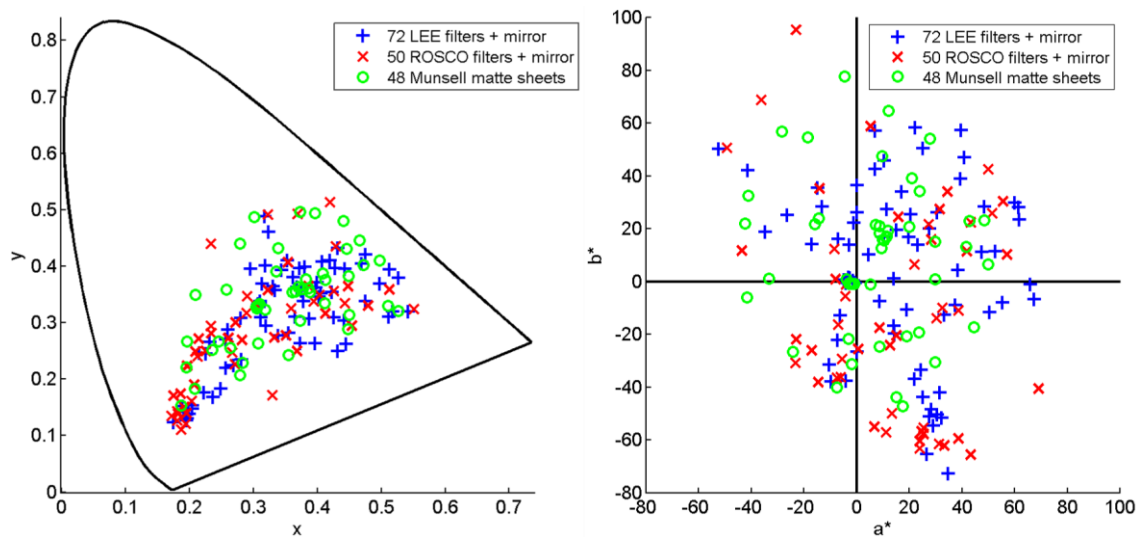


Figure 4.5: Color sample sets used in this study displayed in the CIE Chromaticity diagram (left) and in the a^* - b^* plane of the CIELAB color space (right). The CIELAB L^* values of the samples range from 22.2 to 96.4 units. For clarity, the illuminant used for these plots was D65.

4.4 Ground truth colors of calibration sets

The color calibration process consists in finding a transformation that converts the colors of the samples measured by the uncalibrated imaging system into the real (ground truth) values of the colors of such samples. In order to obtain the ground truth colors, it is necessary to measure the spectral reflectance of each of the samples in the color sets. This can be done with the use of a spectrophotometer by measuring in the visible part of the electromagnetic spectrum, i.e., the wavelengths from 360 nm to 830 nm. These spectral reflectance measurements are used to obtain the color values in a device-independent color system to allow comparisons between measurements obtained by different devices. In this study, CIELAB⁶⁶ was chosen as the device-independent color space to represent the colors since it is the most commonly used color space in studies regarding color calibration. Moreover, the CIE94 color difference, which is the metric used to compare

the performance of the different methods in this study, is based on the CIELAB color space.

To obtain values in the CIELAB color space, it is necessary to calculate the CIE-XYZ values from the spectral measurements beforehand, which requires the spectral power distribution of the used illuminant. The microscope system used in this study is equipped with a halogen lamp whose light passes through several optical components. Measuring its exact spectral power distribution was not possible due to the limited space intended for the placement of the samples. Since the light source is an incandescent halogen lamp, and following the recommendation of the CIE,²⁰ the standard illuminant A was initially assumed as the illuminant of the microscope. As the illuminant A is an instance of an ideal black body radiator with temperature equal to 2856 K, several temperatures values were tested in Section 4.8.2 to evaluate their performance with the different calibration methods proposed.

4.5 Extraction of measured colors from camera images

To obtain the images with the camera, the samples were placed under the microscope and the focus was adjusted by maximizing the sharpness of the image. This adjustment is done each time the position of the sample is changed or a new sample is placed for observation. The camera images were stored in files of 1280×1024 pixels in lossless bitmap image format⁶⁹ (BMP) to avoid color aberrations due to compression. The power of the microscope lamp, the exposure time and the gains of the RGB channels were fixed depending on the calibration method used.

Because the Bayer filters in a color camera are red, green, and blue, and the color images are displayed with red, green, and blue lights on digital displays, the raw values given by the camera are often represented in an RGB space, such as the sRGB⁵² color space. However, each of these raw values is actually the integral of the spectral power distribution of the light signal multiplied by the spectral response of the detector with its corresponding filter, this latter generally having a large passband in the short, middle or large range of wavelengths. The space of the RGB colors obtained by the camera is therefore comparable, although not similar, to the CIE-XYZ³⁶ color space if we consider the color matching functions in place of the spectral response of the detector with filters. Due to this resemblance, and to the fact that the RGB system used by the camera is not specified by the vendor, we approximated the raw (uncalibrated) output values of the camera as CIE-XYZ values.

Even though it is hardly noticeably at simple sight, there is a non-uniform irradiance captured in every image of samples obtained with the microscope. An example of this can be observed in a green sample in Figure 4.6(a). As it can be seen, the colors get darker the further away they are from the center of the sample where the distance to the light source is minimal. To extract the color from an image of a color sample, we assume that the most relevant area of the sample is around the center where the light source is illuminating at its maximum power and perform an arithmetic average over all the pixels inside said area. To minimize the effect of sample irregularities or slight geometrical differences, we first perform a pixel-by-pixel average of all the images taken from all the

samples in the color set. Afterwards, to further reduce noise we apply a mean filtering over the averaged image, based on a 100×100 pixels convolution kernel. Finally, we convert the pixels to CIELAB colors, select the one with highest luminance L^* from them (which we will refer to as c) and then consider only the pixels whose color difference with c is lower than an empirically defined value, in order to obtain an area large enough to be representative of the sample while also being perceptibly uniform. Since the brightness of the image decreases radially from the center of the reflection of the lamp, c was selected as the highest intensity in order to obtain a convex and perceptibly uniform area. An illustration of the area considered for the color extraction for the ROSCO Supergel® color set with the calibrated mirror is shown in Figure 4.6(b). The colors obtained with this procedure are then converted⁶⁶ from the CIE-XYZ color space to the CIELAB color space by using the same illuminant as the one used when obtaining the ground truth values. The approximation of the camera values as CIE-XYZ instead of raw RGB values produced better results with experimental evaluations. Due to time limitations, a detailed study on the benefits and drawback of each of these and other alternatives (such as using cube-root pre-correction) could not be performed.

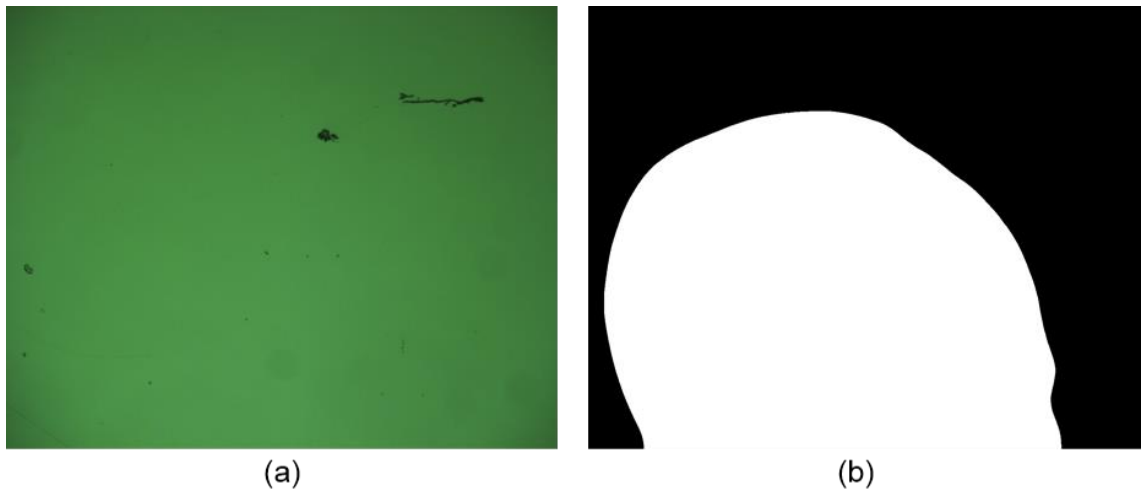


Figure 4.6: (a) Non-uniform irradiance on a sample from the learning set consisting of a ROSCO green filter on top of the calibrated mirror. (b) Area considered for the average color extraction of the samples in the learning set consisting of ROSCO color filters on top of the calibrated mirror. The area corresponds to pixels with color difference lower than 5 CIE94 units with respect to the pixel with the highest CIELAB L^* value.

4.6 Color transformation

Several algorithms have been previously studied to calculate the relationship between device dependent and device-independent spaces in the color calibration of imaging devices, such as: neural networks,⁷⁰ three-dimensional lookup tables,⁷¹ and polynomial transformations.⁶⁷ It has been demonstrated that polynomial transformation and neural networks offer similar performance even though polynomial transformations are easier to implement and require a smaller number of calibration samples to achieve good results.⁶⁸ For that reason, we use a polynomial transformation similar to the one

used in a previous study,⁶⁸ by also performing, in addition to the 3rd degree polynomial fitting, 2nd and 4th degree fittings in order to study the effects of polynomial overfitting.

4.6.1 Polynomial transformation

The color calibration based on polynomial transformation aims at finding a transformation matrix able to convert the colors measured by the uncalibrated camera into the ground truth colors of the same samples computed from spectral reflectance measurements. We thus use a color chart containing several patches. For each patch i , we define color vectors in the CIELAB color space. The ground truth CIELAB values obtained from spectral measurements are denoted by the vector $\mathbf{G}_i = (L_{G,i}, a_{G,i}, b_{G,i})$ and those obtained from the images taken with the uncalibrated camera are denoted by the vector $\mathbf{C}_i = (L_i, a_i, b_i)$. Then, for higher order polynomial regression, an augmented vector \mathbf{A}_i is defined from the entries of \mathbf{C}_i as shown in Table 3. The matrix \mathbf{M} is the matrix that transforms each vector \mathbf{A}_i into a vector $\mathbf{E}_i = (L_{E,i}, a_{E,i}, b_{E,i})$, whose entries are as close as possible to the ground truth CIELAB values according to the goal function in Equation (34). The transformation is obtained by the product of \mathbf{M} and the transpose of \mathbf{A}_i :

$$\mathbf{E}_i = \mathbf{M} \cdot \mathbf{A}_i^T \quad (33)$$

The sizes of vector \mathbf{A}_i and of matrix \mathbf{M} depend on the polynomial transformation order. They are given in Table 3 for transformation orders from 1 to 4.

Table 3: Dimensions of matrix \mathbf{M} and vector \mathbf{A} , and elements of vector \mathbf{A} depending on the polynomial order. Note that \mathbf{A} has only one row of elements.

Order	Size of \mathbf{M}	Size of \mathbf{A}	\mathbf{A}
1	3×4	1×4	$(1, L, a, b)$
2	3×10	1×10	$(1, L, a, b, L^2, La, Lb, a^2, ab, b^2)$
3	3×20	1×20	$\left(1, L, a, b, L^2, La, Lb, a^2, ab, b^2, L^3, L^2a, L^2b, La^2, Lab, Lb^2, a^3, a^2b, ab^2, b^3 \right)$
4	3×35	1×35	$\left(1, L, a, b, L^2, La, Lb, a^2, ab, b^2, L^3, L^2a, L^2b, La^2, Lab, Lb^2, a^3, a^2b, ab^2, b^3, L^4, L^3a, L^3b, L^2a^2, L^2ab, L^2b^2, La^3, La^2b, Lab^2, Lb^3, a^4, a^3b, a^2b^2, ab^3, b^4 \right)$

The polynomial transformation for each color sample becomes a system of equations with a number of variables equal to the number of entries of \mathbf{M} . These entries are calculated by minimizing a function σ which corresponds to the sum of the CIE94 color differences between \mathbf{G}_i and \mathbf{E}_i for all patches i in the learning set, combined with an

additional penalty term introduced to favor lower polynomial order solutions and in this way avoid overfitting when possible:

$$\sigma = \sum_{i=1}^N \Delta E_{94}(\mathbf{G}_i, \mathbf{E}_i) + \sum_{j=1}^3 \sum_{k=1}^N \left| \mathbf{M}_{j,k} \cdot \text{ord}(\mathbf{A}_i, k)! \right| \quad (34)$$

where $|p|$ is the absolute value of real number p , $\text{ord}(\mathbf{S}, k)$ denotes the polynomial order of the k^{th} element of vector \mathbf{S} , and $n!$ is the factorial of integer n .

The calculation of the coefficients in the transformation matrix \mathbf{M} in order to minimize σ is performed with the iterative function *fminsearch* of the MATLAB® software, which uses the Nelder-Mead Simplex Method. The *fminsearch* function requires an initial solution in order to improve it towards the local optimum. In the first iteration, we use the least square regression method to minimize the Euclidean distance between \mathbf{G}_i and \mathbf{E}_i since its computation cost is low and its results are not very far from the optimal values. After each iteration, we keep the best solution found so far and then slightly modify it to use it as a new initial solution for the *fminsearch* function. The modification consists in introducing some noise to each element by adding a random number between -10% and +10% of their current value. This mutation range was empirically chosen to allow enough change of the solutions without going unnecessarily far from the optimum. Since the solutions tend to converge rapidly, a number of 30 iterations was selected. No significant improvement of the calibration was achieved by using higher number of iterations.

4.6.2 Applying the color calibration

Once the optimal transformation matrix \mathbf{M} is obtained from the color patches of the learning set, the correction process can be applied to any other measured color, i.e. to each pixel of an image captured by the camera. We assume that the three channels of the camera correspond to uncalibrated CIE-XYZ values. For a given CIE-XYZ color of a pixel P measured by the uncalibrated camera, the following procedure is applied:

- 1) Convert the pixel values from the CIE-XYZ color space to the CIELAB color space;
- 2) Compute the augmented vector \mathbf{A} from the obtained CIELAB values depending on the selected polynomial order;
- 3) Compute the corrected color vector \mathbf{E} by multiplying the transformation matrix \mathbf{M} with the transpose of the vector \mathbf{A} as shown in Equation (33);
- 4) Finally, the corrected CIELAB colors can be converted to any color space such as the most commonly used digital standard sRGB by applying standard conversions between these color spaces.⁵²

4.7 Color calibration methods

As previously mentioned, the purpose of this study is to calibrate a microscopic imaging system intended for the observation of highly specular materials. To accomplish

this goal, four different methods were explored: The first two are naïve approaches based on performing a classical color calibration with the use of a diffuse color chart; and the third and fourth methods are more elaborated approaches involving the learning specular color sets defined in this study. All the methods were tested by using the specular color testing set described in Section 4.3. An overview of the methods described in this study is shown in Table 4.

4.7.1 Adjustment of exposure time and color channel gains

In the four methods, a pre-calibration white balance is performed by adjusting the exposure time and the gains of the color channels of the camera in order to decrease the difficulty of the polynomial transformation to find acceptable solutions. The exposure time and color gains in this imaging system are analog settings and modifying them in the analog domain reduces the quantization errors that could arise when trying to simulate them in the digital domain. The white balance consists in observing the white sample of the current learning color set, followed by adjusting the gains of the color channels until their responses are approximately the same, while also adjusting the time exposure to maximize such responses without saturating any of the channels. The maximization step is done to take advantage of all the dynamic range of the system and minimize the loss of information due to low signal levels and quantization.

4.7.2 Ground truth measurement

To obtain the ground truth values of the color sets in the first, second and third methods, the spectral reflectance of the samples was measured with an X-rite Color i7® spectrophotometer based on the CIE diffuse d:8° sphere geometry. The difference in geometry with respect to the microscope only introduced minor color changes in the measurements of the calibration samples. In the fourth method, the spectral reflectance was measured by using the Ocean optics USB-650 spectrophotometer, based on the 0°:0° illumination/observation geometry with the optical setup described in Section 4.7.6.

4.7.3 First method: Diffuse learning set and exposure time decrease

The first method consists in the following steps:

- 1) The power of the lamp of the microscope is set to the maximum.
- 2) The parameters of the camera are adjusted as explained in Section 4.7.1 by using the white color patch of the learning color set consisting of 48 Munsell matte color sheets.
- 3) The color transformation matrix M is calculated by using as input the same learning color set as in Step 2.
- 4) To test the robustness of the calibration, the lamp is adjusted to exactly the same power as the one used for the learning set, and the parameters of the camera are adjusted again following the steps in Section 4.7.1 but this time by using the white patch of the testing set, which in our case is specular. This procedure results in an exposure time lower than the one used for the learning set, in order

to normalize the response of the color channels to the higher intensity due to the strong specular reflection.

- 5) The transformation matrix M obtained from the learning set is applied to the testing set camera images with the procedure explained in Section 4.6.1. Their average colors are extracted and compared to the ground truth colors of the testing color set.

4.7.4 Second method: Diffuse learning set and lamp power decrease

The only difference between the second method and the first method is the step number 4:

- 4) To test the robustness of the calibration in the second method, the parameters of the camera are adjusted to exactly the same values as the ones used with the learning set, and in this case the power of the lamp of the microscope is adjusted in order to maximize the responses of the color channels but paying attention not to saturate any of them. Since the testing set consists of specular samples, this will result in a lower lamp power as the one used for the learning set.

4.7.5 Third method: Specular learning set

The steps 1 and 5 are the same as in the previous methods. The remaining steps are as follows:

- 2) The parameters of the camera are adjusted as explained in Section 7.1 by using the white color patch of the color set consisting of 72 LEE color filters on top of the calibrated mirror.
- 3) The camera is calibrated by using the same color set as in Step 2.
- 4) As in this case both the learning and testing sets of colors are specular, to test the robustness of the calibration, the system is adjusted to exactly the same parameters of the camera and power of the lamp used with the learning set.

4.7.6 Fourth method: Optical bench with $0^\circ:0^\circ$ geometry

Lastly, the fourth method is exactly the same as the third method except for the ground truth values of the color sets involved, which were calculated in a different manner. The spectral reflectance measurements were done by using an optical set-up that reproduced the $0^\circ:0^\circ$ illumination-observation geometry of the microscope, in which the samples are illuminated and observed at the normal of their surface. This optical measurement configuration is illustrated in Figure 4.7. The setup consisted of a HL-2000-HP 20W halogen light source from Edmund Optics with an optical fiber whose output was placed in front of a lens to create a collimated beam of light and thus maintain a consistent illumination angle. The light passed through a 50-50 beam splitter before illuminating the sample with a normal incidence angle. As mentioned before, each sample is made by placing a different color filter in contact with the calibrated mirror. The reflected light from the sample passed again through the beam splitter and then through a telecentric lens made of two lenses and one aperture. Finally, the light passed through an

additional lens to focus the beam on an optical fiber connected to a USB2000 spectrophotometer from Ocean Optics.

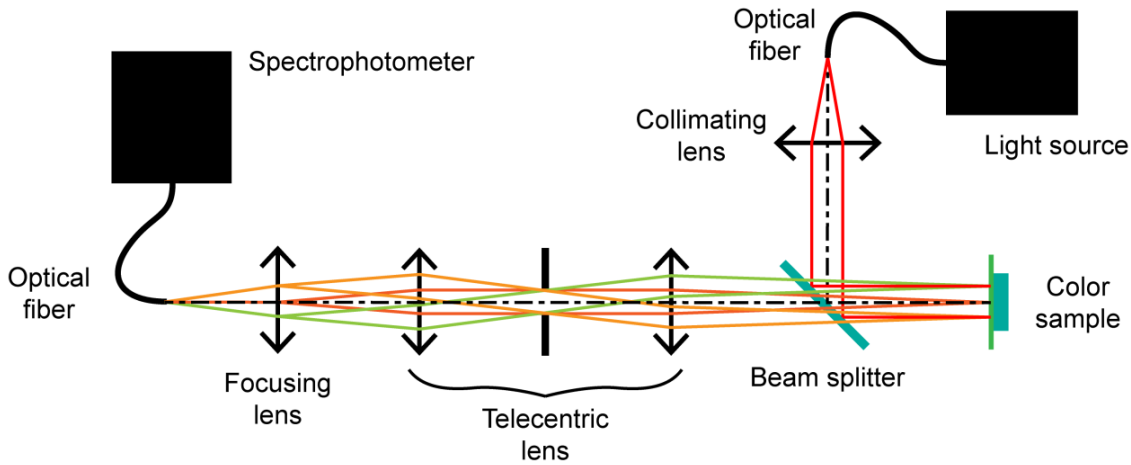


Figure 4.7: Optical setup based on the $0^{\circ}:0^{\circ}$ geometry used to obtain the spectral measurements of the samples in order to obtain the ground truth color values with the fourth method.

Table 4: Overview of the four calibration methods used in this study.

	Method 1	Method 2	Method 3	Method 4
Learning set	48 matte Munsell	48 matte Munsell	72 LEE filters placed on mirror	72 LEE filters placed on mirror
Testing set	50 ROSCO filters placed on mirror			
Ground truth measurement device and geometry	X-rite Color i7@ d:8°	X-rite Color i7@ d:8°	X-rite Color i7@ d:8°	Ocean optics USB-650 0°:0°
Learning time exposure	Initial	Initial	Initial	Initial
Testing time exposure	Reduced	Initial	Initial	Initial
Learning lamp power	Maximum	Maximum	Maximum	Maximum
Testing lamp power	Maximum	Reduced	Maximum	Maximum

4.8 Color calibration results

The accuracy of the calibration is determined by the average CIE94 color difference between the ground truth color values and the colors obtained from the calibrated images of the samples used. The results of the color calibration obtained with each of the four methods by assuming an A illuminant (i.e. a black body illuminant of 2856 K temperature) are shown in Table 5. From the four methods used, the third one had the best performance by a significant margin. It is important to note that even though some of the methods give good results regarding their learning sets, they give poor results

regarding the testing sets, which can be a consequence of overfitting or errors due to different camera settings between the learning and testing measurements.

Table 5: Average CIE94 results obtained with each of the four methods by assuming an A illuminant (i.e. a black body illuminant of 2856 K temperature).

Polynomial order	2 nd order		3 rd order		4 th order	
	Learning ^a	Testing ^b	Learning ^a	Testing ^b	Learning ^a	Testing ^b
Method 1	2.27	14.53	2.04	14.76	1.33	19.87
Method 2	2.28	16.73	1.60	24.92	1.48	24.98
Method 3	2.18	<u>2.47</u>	1.94	<u>2.86</u>	1.63	<u>3.50</u>
Method 4	2.76	3.86	2.27	4.01	2.12	4.21

^acalibration tested with the learning set of samples used to obtain the polynomial transformation matrix.

^bcalibration tested with a different set of samples than the learning set. The best testing results obtained for each polynomial order are underlined.

Although the first two methods obtained fairly good results regarding the color set used to obtain the transformation matrix (learning set), the results obtained with the testing color sets were highly unsatisfactory. Therefore, it is evident that the first two naïve methods are not acceptable choices to perform a color calibration of an imaging device intended for the observation of highly specular samples. The first method obtains the transformation matrix from a set of matte samples and afterwards the exposure of the camera is adjusted to the strong reflectivity of specular testing samples. The main source of error for this method is that the responses of the sensors are non-linear which was experimentally verified but, due to time limitations, a detailed evaluation of the exact properties of the non-linearity remains for a future study. Due to the non-linearity, the polynomial transformation obtained with the exposure time used with the learning set does not correspond to the polynomial transformation that would be needed for the lower exposure time used with the testing set. On the other hand, the second method obtains the transformation matrix from the same learning set of matte samples and then the power of the lamp of the microscope is decreased in order to adapt the intensity of the reflection from the learning samples to the same exposure time conditions used with the learning set. Some of the main causes of bad performance with this method were the lack of accurate adjustability of the power of the lamp, which did not allow a precise adjustment according to the white sample of the testing set. Furthermore, the modification of the power of a halogen lamp induces a change in the spectral power distribution of the light which in consequence changes the chromaticity of the colors of the samples observed.

Unlike the first two methods, the third and fourth method have unchanged exposure time and lamp power settings throughout the whole calibration process, thus reducing the number of factors affecting the color transformation process, which is reflected in their performance regarding the testing sets. The only difference between the third and fourth method was the device used to measure the ground truth colors of the calibration sets. Despite the fact that the optical setup used in the fourth method resembled more closely

the illumination/observation geometry of the microscope's imaging system, the superior performance of the third method could be due to a higher consistency throughout the measurements of all the samples used. The spectrophotometer used in the third method allows the samples to be pressed against the measurement aperture, which makes the surface of the color filters parallel to the one of the mirror. In the fourth method, the color filters were placed in contact with the mirror but they were not perfectly parallel, introducing slight geometric inconsistencies between measurements in the same color set. In addition, there could have also been small optical misalignments in the setup, which have significant consequences in the case of specular reflectors.

4.8.1 Influence of the polynomial order

Similar to what has been found in previous polynomial fitting studies,^{67,72} higher polynomial order of the calibration allowed a better correction of the colors used for the learning phase of the process, but it also increased the risk of overfitting, where only the samples fitted are modeled and not the underlying relationship between them, which causes the calibration to make erroneous transformations of colors different from the ones used in the learning phase. This can be clearly seen in the results obtained in this study (Table 5 and Table 6), where the higher the polynomial order is, the better the results are regarding the learning color set but the worse the results are regarding the testing set. It is evident that overfitting is present in the fourth order polynomial transformations; hence, those results (along with the ones of the first two methods) will be omitted in Section 4.8.2.

4.8.2 Influence of the color temperature of the illuminant

As previously mentioned, the initially assumed color temperature of the illuminant of the imaging system was 2856 K, corresponding to the A illuminant recommended for incandescent light sources. As the actual color temperature of the light source in our system cannot be measured due to space and equipment limitations, we tested the calibration performance by assuming different color temperatures of an ideal black body radiator and the results for the third and fourth method can be seen in Figure 4.8. The color differences obtained were lower for color temperatures around 1800 K. Taking this into account, we performed the calibration again with the four methods assuming a blackbody illuminant of 1800 K (Table 6) and obtained an average CIE94 color difference of 1.93 units with the third method using the 2nd polynomial order transformation.

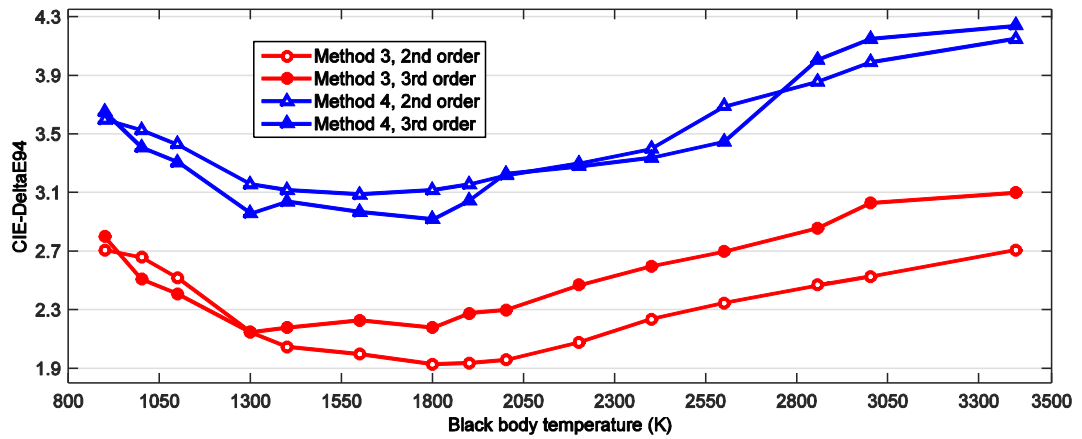


Figure 4.8: Average calibration results regarding the testing set, by assuming different color temperatures of a black body illuminant with the third and fourth calibration methods.

Table 6: Average CIE94 results obtained with each of the four methods by assuming a black body illuminant of 1800 K temperature.

Polynomial order	2 nd order		3 rd order		4 th order	
	Learning ^a	Testing ^b	Learning ^a	Testing ^b	Learning ^a	Testing ^b
Method 1	2.05	15.29	1.25	20.38	1.25	20.65
Method 2	2.06	16.03	1.38	21.33	1.26	21.69
Method 3	1.87	<u>1.93</u>	1.64	<u>2.18</u>	1.46	<u>2.69</u>
Method 4	2.27	3.11	1.99	3.05	1.89	3.38

^acalibration tested with the learning set of samples used to obtain the polynomial transformation matrix.

^bcalibration tested with a different set of samples than the learning set. The best testing results obtained for each polynomial order are underlined.

4.9 Conclusion on color calibration

The study of the color camera calibration was motivated by the necessity of measuring the color of highly specular samples under constrained illumination and observation conditions, imposed by the microscope. A complete comparison between the methods has been carried out, permitting an interesting discussion on the influence of different parameters on the calibration accuracy of each method, such as the diffusing properties of the color chart, and the polynomial order of the color transformation. Through our experiments, we conclude that the third method with 2nd order degree polynomial fitting is the most accurate. By comparing the colors recorded by the device after transformation and those measured from our set of 50 specular testing samples, we obtained an average CIE94 color difference of 1.93 units. This is a good performance in comparison with previous studies based on diffusing materials,^{68,73,74} where results between 2.2 and 3.0 units of CIE94 color difference were obtained. This method has been published in the international peer-reviewed conference SPIE Electronic Imaging 2015¹³

and is already being used for color measurements of photochromic dyes created by laser insolation of clear plates.¹¹

4.10 Extraction of color information from calibrated images

Thousands of lines were systematically printed at micrometric scale in order to characterize the colors produced by the PICSLUP system in the specular $0^\circ:0^\circ$ used by the microscope. The lines were made with all the combinations of the following laser parameters:

- 4 wavelengths: 488, 514, 530, and 647 nm
- 4 laser powers: 300, 400, 500, and 600 mW
- 18 focusing distances (from the focusing plane): from 0 to 3.8 mm
- 37 translation speeds: from 300 to 30000 $\mu\text{m/s}$

Numerous images of the printed samples were obtained, such as the ones shown in Figure 4.9. The relative positions of the lines in the images were preserved thanks to a controlled mechanical translation system. The lines are connected horizontally and a total of 20 different lines were captured per image.

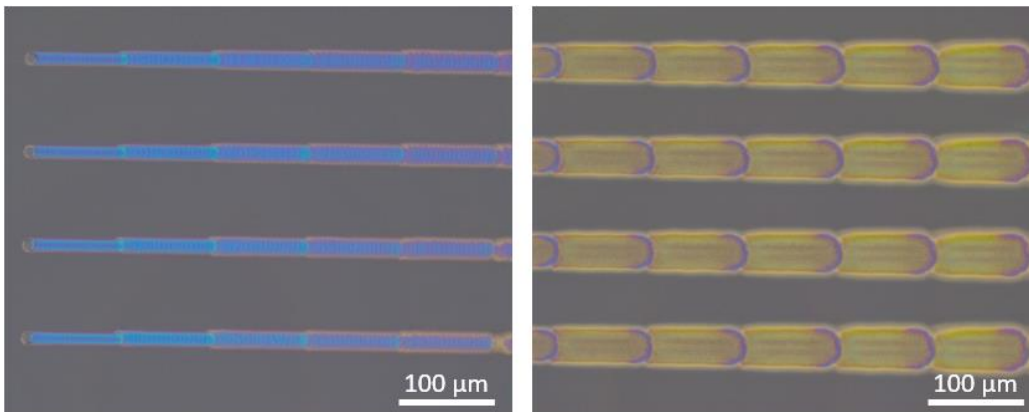


Figure 4.9: Microscope images containing 4 rows and 5 columns of printed lines for a total of 20 different combinations of laser parameters per image.

After the calibrated images were converted to the sRGB system, the following image processing method was used to separate the lines from the background in order to extract their color:

- 1) Since the relative positions of the lines in the image and their length are known, a cropped image is automatically extracted containing the line whose color needs to be extracted. Note that the background of the sample covers a large area of the image, which is required for step 3.
- 2) The image is blurred with an 3×3 Gaussian kernel to reduce noise and homogenize the edges of the lines.
- 3) The sRGB color of the background is estimated by extracting the median sRGB color of the image.

- 4) The estimated sRGB values of the background is transformed to the CIELAB color space by using the standard illuminant for sRGB, i.e., D65.
- 5) The image is also transformed to the CIELAB space by converting each of its pixels in the same manner. These conversions are done because the CIELAB color space is more appropriate for color difference perception evaluations.
- 6) In order to separate the printed areas from the background, a binary image is created, where the white pixels are those whose CIE94 color differences with the color of the background are larger than an empirically-defined threshold.
- 7) To make the segmentation more robust, a morphological close operator is applied to the image in order to connect areas that were separated due to printing defects or scratches.
- 8) The connected components with fewer than 100 pixels are removed, in order to clean the image from detected regions that were not part of the sample, mainly due to printing defects or dust.
- 9) The holes in the image are filled by converting all black regions that are not connected to the edge into white.
- 10) Since the position and length of the lines are known, only the pixels in a central range are selected, and the colors in the same locations in the original image are extracted and averaged.

An example of the color extraction of a line is shown in Figure 4.10. We preferred excluding the left and right boundaries of the lines in order to discard the color irregularities that arise because of the acceleration and deceleration of the translation stage at the beginning and ending of the colored marks. These irregularities on the left and right edges become negligible at a macroscopic level as the lines become longer, whereas the colors of the top and bottom edges, which are considered, affect the overall color independently of the length or number of marked lines.

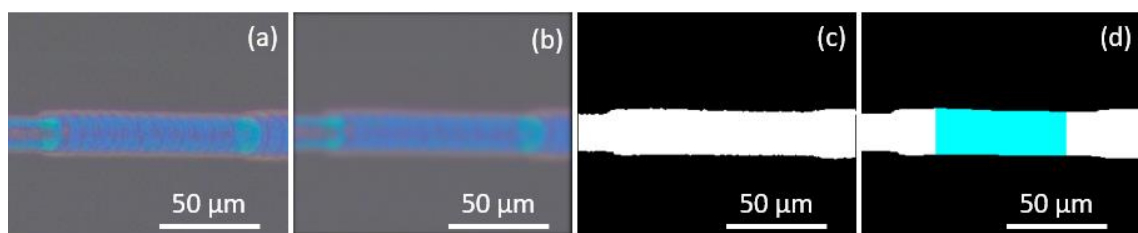


Figure 4.10: Different stages in the color extraction from one of the lines in the left image of Figure 4.9. (a) Step 1: Image cropped around the target line. (b) Step 2: Image blurred to reduce noise. (c) Steps 3 to 9: Different steps to separate the line from the background. (d) Step 10: Pixels to be extracted and average from the original image.

Thanks to the color calibration of the microscope camera described in Section 4.1, and the method developed to extract colors from micrometric printed lines, advances were made in the characterization of the PICSLUP technology in the specular direction, particularly in the $0^\circ:0^\circ$ geometry.

4.11 Color gamut in the 0°:0° specular reflection geometry

From the exhaustive measurement of the thousands of lines printed with different parameter combinations of the PICSLUP system, we can make an estimation of all the colors that can be produced by this technology in the given illumination/observation conditions, which is also referred to as the *color gamut*. Figure 4.11 displays all the colors obtained with the microscope imaging system converted into the CIELAB color space.

In order to evaluate the volume of the colors obtained, we compare it with the color gamut of typical offset and inkjet printing systems in Figure 4.12. As it can be seen, the color gamut of the PICSLUP system has a broad range of values of hue and chroma. However, the colors obtained are mainly located in the lightness range between 45 and 65 L* units (for comparison, the unprinted support measured in the same conditions has a lightness of about 40 L* units). Furthermore, it can be noted that there is an absence of colors in the green-cyan hues. Both of these factors can affect the contrast and color accuracy of the images produced by the system.

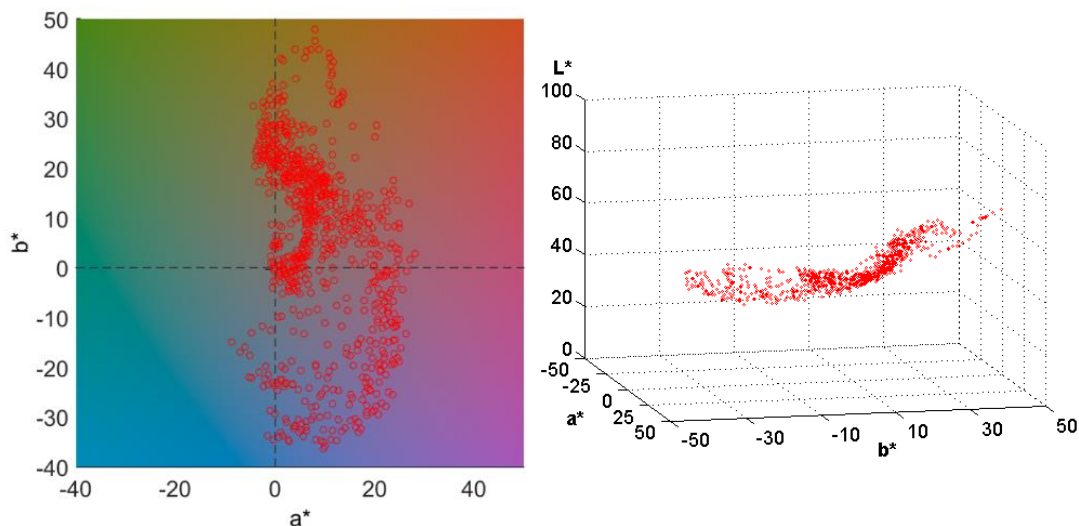


Figure 4.11: Colors obtained with a controlled combination of elaboration parameters, and measured by a color-calibrated microscope in the 0°:0° illumination/observation geometry. The colors are represented in the CIELAB color space by assuming a D65 illuminant. The reference colors in the background of the left image were calculated by fixing a lightness value L* of 50 units.

4.12 Influence of polarization and printing parameters

As it was previously mentioned, the colors produced by the PICSLUP system are sensitive to the use of polarization. Figure 4.13 shows the colors obtained by measuring 9 different samples with the calibrated microscope while a polarizer placed in front of the detector is rotated between 0° and 180°. The irregularities of the lines are due to the low intensity of the light in some polarization angles.

As it can be observed, the reproducible regions of the color space (color gamut of the system) have considerably increased with the use of polarization with only a few tested samples, which suggests that an even greater coverage can be obtained with a more exhaustive evaluation.

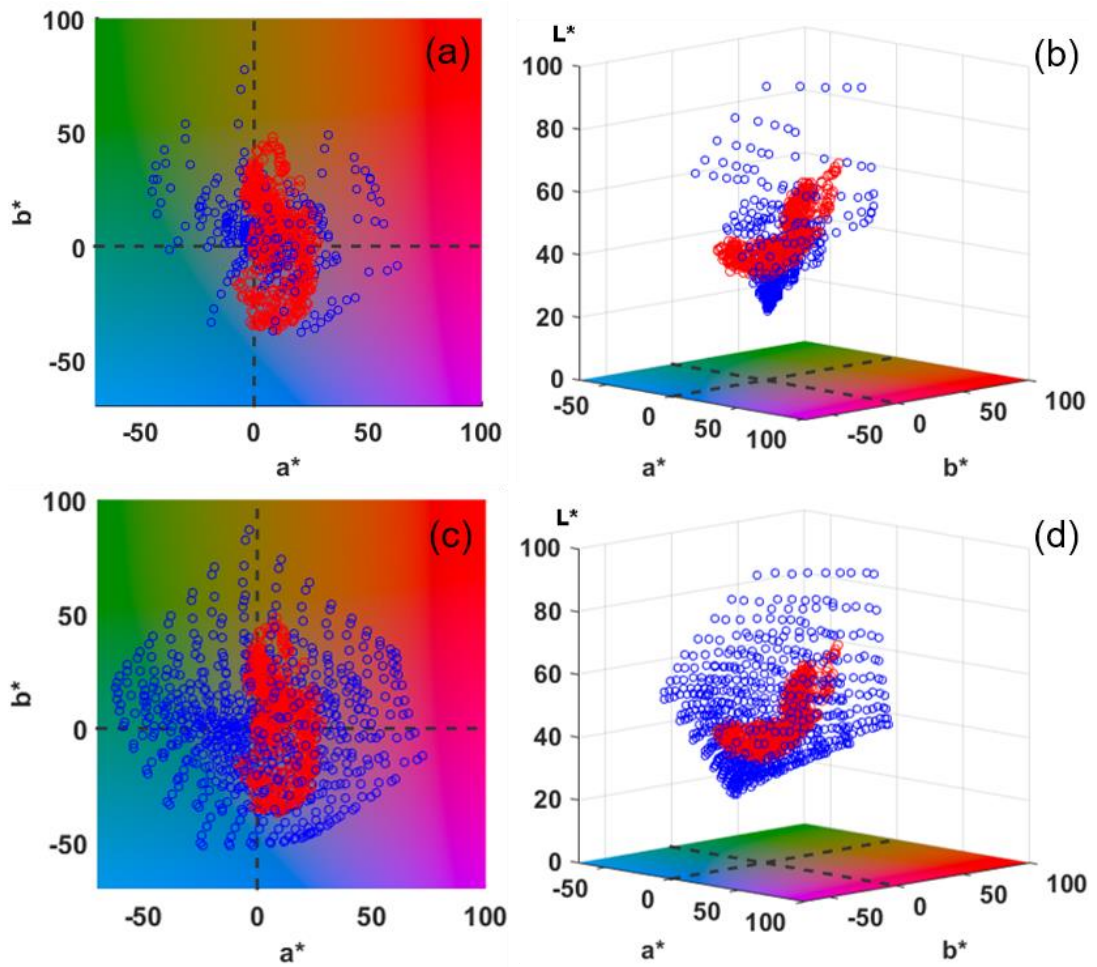


Figure 4.12: Color gamut of the PICSLUP system in the $0^\circ:0^\circ$ geometry (red) compared to the color gamut of two typical printing systems (blue): (a,b) offset printer, and (c,d) inkjet printer. The reference colors in the background of the plots were calculated with a D65 illuminant and a lightness value L^* of 50 units.

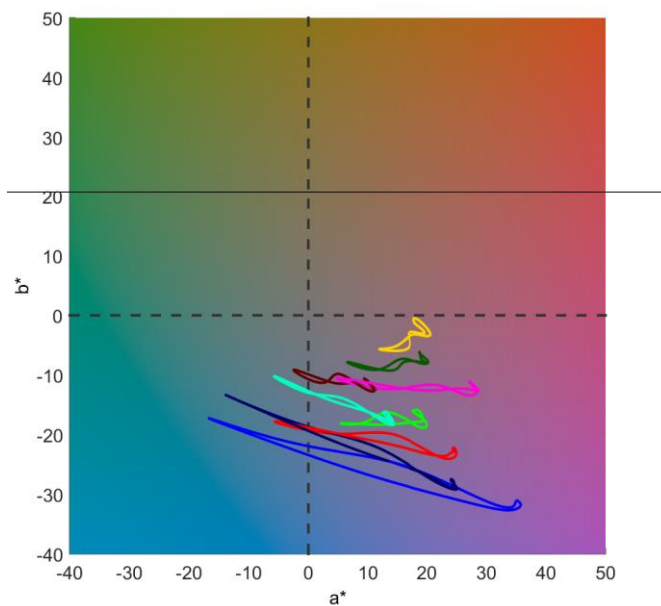


Figure 4.13: Color variation in the CIELAB a^*b^* -plane of 9 different samples observed in the $0^\circ:0^\circ$ geometry, when rotating a polarizer between 0° and 180° . In each curve, 0° and 90° correspond to the left and right extrema, respectively.

Another interesting property of the samples produced by the PICSLUP system is that some of them are very dichroic, i.e. their color is affected very differently by two directions of polarization: parallel to the nanoparticle grating lines (TE polarization) and perpendicular to the grating lines (TM polarization). In Figure 4.14 we show the colors measured for TE and TM polarizations and study the influence of three main parameters, which are the translation speed of the sample, the laser wavelength, and focusing, on the dichroism. When the red and blue curves are close to each other, the dichroism is low, and it increases when the red and blue curves diverge. When the curves are long, the color strongly varies with speed. These measurements suggest that moving the sample away from the focal plane of the objective lens, as well as using longer wavelengths, strongly deteriorate the dichroism.

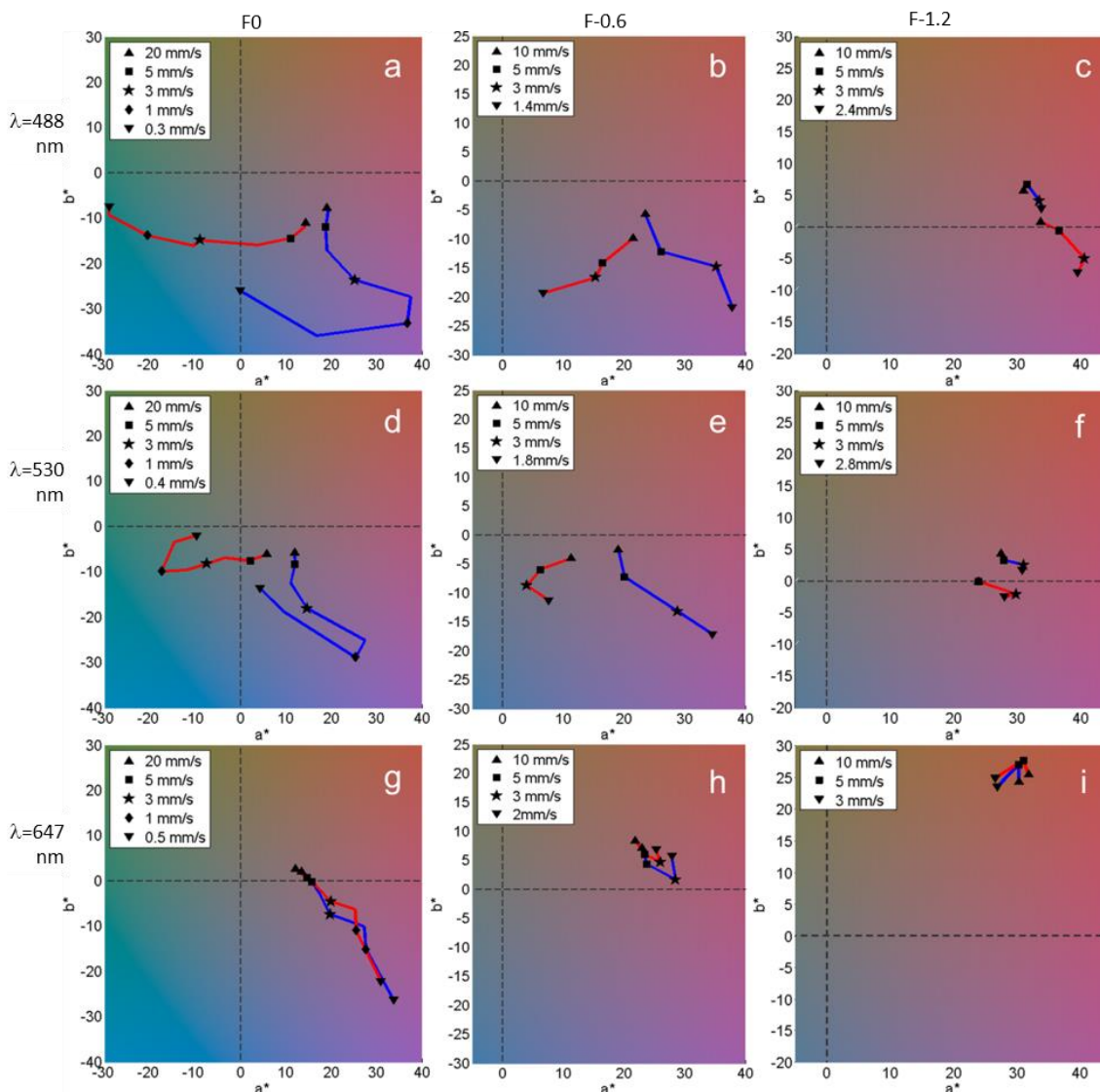


Figure 4.14: Color change in the CIELAB a^*b^* -plane of PICSLUP prints as a function of wavelength (one wavelength λ per row), focusing conditions (the same focusing on each column), and speed (varies in each CIELAB a^*b^* -plane), for TE (red curve) and TM (blue curve) polarizations.

4.13 Conclusion

A color calibration method was developed for a microscope imaging system in order to exhaustively characterize the colors produced by the PISCLUP system in the $0^\circ:0^\circ$ specular reflection configuration. A good accuracy was achieved by the method in comparison with previous studies based on diffusing materials. From the color calibrated images, the colors of numerous printed lines were extracted thanks to a segmentation method. and the color gamut of the system was estimated and compared to that of typical offset and inkjet printing systems, showing a good range of hue and chroma values, but a very low variation in terms of lightness. The results presented in this chapter, illustrate the complex color change that can be obtained from the system in just one geometrical configuration, and led us to investigate other methods in order to continue characterizing the colors in different viewing conditions.

5

CHARACTERIZATION BY HYPERSPPECTRAL IMAGING

Although the measurements with microscope imaging in the $0^\circ:0^\circ$ specular geometry are very useful to study the properties of the colors produced by the PICSLUP technology, they are not sufficient to fully characterize the system, since the samples exhibit very different colors according to the respective positions of the viewer and the light source. Moreover, the $0^\circ:0^\circ$ geometry is not the most convenient for visual characterization since in practice the observer and the light source are never exactly in the same place. In order to be able to measure the spectral information (and ultimately the colors) in different observation and illumination configurations, we developed a hyperspectral imaging system installed on an optical bench illustrated in Figure 5.1.

5.1 Hyperspectral imaging setup

The system consists of two horizontally rotatable arms: one supporting the light source of the system, and the other one holding a B&W 12-bit intensity camera placed in front of a rotating filter wheel with 16 slots. A set of 31 interferential filters were used, each with a bandwidth of 10 nm, consisting of wavelengths from 400 to 700 nm in steps of 10 nm, thus two full wheel measurements were required in order to obtain images with all the 31 filters. The spectral transmittances of the filters are displayed in Figure 5.2. The sample to be measured is placed in the axial intersection of the two adjustable arms on a rotating platform, which also allows the angle of the sample to be adjusted. The camera captures images of an area of approximately 35×25 mm, with a resolution of 1024×768 pixels, which is focused on the sensor thanks to the two lenses featured in the capturing arm which form together a telecentric lens. The respective foci of these two lenses meet each other, while the sample and the detector are located in the focus planes of the first lens, and respectively the second lens.⁷⁵ The advantage of the telecentric lens is that all points on the sample are viewed by the camera under exactly the same angle, thus

preventing obliquity issues at the border of the image, which would be a drawback with the goniochromatic samples that we want to analyze.

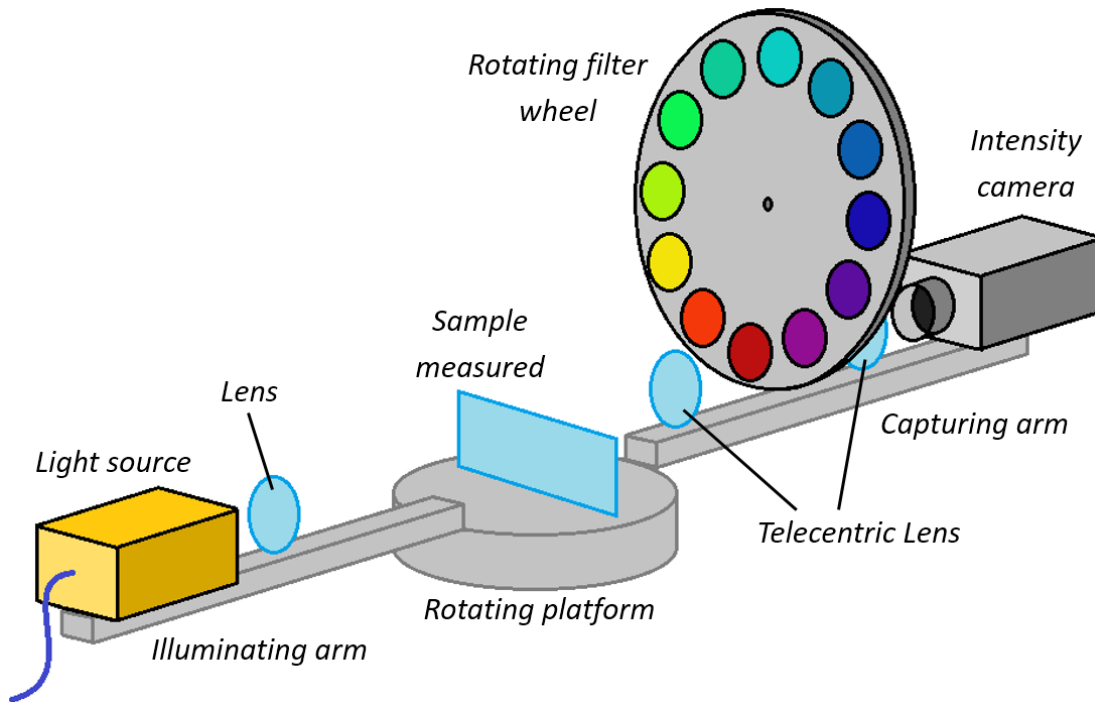


Figure 5.1: Scheme of the hyperspectral imaging system.

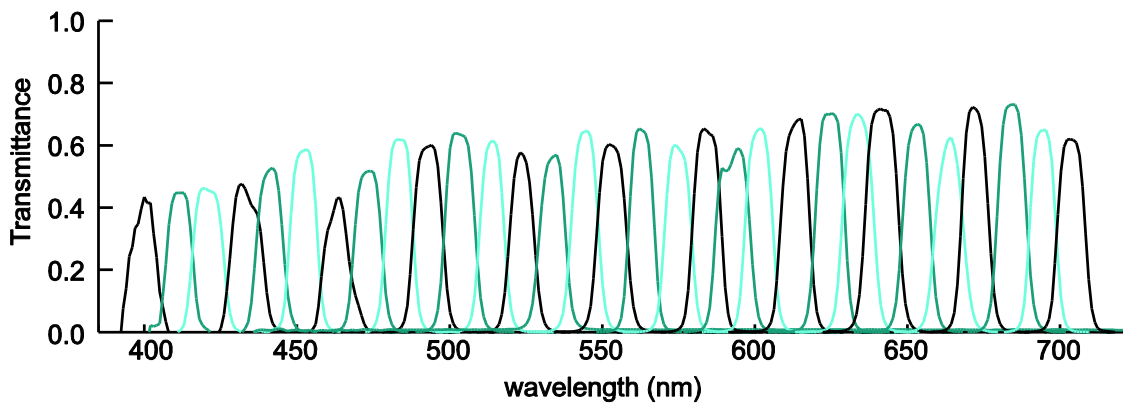


Figure 5.2: Spectral transmittances of the 31 interferential bandpass filters.

By making images of the considered sample and of a white reference reflector/transmitter in each waveband, we can obtain an image with a spectral reflectance/transmittance factor in each pixel. The hyperspectral system is capable of doing measurements in adjustable illumination/observation settings. The process used for capturing hyperspectral images in transmission, specular reflection, and off-specular reflection, is described in the following sections.

5.2 Exposure time and white reference

The interferential filters used to obtain spectral measurements have a wide variation in the fraction of light they transmit. Moreover, the light sources used for the experiment

also have varying radiances as a function of their wavelength. Both of these factors mean that the radiance arriving to the camera sensor can vary widely depending on the used bandpass filters.

In order to avoid saturation of the sensor by receiving too high radiance, and avoid quantization noise by receiving too low radiance, the exposure time of the camera was normalized separately for each of the 31 wavelengths, by maximizing the signal obtained from a “white reference” without saturating the sensor of the camera. This reference corresponds to a material resulting in the maximum signal expected depending on the geometrical configuration used and the types of samples to be measured. The same normalized settings are used afterwards to obtain images from such samples.

5.3 Hyperspectral images in transmission

The geometrical configuration of the system for transmission measurements is illustrated in Figure 5.3. The illuminating and capturing arms are placed parallel to each other and the sample is oriented perpendicular to the arms. The light source is an HL-2000-HP 20W halogen lamp by Ocean Optics; the light is brought by optical fiber to the focus of a lens, thus creating a collimated beam of 4 cm diameter.

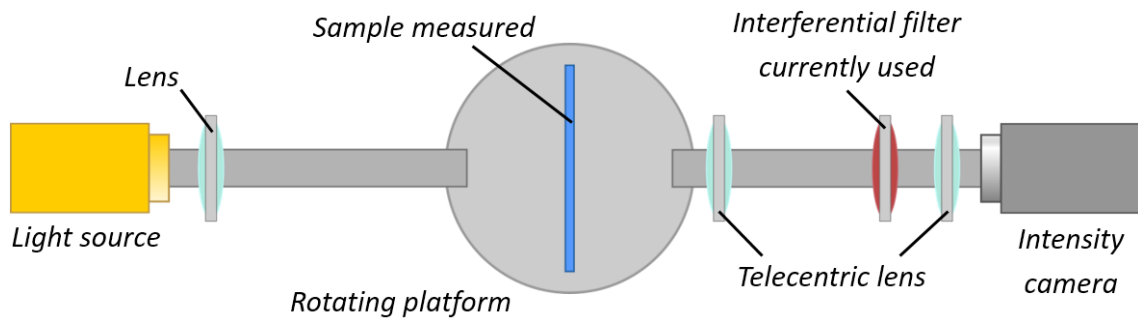


Figure 5.3: Scheme of the hyperspectral imaging system for the measurement of samples in transmission mode

The white reference used to normalize the exposure time of the camera (different for each waveband) in this configuration was air, assumed to be a perfectly clear transmitter. For each waveband, the pixel-to-pixel ratio of the sample image to the reference image provides the transmittance factor of the sample:

$$T(x, y, \lambda) = \frac{L_{sample}(x, y, \lambda)}{L_{reference}(x, y, \lambda)} \quad (35)$$

where (x, y) denote the pixel position in the image, λ the waveband, L_{sample} the radiance measured by the camera issued from the sample and $L_{reference}$ the one issued from the reference sample (air).

Figure 5.4 shows an example of two pairs of images of a sample printed with the PICSLUP system, obtained in this configuration using the 460 nm and 600 nm filters, along with the images of the white reference obtained using the same filters, i.e., without any sample placed in the holder. Note that spatial variations of the illuminance, lenses

transmittances, vignetting and other aberrations introduced by the system, are systematically corrected as they should be the same in both the sample and reference images.

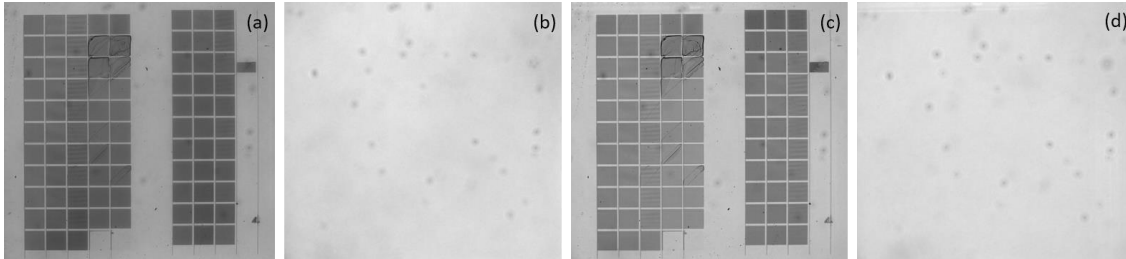


Figure 5.4: Images of a sample printed by the PICSLUP system (c,d) and images obtained with no sample placed in the holder (b,d), obtained with the intensity camera in transmission mode by using different filters: 460 nm (a,b), and 600 nm (c,d).

From the 31 pairs of images obtained by our system (similar to the ones shown above), we can reconstruct the hyperspectral image in transmission mode with a wavelength step of 10 nm, which is a rather good spectral and spatial resolution compared to hyperspectral imaging systems existing today.^{76,77}

5.4 Hyperspectral images in specular reflection

The geometrical configuration of the system for specular reflection measurements is illustrated in Figure 5.5. The illuminating and capturing arms are placed forming an angle α below 90° , depending on the wanted specular geometry. For our experiments, we used an angle of 30° . The sample measured is rotated such that the normal from its surface is the bisector of the two arms. This corresponds in our case to the $15^\circ:15^\circ$, or more generally $\alpha/2:\alpha/2$ bi-directional geometry. The light source is similar to the one used in transmittance mode.

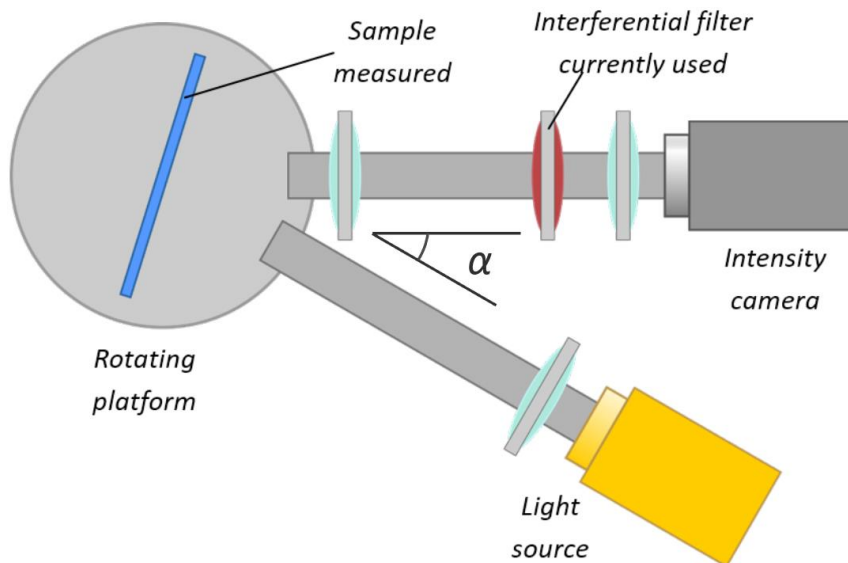


Figure 5.5: Scheme of the hyperspectral imaging system for the measurement of samples in specular reflection mode

The reference sample in this configuration should have similar reflectance as the printed glass plate that we want to measure in order to prevent saturation or under-illumination issues. We selected a polished silicon wafer.

For each waveband, the pixel-to-pixel ratio of the sample image to the silicon wafer image provides the reflectance factor of the sample in respect to the silicon wafer:

$$R_{\text{sample/silicon wafer}}(x, y, \lambda) = \frac{L_{\text{sample}}(x, y, \lambda)}{L_{\text{silicon wafer}}(x, y, \lambda)} \quad (36)$$

where (x, y) denote the pixel position in the image, λ the waveband, L_{sample} the radiance measured by the camera issued from the sample and $L_{\text{silicon wafer}}$ the one issued from the reference sample. In order to obtain the reflectance factor with respect to a perfectly achromatic reflector, we divide the reflectance factor given by Equation (36) with the reflectance of the silicon wafer, $R_{\text{silicon wafer}}$, measured with a spectrophotometer:

$$R(x, y, \lambda) = \frac{R_{\text{sample / silicon wafer}}(x, y, \lambda)}{R_{\text{silicon wafer}}(x, y, \lambda)} \quad (37)$$

Figure 5.6 shows an example of sample and reference images obtained in this configuration at 470 nm. As for the transmittance, spatial photometric heterogeneities of the optical bench (including the light source, the lenses, and the camera) are systematically compensated as they are similar in the sample and reference image. However, spatial heterogeneities of the reference sample may introduce errors in the computed reflectance factor, reason why a very flat, homogeneous and carefully cleaned silicon wafer was used.

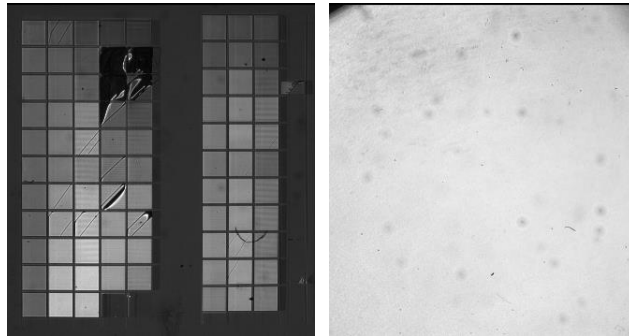


Figure 5.6: Image of a sample printed by the PICSLUP system (left) and of the white reference used (right), obtained in specular reflection mode by using the 470 nm filter.

5.5 Hyperspectral images in off-specular reflection

The geometrical configuration of the system for off-specular reflection measurements is illustrated in Figure 5.7. The illuminating and capturing arms form an angle β below 90° , namely 45° in our experiments. The sample is placed perpendicularly to the measuring direction.

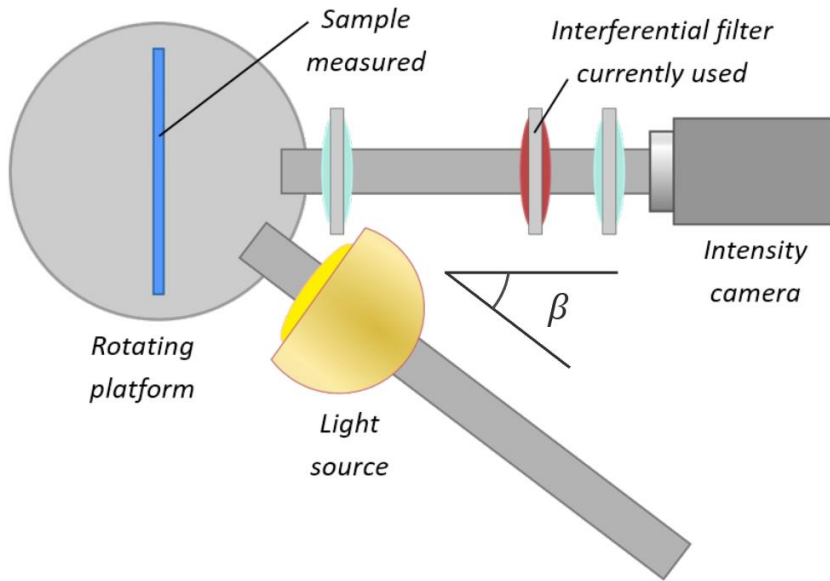


Figure 5.7: Scheme of the hyperspectral imaging system for the measurement of samples in off-specular reflection mode

Since the light reflected by highly specular samples in the off-specular direction is very low, a powerful light source was required in order for the camera to receive enough intensity. The light source used in this configuration was a tungsten lamp placed inside a 10-inch integrating sphere with a small output hole where the exitance of the light was concentrated. The illumination setup was placed on the illuminating arm in close proximity to the sample.

Once again, the reflectance of the reference sample should be similar to the one of the samples we want to measure. The particularity of our samples is to have a strong off-specular reflectivity in the medium wavelengths, while having a weak reflectivity in the rest of the spectrum, giving them a greenish appearance. With a white reflector as reference, one would obtain a saturation of the camera for the middle wavelengths, and a considerable amount of noise and quantization errors in the other wavelength ranges due to the low signal received. Figure 5.8 (left) shows a picture in off-specular reflection of a PICSLUP sample printed with many different laser parameter combinations. An illustration of a typical spectral reflectance of the samples in that configuration, and the reflectance of the white reference used is shown in Figure 5.8 (right).

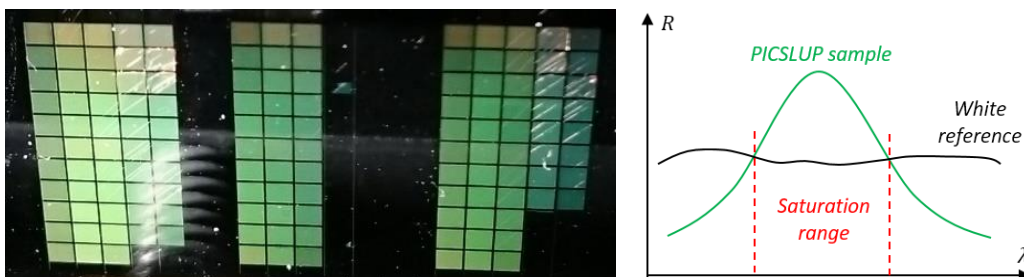


Figure 5.8: (Left) Image in off-specular reflection of sample printed with the PICSLUP system with many different laser parameter combinations. (Right) Illustration of a typical spectral reflectance of PICSLUP samples in off-specular reflection, and the reflectance of the white reference used.

In order to overcome these obstacles and thanks to the fact that the exposure time normalizations are done in a wavelength by wavelength basis, we selected a green diffusing sample (X-rite calibration tile for the Color i7® spectrophotometer) having a reflectance slightly higher than the PISCLUP samples in all the spectrum.

As for the specular reflection mode, the reflectance factor of the samples in off-specular mode is given by

$$R(x, y, \lambda) = \frac{L_{sample}(x, y, \lambda)}{L_{green\ tile}(x, y, \lambda) R_{green\ tile}(\lambda)} \quad (38)$$

where (x, y) denote the pixel position in the image, λ the waveband, L_{sample} the radiance measured by the camera issued from the sample, $L_{green\ tile}$ the one issued from the reference sample, and $R_{green\ tile}$ is the reflectance of the reference sample measured with a spectrophotometer

Figure 5.9 shows an example of images at 580 nm of a PISCLUP sample and the reference tile used.

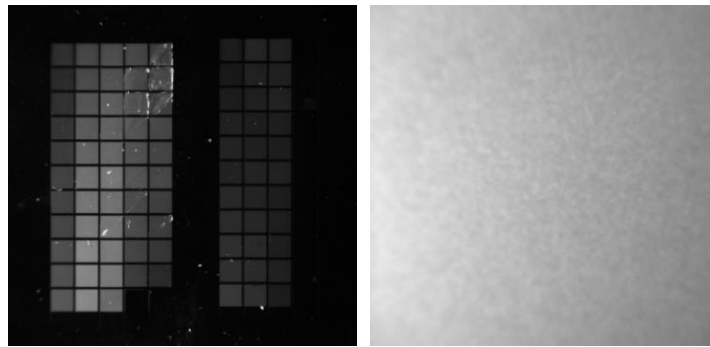


Figure 5.9: Image of a sample printed by the PISCLUP system (left) and of the white reference used (right), obtained in off-specular reflection mode by using the 580 nm filter.

5.6 Image registration of narrowband-filter images

An important requirement that has to be fulfilled in order to extract spectral information from images taken with different narrowband filters, is that they have been registered, i.e., that the elements in the images are located in the same absolute positions. Once the images have been aligned, the information from them can be extracted in a pixel-by-pixel manner. Even though the hyperspectral imaging system has been optically aligned, the narrowband filters introduce minor misalignments that can result in spatial differences in the images taken by the system. Figure 5.10, illustrates the spatial difference introduced by two different filters in images of the same sample taken under the same measurement mode. It is evident from this example that the position of a patch differs from one image to another one, and that identifying the patch position for deducing its spectrum requires the registration of the different images.

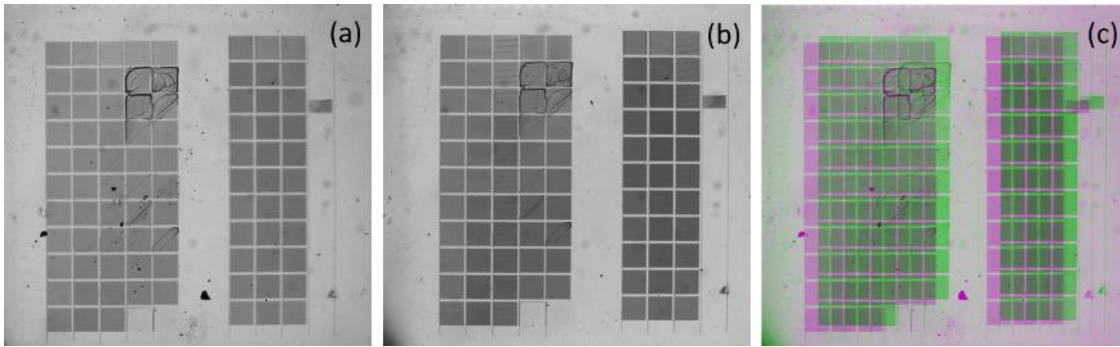


Figure 5.10: Images obtained by the hyperspectral system in transmission mode by using the 400 nm filter (a) and the 420 nm filter (b). Both images are combined in image (c) to highlight their misalignment.

Since the intensity of the printed areas in the images can vary widely according to the wavelength, due to the different colors displayed by the samples, the direct application of common image registrations algorithms did not always produce a correct alignment. In order to obtain a robust registration some pre-processing steps are required.

The images taken with each narrowband filter were aligned by using the following method, implemented with the MATLAB® software. The steps in the process are illustrated in Figure 5.11:

- 1) Define ***Im*** as the edges of the current image ***Cur*** being registered. The edges are obtained using the Canny edge detection algorithm,⁷⁸ resulting in a binary image where the white pixels are the edges detected (see row (b) in the figure).
- 2) Apply a morphological dilation⁷⁹ using a 2x2 kernel to ***Im*** in order to connect the edges that were not completely detected.
- 3) All holes in ***Im*** are filled, where the holes are black regions that are not connected to the edge of the image. This step allows us to have a binary approximation of the areas printed (see row(c) in the figure).
- 4) Remove noise in ***Im*** by removing all the white connected components with a pixel size smaller than a defined threshold (see row(d) in the figure).
- 5) Define ***Ref*** as the edges detected from the first image of the set of images being registered, which will be used as the reference for the registration.
- 6) Apply the same process used in steps 2, 3 and 4, to ***Ref*** in order to obtain a similar binary image with the main areas highlighted.
- 7) Obtain the transformation ***tform*** that aligns ***Im*** to ***Ref***, by performing an intensity-based registration with the *imregister* MATLAB® function (see row(e) in the figure).
- 8) Apply the geometric transformation ***tform*** to ***Cur*** and to the image of the white reference obtained with the same measurement mode and narrowband filter (see row (f) in the figure).

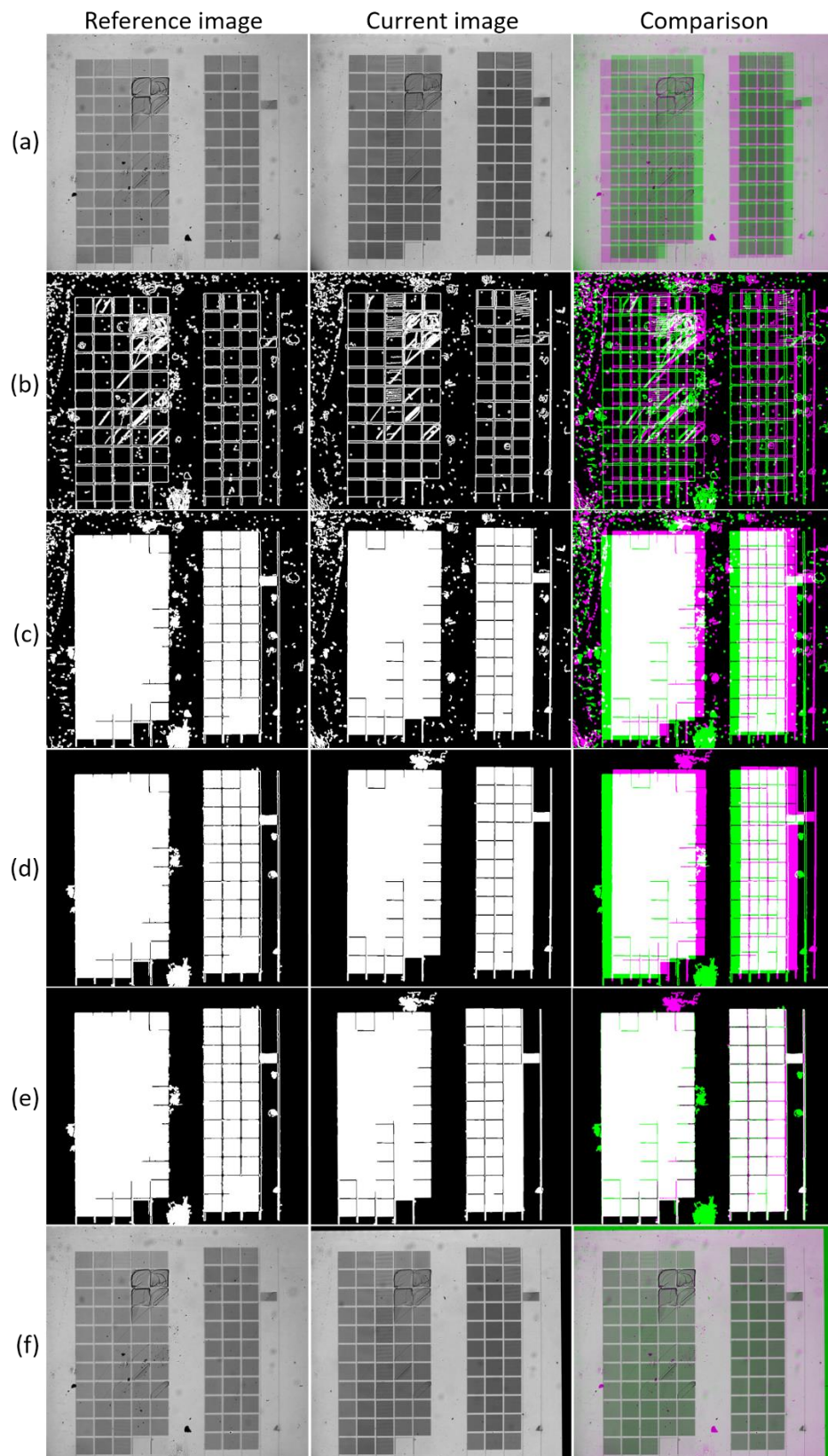


Figure 5.11: Example of images aligned by using our image registration method. The images on the left correspond to the reference used for the registration, the ones on the center correspond to the current image being registered, and the ones on the right to the comparison of both images in each stage of the process. (a) Original images used as input. (b) Edge detection and dilation. (c) Holes in images are filled. (d) Remove small objects. (e) Obtain and apply the image registration transformation. (f) Final registered image.

5.7 Color visualization of hyperspectral images

After the images have been registered and aligned, we have the spectral and spatial information of the observed samples. A good way to visualize the colors of the spectral images in a computer display is to render them by assuming an illuminant to obtain their CIE-XYZ values and then obtain their sRGB color by using standard transformations (see Section 2.10). In Figure 5.12 we can see some examples of images obtained with the hyperspectral imaging system of two different PICS LUP samples in the transmission, specular reflection, and off-specular reflection measurement geometries by assuming a D65 illuminant. We can notice the dramatic change in color of the same printed areas according to the observation/illumination geometry used.

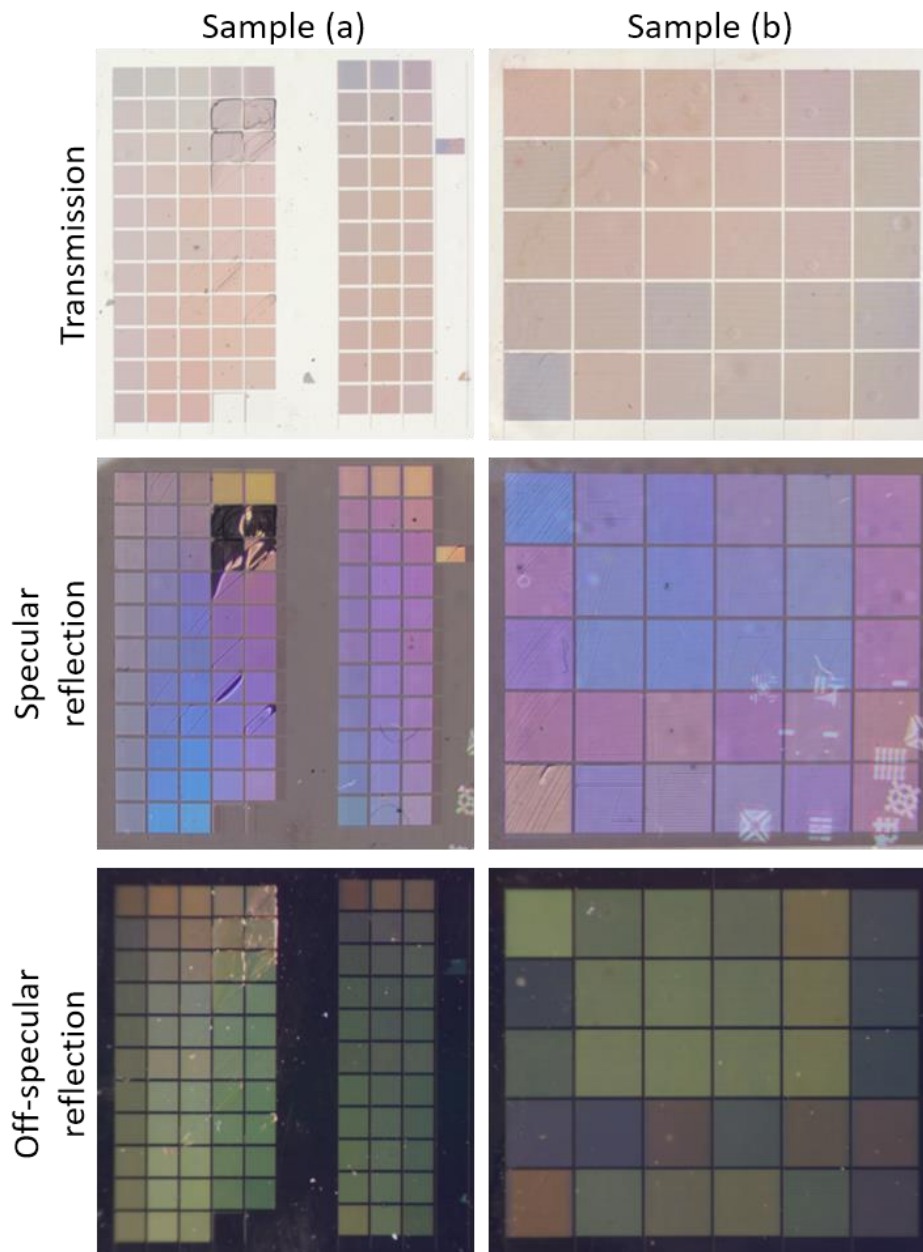


Figure 5.12: sRGB color images rendered from the hyperspectral images obtained from two different samples (a, b) in three different measurement geometries. The white defects in the specular reflection images are discussed in Section 5.8. The areas of the squares are: $1\text{ mm} \times 1\text{ mm}$ in sample (a), and $2 \times 2\text{ mm}$ in sample (b).

5.8 Extraction of spectral information from printed areas

In order to extract the spectral information from the samples we can simply calculate the average of the values of all the pixels in the printed areas concerned. However, we can obtain more accurate results by removing defects from the samples that were introduced by dust, printing errors, scratches or other unavoidable anomalies, such as the white marks shown in the specular reflection images of Figure 5.12. These white marks are due to the limited homogeneous area of the material used as a white reference for the specular reflection measurements, which contained printed patterns from previous unrelated experiments (see Figure 5.13).

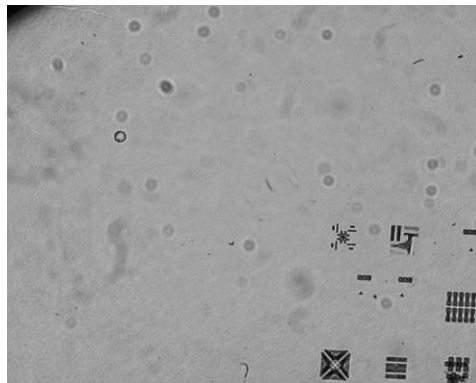


Figure 5.13: Image of the white reference used for the specular reflection measurements. The printed markings (from previous unrelated experiments due to unavailability of a new white reference with similar reflective properties) can influence some images obtained with the system, but their effect is excluded for spectral measurements.

The area selection for spectral extraction can be done either by selecting several rectangular areas manually, or semi-automatically, by specifying the dimensions of a grid of rectangles to be extracted and providing the pixel position of the top left corner of the grid. After the areas have been selected, they are enumerated and an image is generated as shown in Figure 5.14, to be used as a visual reference of the results obtained.

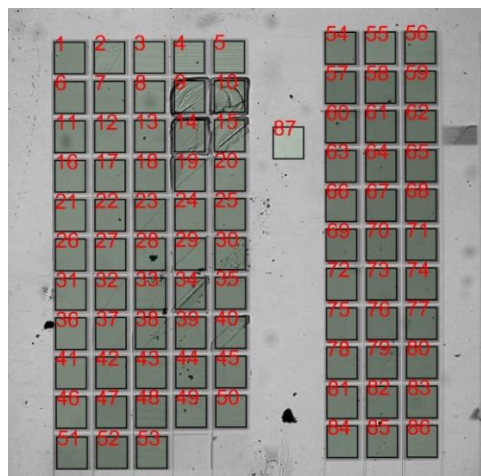


Figure 5.14: Areas enumerated prior to the spectral information extraction.

Each of these areas in the sample are treated individually along with the area in the same position of the image of the white reference obtained with the same narrowband filter, and their defects, such as the ones shown in Figure 5.15, are detected separately for the area of the sample and for the same area in the white reference.

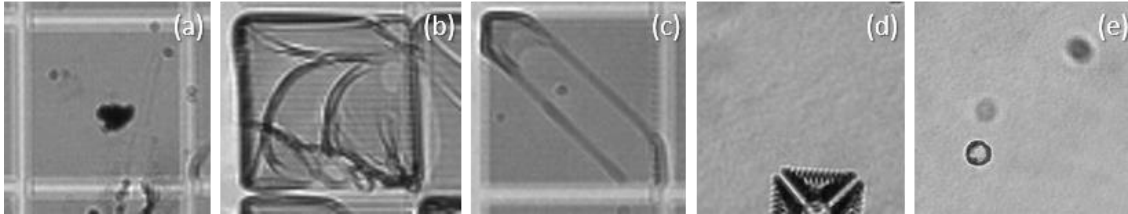


Figure 5.15: Defects present in areas of the printed samples (a, b, c) or in the same areas of the white reference used (d, e).

In order to detect the defects in the given areas, we calculated a reference central value C , which can be either: the mean, the median or the maximum-frequency bin of the histogram of the image. We also calculated the standard deviation σ of the values in the selected area. Based on these values we defined an acceptance range A given by the following equation:

$$A = C \pm k * \sigma \quad (39)$$

where k is a coefficient empirically chosen. All the pixels whose values were outside of this acceptance range were not considered for the calculation of the spectral information.

For our experiments, C was selected as the median of the values of the image, and a value of 2 was empirically defined for the coefficient k . In Figure 5.16 we can see the defect detection for a selected area with its rejected pixels highlighted.

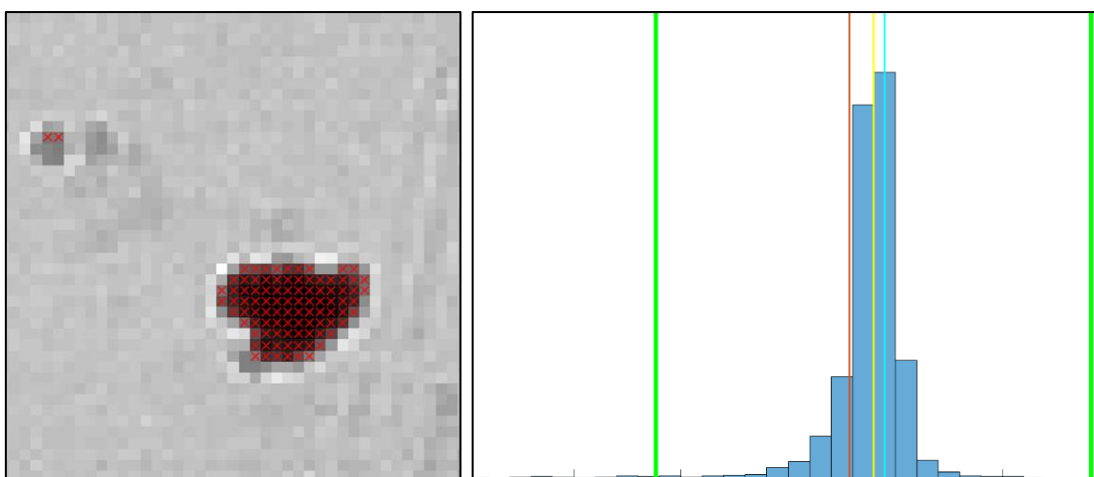


Figure 5.16: (Left) Selected image area with defects detected by our method. (Right) Histogram of the image analyzed with the following highlighted values: (yellow) median, (blue) maximum frequency histogram bin, (red) mean, and (green) limits of the acceptance range A .

The defect removal method also helps to remove the background of the samples in the case that the selection of the areas is not done very accurately, which can be seen in Figure 5.17.

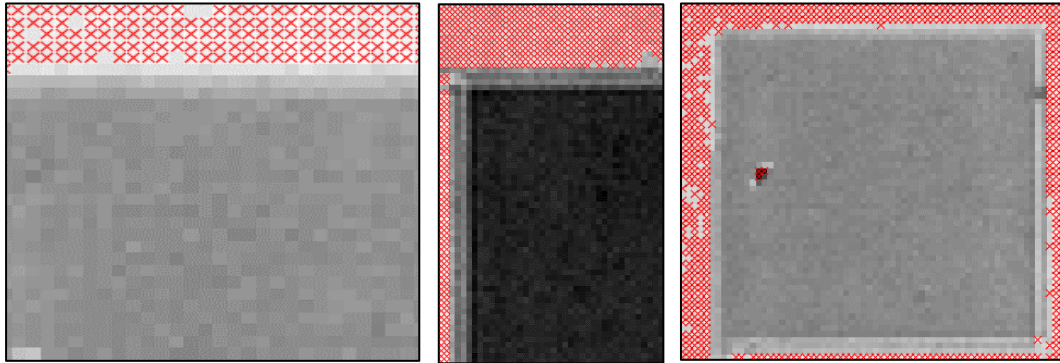


Figure 5.17: Rejection of background pixels by the defect removal algorithm due to their difference

All the non-rejected pixels by the defect detection algorithm were averaged and the spectral information was obtained from them according to the process define before for each of the measurement geometries.

5.9 Practical aspects of the hyperspectral imaging system

Although our system offers good spectral and spatial resolution compared to hyperspectral imaging systems existing today,^{76,77} the optical alignment process is very sensitive and can become a source of errors if not carefully performed. This is especially the case for measurements in specular reflection geometries since very small angular misalignments can dramatically change the amount of light that is reflected by samples with high specularity, which is the case for PICSLUP samples printed on glass.

The process to obtain the hyperspectral images is rather long in comparison to other industrially produced devices, since for each sample that needs to be measured, 62 images have to be captured, corresponding to 31 images of the white reference and 31 images of the sample measured, both captured with each of the narrowband filters. This part of the process can be improved if there are several samples to be measured, in which case the white reference measurements only need to be obtained once for the whole batch. Moreover, since our filter wheel consists of only 16 slots, it is necessary to capture the images with half of the filter set and then replace the filters in the wheel with the other half, which can be time consuming especially if several samples need to be measured. In that case, the process can be optimized by first obtaining all the images of the first half of the filters for all the samples in the batch, replace the filters, and then capture the images with the second half of the filters. Finally, the images obtained have to be registered, which can take approximately 10 minutes for the whole set of images of one sample.

5.10 Conclusion

The hyperspectral imaging system described in this chapter allows to capture spectral images with good spectral and spatial resolution. The system can be adjusted to variable illumination/observation angles in transmission, specular reflection, and off-specular reflection configurations, and can automatically remove the influence of defects or printing errors when used to extract the spectral information of predefined areas. The range of colors measured with this system, from samples produced with the PICSLUP technology, will be presented in the next chapter in the context of color gamut and the evaluation of halftoning techniques.

6

COLOR GAMUT AND EXTENSION BY HALFTONING

The International Commission on Illumination (CIE) defines *color gamut* in their Colorimetry technical report³⁶ as:

“A range of colors achievable on a given color reproduction medium (or present in an image on that medium) under a given set of viewing conditions – it is a volume in color space.”

When referring to the achievable colors, this range is normally represented by a volume in a color space which contains all the color coordinates that can be produced by a system.

In Chapter 4 we showed all the primary colors measured in the 0°:0° specular reflection geometry thanks to the microscope imaging system, from samples produced by varying many printing parameters of the PICSLUP system. Thanks to the hyperspectral system described in Chapter 5, a representative subset of these samples was produced and measured in other geometrical configurations, in both recto and verso faces of the samples: 0°:0° transmission, 15°:15° specular reflection, and 45°:0° off-specular reflection.

In this chapter, we will first show the color gamuts that can be achieved by the PICSLUP printing system in the different measuring geometries, then we will analyze the possibility of extending them by juxtaposing patterns of different colors with halftoning techniques.

6.1 PICSLUP color gamut estimation

The resolution of the hyperspectral bench is good, but not as high as the one of the microscope. The measurement of single-line color patches is therefore not possible, and

larger color patches made of numerous printed lines are needed. A microscope image of one of the large patches printed is shown in Figure 6.1.

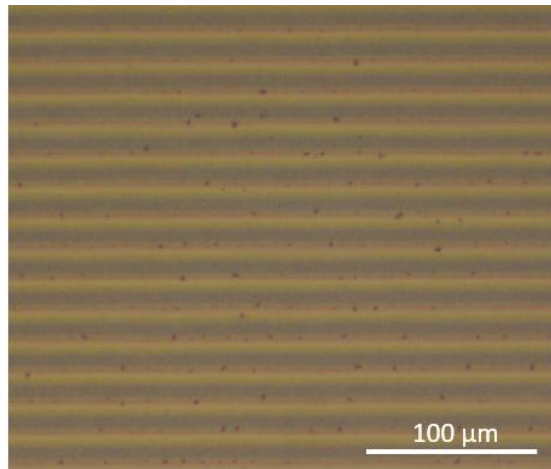


Figure 6.1: Microscope image of one of the large patches made by printing numerous consecutive lines.

In order to limit the printing time, the number of glass supports (whose preparation may induce slight variations) and also the measurement effort, we made a selection of color patches instead of the exhaustive color chart measured by microscope (see Chapter 4) obtained by incrementing each of the command parameters of the printing system. A total of 330 samples were printed in squares with an area of 1×1 mm, with the following combinations of parameters:

- 2 wavelengths (nm): 488 and 647
- 3 powers (mW): 300, 400, and 600
- 11 translation speeds ($\mu\text{m/s}$): 30000, 3200, 2000, 1400, 1200, 1000, 900, 800, 600, 500, and 300
- 5 focus distances (mm): 0, 0.5, 0.8, 1.8, and 2

The squares were separated in groups of equal wavelengths and powers containing 11 rows (corresponding to the speeds) and 5 columns (corresponding to the focus distances) as illustrated in Figure 6.2. It can be noted that many squares especially in the longer focusing distances were not printed by the system due to printing issues. The spectra and colors reported in this section are only the ones measured from the squares that were successfully printed.

The spectra of all the printed squares in both front and back sides of the samples (also called recto and verso) were calculated with our hyperspectral imaging system and their CIELAB colors were obtained by assuming a D65 illuminant in order to visualize the volume of colors that can be produced with the PICSLUP system.

The colors obtained from the hyperspectral measurements are shown from Figure 6.3 to Figure 6.8. Their background was calculated using a D65 illuminant, for each (a^* , b^*) coordinate by assuming a lightness value of L^* equal to 50 and converting the resulting (L^* , a^* , b^*) tristimuli to the sRGB space.

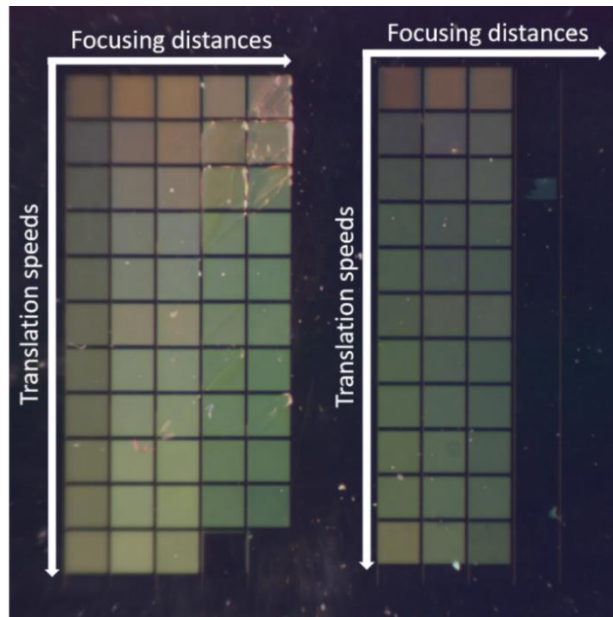


Figure 6.2: Image in off-specular reflection of areas printed with a laser wavelength of 488 nm, and laser powers of 300 mW (left group) and 400 mW (right group)

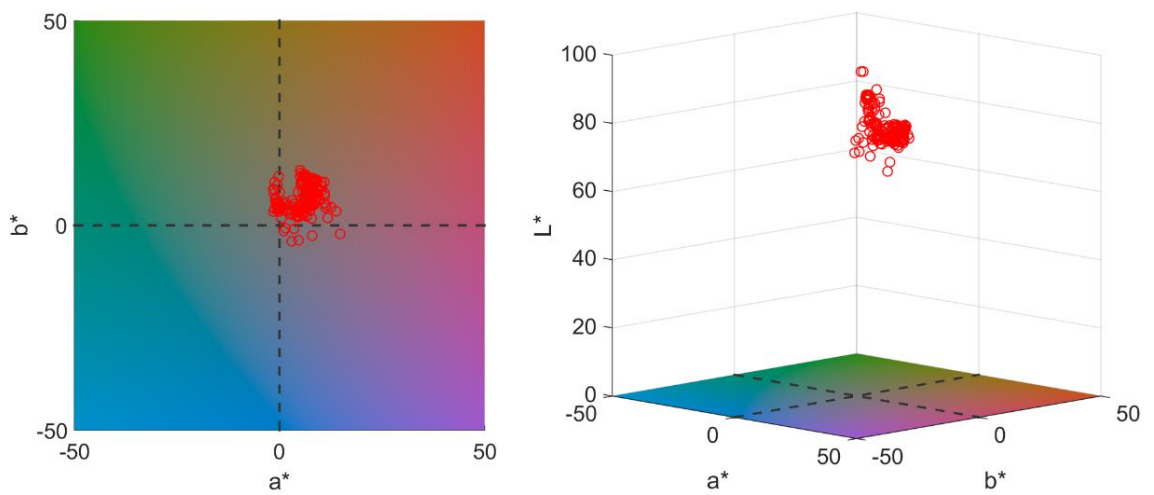


Figure 6.3: Colors obtained in transmission mode of the front side of the samples

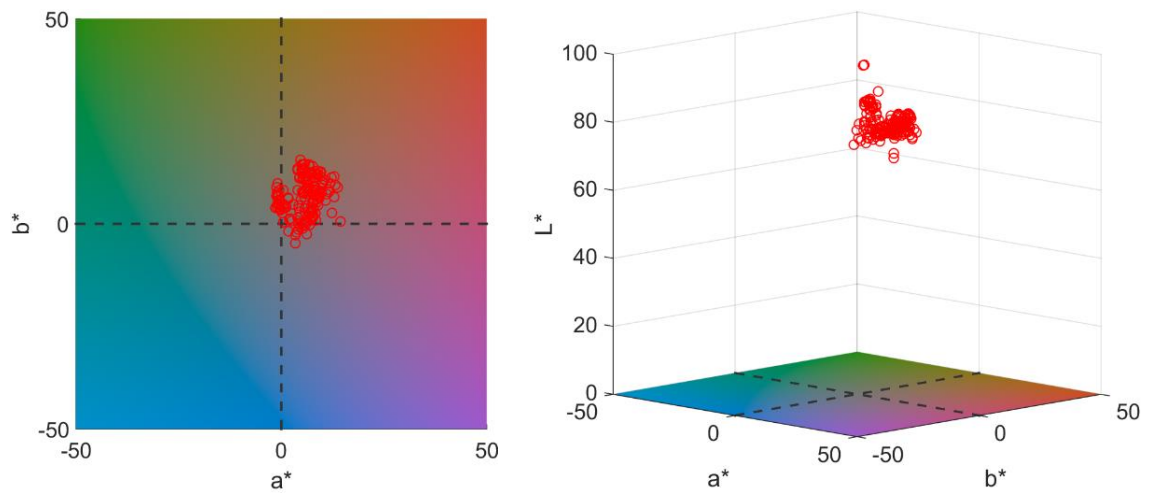


Figure 6.4: Colors obtained in transmission mode of the back side of the samples

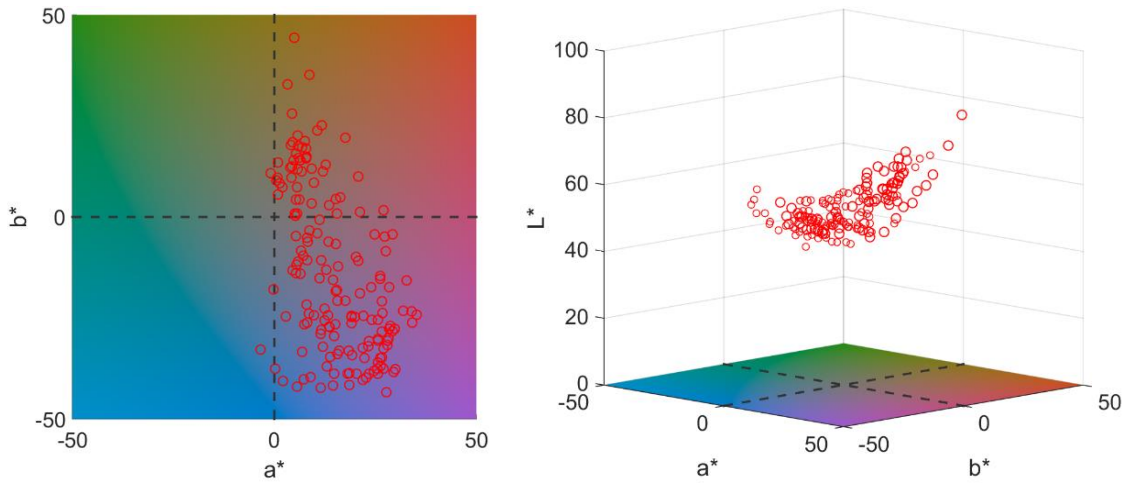


Figure 6.5: Colors obtained in the $15^\circ:15^\circ$ specular reflection mode of the front side of the samples

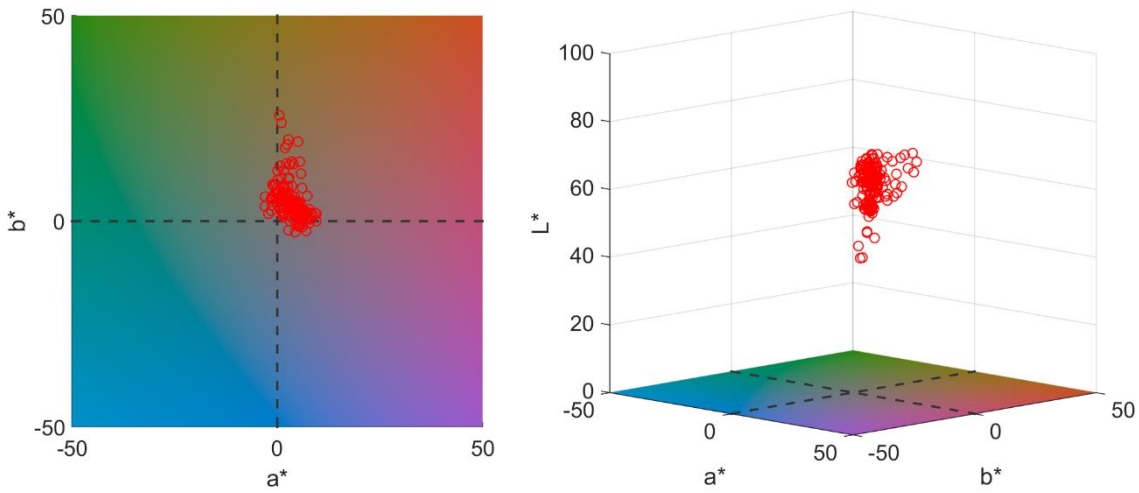


Figure 6.6: Colors obtained in the $15^\circ:15^\circ$ specular reflection mode of the back side of the samples

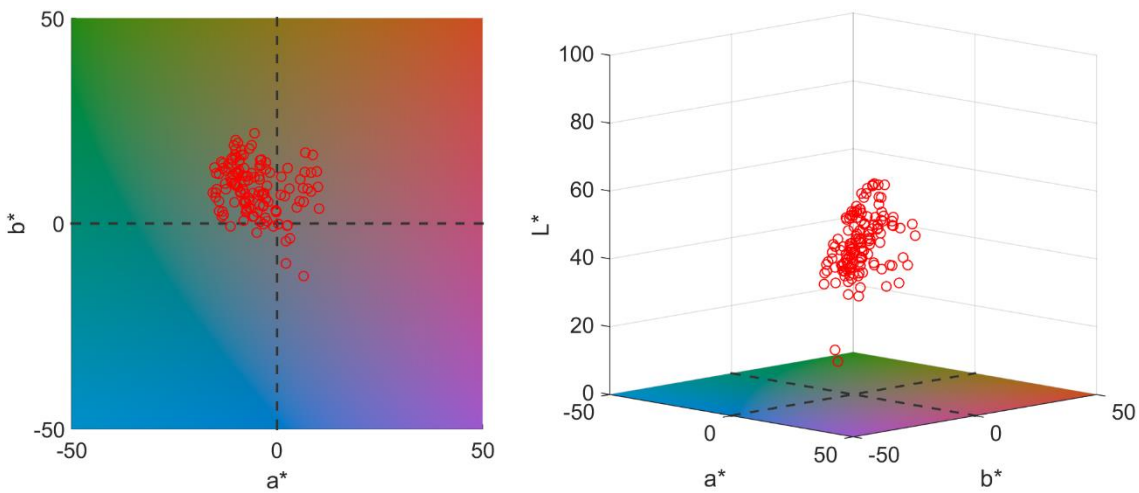


Figure 6.7: Colors obtained in the $45^\circ:0^\circ$ off-specular reflection mode of the front side of the samples

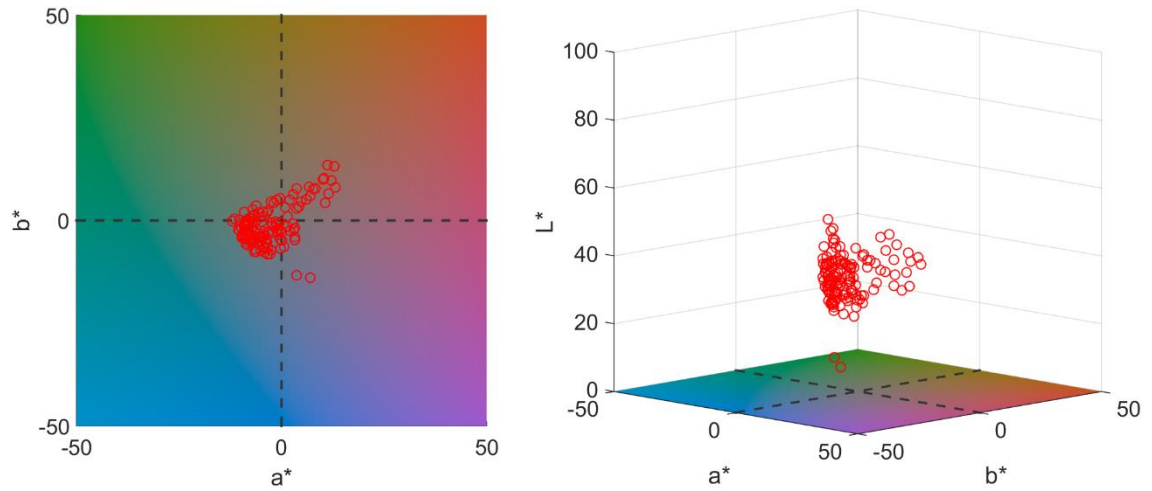


Figure 6.8: Colors obtained in the 45°:0° off-specular reflection mode of the back side of the samples

From these results we can observe that a wide range of different colors can be obtained by varying the printing parameters of the PICSLUP system. These colors also change dramatically depending on the illumination/observation geometrical configurations.

Transmission mode (Figure 6.3 and Figure 6.4): The color gamut obtained in this configuration is very reduced, consisting mainly of very light and pale colors of orange hue. There were no significant variations between the colors obtained in front and back sides.

Specular reflection mode (Figure 6.5 and Figure 6.6): From all the configurations tested, the front-side specular-reflection mode produces the widest range of chromaticities in the samples. However, the variation in lightness in that geometry is rather limited, presenting L^* values of between 40 and 65 units. The colors in the back side of the samples in this configuration have a much smaller volume, with very reduced chromatic and lightness variations.

Off-specular reflection mode (Figure 6.7 and Figure 6.8): The volume of colors that can be obtained in both front and back sides of this configuration have a moderate size, with a strong presence in the green hue in the front side, and cyan hue in the back side, which are lacking in the other configurations.

Other sets of samples designed with different halftoning patterns were also printed using the PICSLUP system and characterized thanks to the hyperspectral imaging system. These samples and their characteristics will be discussed in detail in Section 6.3.

6.2 Multiple colors displayed by a single patch

As it was previously mentioned, the colors produced by the PICSLUP system have a strong dependence on the illumination/observation geometry used, and a single printed patch can have widely different colors depending on the viewing conditions. In Figure 6.9 we show the colors displayed by six different printed patches in all the geometrical configurations tested. The colors were obtained by calculating their XYZ tristimulus

values from their spectral information using a D65 illuminant, and then transforming them to the sRGB color space by using standard transformations (see Section 2.10). As it can be seen in the image, several patches can display similar colors in one geometry, while also displaying completely different colors in another. An example of this color match/mismatch is seen in samples 3 and 6, whose colors match visually in the transmission configurations, while being completely different in the specular and off-specular reflection configurations, or in samples 1 and 3, whose color match visually in the off-specular reflection verso configuration while being different in every other configuration. This property gives a multi-dimensional characteristic to the primaries printed and opens the possibility for interesting security and design applications that will be discussed in Chapter 7.

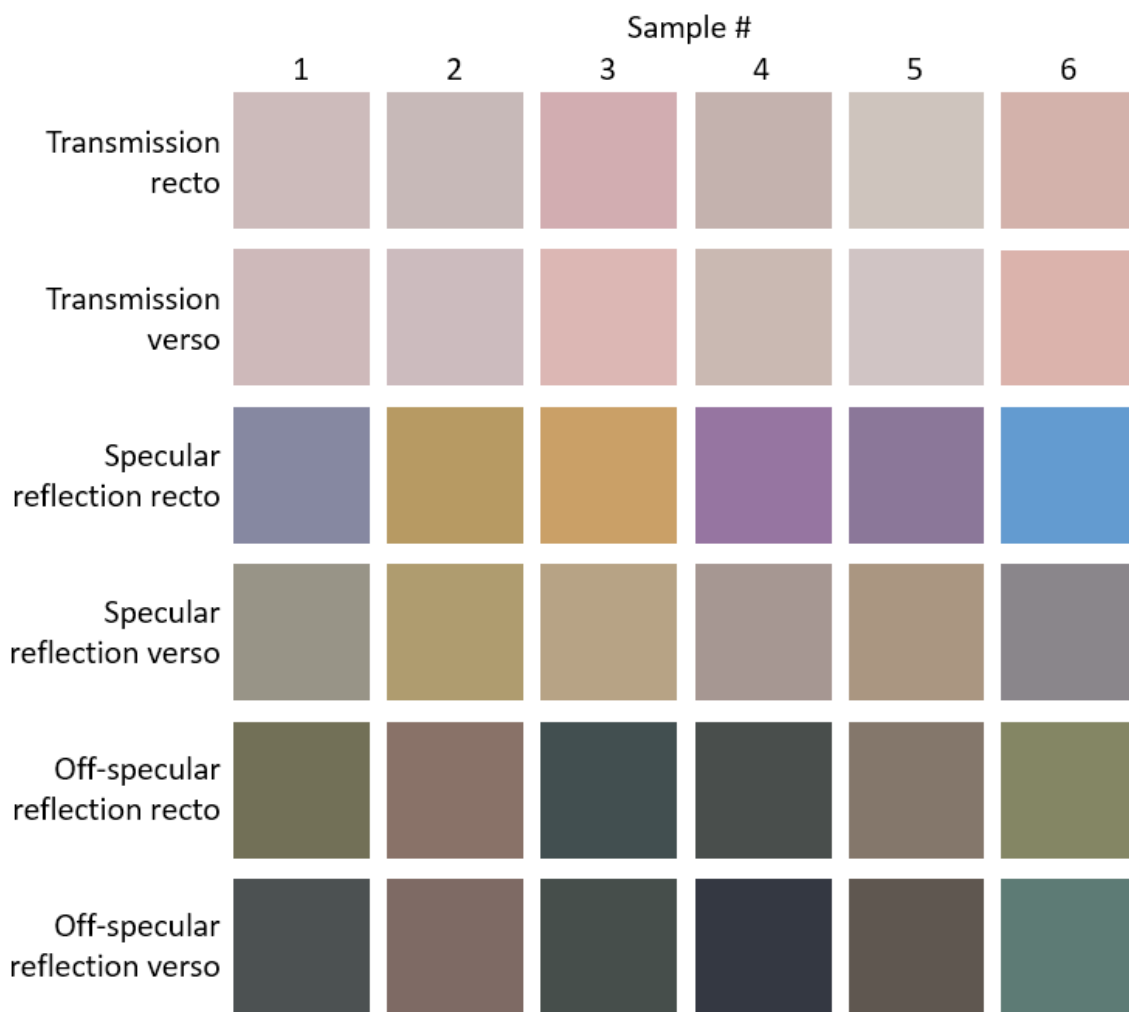


Figure 6.9: Colors displayed by six different printed patches in all the geometrical configurations tested. The colors were obtained from hyperspectral measurements assuming a D65 illuminant.

6.3 Halftoning

Halftoning is an ancient technique used by engravers to produce the impression of grey level images from a binary printing process, by juxtaposing small areas with and without ink at a higher frequency than the human visual system's modulation transfer function. Multi-color halftoning is based on the same principle by printing several halftone images with different color inks, typically cyan, magenta, yellow and black. Since the PICS LUP technology is a continuous-tone printing system able to reproduce several primary colors in each pixel of the printed image, halftoning is not strictly required. However, as its color gamut is sparse in some regions and concave (see Figure 4.11), there is an interest in seeing whether halftoning could increase the size of the color gamut and make it more convex, dense and continuous. Halftoning is also a way of creating, not only more colors in each of the geometrical configurations studied, but also more primaries with different sets of colors in multiple configurations, as discussed in Section 6.2. The most suitable type of halftoning with the PICS LUP technology is the line halftoning, a variant of the dot-off-dot halftoning,⁸⁰ where lines of different primary colors are periodically juxtaposed without overlapping.

In order to evaluate the color prediction of halftoning patterns printed with the PICS LUP system, first experiments were carried out on two-color halftone patches where lines of two colors are alternated, covering each one 50% of the surface. Through these experiments, we wanted to verify that the spectral reflectance or transmittance of the halftone patches could be predicted from the ones of the full-tone patches. For that purpose, we used the Yule-Nielsen modified Spectral Neugebauer (YNSN) model in reflectance mode,^{81,82} or accordingly in transmittance mode.⁸³

Let us consider the reflectance mode corresponding to a given measuring geometry, and denote as $R_1(\lambda)$ and $R_2(\lambda)$ the spectral reflectance factors (or similarly, transmittance factors) of two primary colors at a given wavelength λ . In absence of scattering by the printing support, each point of the printed surface should reflect and transmit light independently of each other. The spectral Neugebauer model⁸⁴ thus applies, which predicts spectral reflectance of the halftone as the sum of the one of the primaries weighted by their respective surface coverage a_i :

$$R(\lambda) = a_1 R_1(\lambda) + a_2 R_2(\lambda) \quad (40)$$

where the sum of the surface coverages a_i is 1. Note that the unprinted support, which is present in the halftone, is a primary. When the halftone contains $N > 2$ primaries, its reflectance is given by:

$$R(\lambda) = \sum_{i=1}^N a_i R_i(\lambda) \quad (41)$$

If slight scattering occurs within the support, due in particular to small defects, surface roughness and multiple reflections of light between the different interfaces, it is possible that light crosses different areas along its path interacting with different primaries. This phenomenon, called optical dot gain,⁸⁴ is strong in paper prints where the

printing support is strongly scattering, but also noticeable with inkjet prints on transparency films.⁸⁵ For most kinds of halftone prints, optical dot gain is the cause of poor prediction accuracy by the Neugebauer model, but a simple correction, known as the Yule-Nielsen transform,⁸¹ allows a considerable gain in prediction accuracy:

$$R(\lambda) = \left[(1-a)R_1^{1/n}(\lambda) + aR_2^{1/n}(\lambda) \right]^n \quad (42)$$

or, in case of N primaries,

$$R(\lambda) = \left[\sum_{i=1}^N a_i R_i^{1/n}(\lambda) \right]^n \quad (43)$$

where the sum of the surface coverages a_i is equal to 1, and n is an empirical parameter, having generally a real value higher than 1, modeling partial mixing between the fluxes interacting with each primary. The n value generally depends on the measuring geometry,⁸³ especially with a clear printing support in which the optical dot gain due to the multiple reflections between the two interfaces of the glass plate may have different importance in reflection and transmission modes. The Neugebauer model is a special case where $n = 1$.

6.4 First experiments with halftone samples

In order to check the validity of the prediction model, a very first experiment was carried out (a more comprehensive one is presented in the next section), consisting of halftone samples composed of two primaries: one line over two was printed with a first primary, the second primary being the remaining unprinted support. Spectral measurements were done at the macroscopic scale by using a goniospectrophotometer allowing the following configurations:

- Specular reflectance mode with a 20°:20° geometry;
- Transmittance mode with a 0°:0° geometry

The Color i7 spectrophotometer was also used for the following configuration:

- Off-specular reflectance mode with a de:8° geometry

These first experiments were performed before the ones presented in Chapter 5 and Section 6.5, for which we decided to use a smaller aspecular angle (15°:15°) in order to have a more similar configuration to the one used with the microscope camera.

In the three measurement configurations, the white references from which the reflectance/transmittance factors were defined were achromatic surfaces reflecting a comparable radiance to the samples. The $R_1(\lambda)$ and $R_2(\lambda)$ reflectance/transmittance factors were obtained from spectral measurements of areas fully covered with the respective primaries.

By way of illustration, we reproduce in Figure 6.10 the measured and predicted spectra for one 50% halftone in the three modes: specular reflectance, off-specular reflectance and transmittance. The CIE94 color-difference values computed between the predicted and measured spectra in these three modes, indicated in the figure, are rather good. To obtain the predictions for a given measurement geometry and material type, the values of a and n are fitted to minimize the calculated color difference between the measured and predicted spectra.

The surprising results come from the very high value of surface coverage a fitted in off-specular reflectance mode, which indicates that this value might incorporate optical phenomena not taken into account in the Yule-Nielsen model, especially slight scattering by the engraved areas whose impact in comparison to the low reflected radiance may be significant. Similar differences in the fitted surface coverage values according to the measuring mode were already noticed with transparencies printed by inkjet, but this did not prevent good reflectance and transmittance predictions.⁸⁵

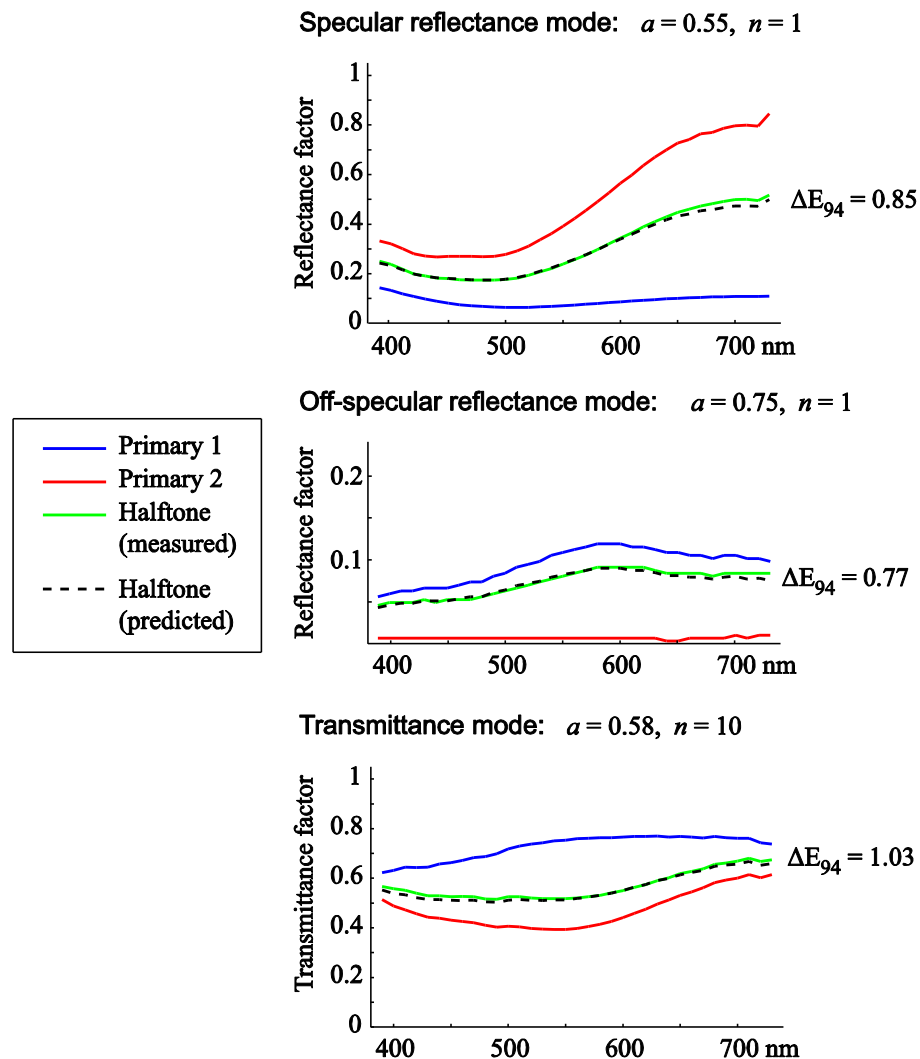


Figure 6.10: Measured spectral reflectance factor (specular and off-specular modes) and transmittance factor of fulltone primaries printed with PICSUP and a halftone made with these primaries, and spectrum of the halftone patch predicted with the Yule-Nielsen modified Spectral Neugebauer model with the fitted parameters a and n values indicated above the plots.

From the measured and predicted spectra, colors were computed in the CIELAB color space by assuming a D65 illuminant. By varying the surface coverage a of the second primary in the Yule-Nielsen modified Spectral Neugebauer equation, we can predict the set of colors achievable with a pair of primaries. The ones achievable with the primaries used for the sample presented in Figure 6.10 are displayed in Figure 6.11 in 2D and 3D views of the CIELAB color space. As we can see, the set of colors obtainable by halftoning with two primaries draws an almost straight line. Hence, we might expect that the color gamut displayed in Figure 6.5 for the specular reflection mode could become convex, and more suitable for gamut mapping. This will be further evaluated with a more comprehensive set of appropriate halftone color patches in the following sections.

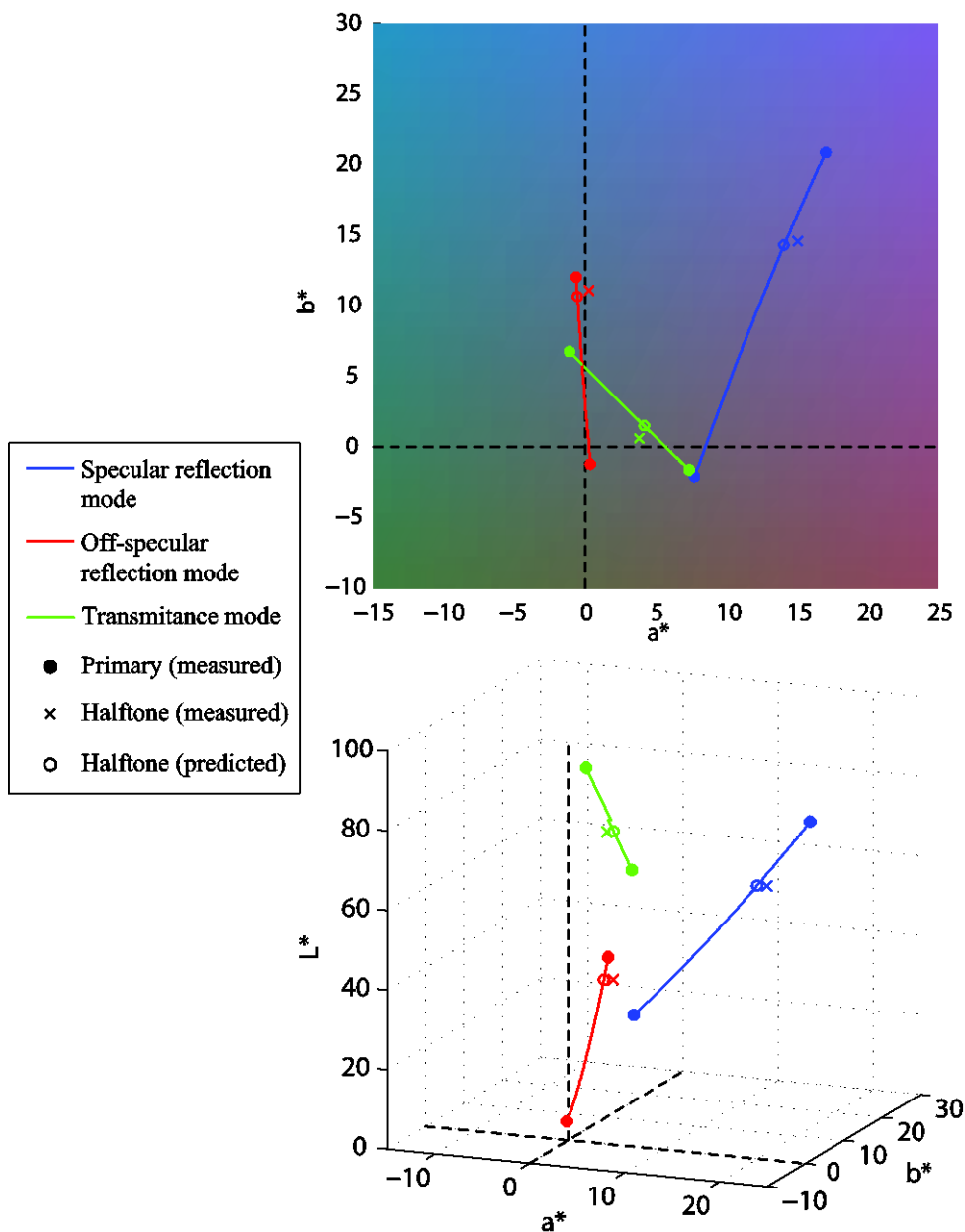


Figure 6.11: 2D and 3D representations of the measured colors in the specular and off-specular reflection modes and the transmittance mode of fulltone primaries printed with PICSLUP and a halftone made with these primaries. The reference colors in the background of the 2D view were calculated by fixing a lightness value L^* of 50 units.

6.5 Advanced experiments with halftone samples

In order to further validate the color prediction accuracy of the model for samples produced using halftoning, we designed a more comprehensive set of samples made of different primaries and with different surface coverages.

6.5.1 Selection of halftoning primaries

Five different halftoning primaries were selected due to their well-distributed locations in the CIELAB color space when measured in specular reflection mode. Their printing parameters and CIELAB coordinates in the specular reflection mode are presented in Table 7.

Table 7: Printing parameters and CIELAB coordinates of the printing primaries used for the extended evaluation of halftoning predictions. The CIELAB values were measured with the hyperspectral imaging system in the specular reflection mode.

Primary name	Laser wavelength	Laser power	Translation speed	Focusing distance	L*	a*	b*
1	488 nm	600 mW	500 $\mu\text{m/s}$	0.8 mm	56.74	9.07	-35.34
2	488 nm	300 mW	1400 $\mu\text{m/s}$	0.8 mm	56.65	24.07	-21.37
3	488 nm	400 mW	1000 $\mu\text{m/s}$	0.8 mm	54.99	23.36	-32.16
4	488 nm	300 mW	3200 $\mu\text{m/s}$	0.8 mm	55.54	24.31	-15.37
5	488 nm	400 mW	3000 $\mu\text{m/s}$	0.8 mm	61.93	12.65	1.91

Figure 6.12 shows color calibrated images of areas consisting of lines printed with the primaries selected, captured with our microscope imaging system.

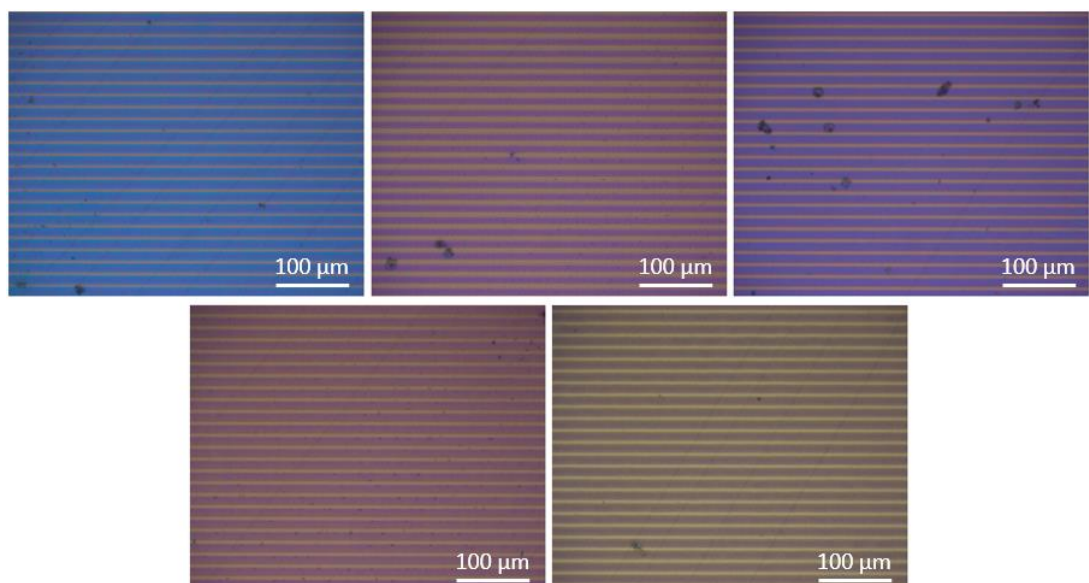


Figure 6.12: Microscopic images of areas printed using the parameters selected for the halftoning primaries. The primaries are presented in the same order as in Table 7.

6.5.2 Halftone samples

A set of 30 different squares, each with an area of 2×2 mm composed of lines of $20 \mu\text{m}$ width, were printed on the same glass support with different combinations of the primaries selected and different proportions of area coverage. An image of the squares, captured with the hyperspectral imaging system in the $15^\circ:15^\circ$ specular reflection configuration, is shown in Figure 6.13.

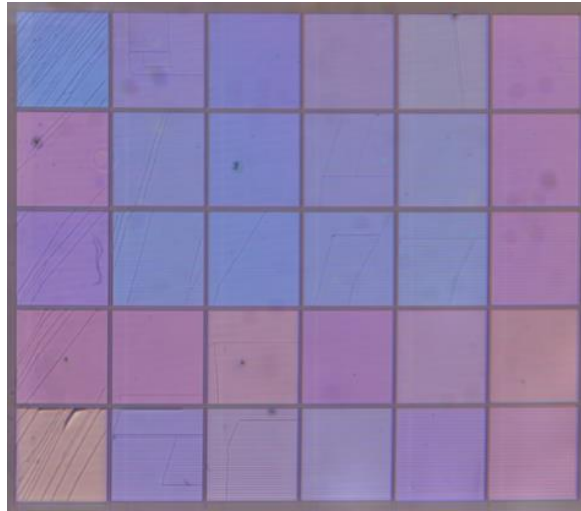


Figure 6.13: Image of the squares printed for halftoning prediction testing, captured with the hyperspectral imaging system described in Chapter 5.

Full Primary 1	(1,2) 1:1	(1,3) 1:1	(1,4) 1:1	(1,5) 1:1	(2,3) 1:1
Full Primary 2	(1,2) 2:1	(1,3) 2:1	(1,4) 2:1	(1,5) 2:1	(2,3) 2:1
Full Primary 3	(1,2) 3:1	(1,3) 3:1	(1,4) 3:1	(1,5) 3:1	(2,3) 3:1
Full Primary 4	(2,4) 1:1	(2,5) 1:1	(3,4) 1:1	(3,5) 1:1	(4,5) 1:1
Full Primary 5	(1,2,3) 1:1:1	(1,2,5) 1:1:1	(1,3,5) 1:1:1	(2,1,3) 2:1:1	(2,4,5) 2:1:1

Figure 6.14: Specification of squares printed for halftoning evaluation. The squares on the leftmost column were printed by using only one primary, while the other 25 were printed by combining the primaries in the parenthesis in the proportions shown.

The composition of each of the printed squares is specified in Figure 6.14. The leftmost column corresponds to areas printed by using only one of the primaries. These will be used as inputs in the prediction models in order to estimate the colors obtained from the combination of several primaries. The remaining 25 squares correspond to areas printed with the combinations of two or three different primaries. The primaries used are

specified by the numbers in the brackets, and the ratio of the area covered by each of them is specified below the primaries. For example, the square located in the 2nd row and 5th column is made with the primaries 1 and 5, with a ratio of 2 lines of Primary 1 for each line of Primary 5. In order to illustrate this example, a microscopic image of the sample is shown in Figure 6.15.

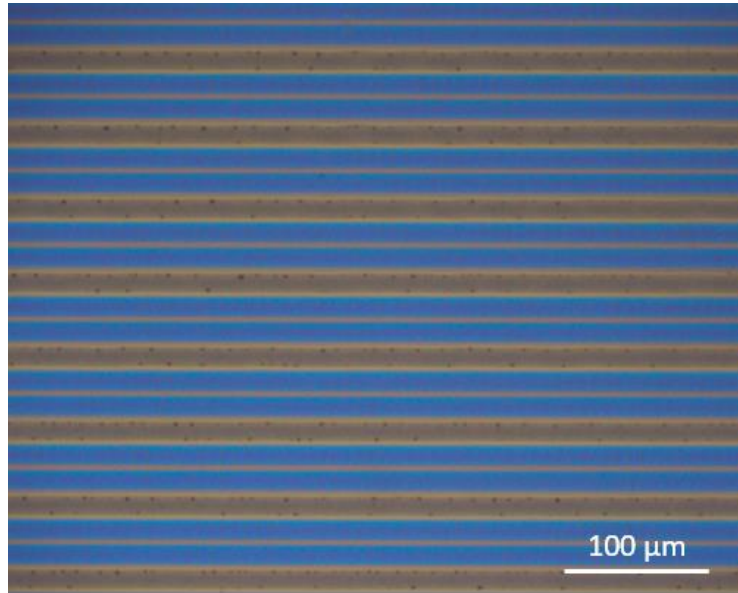


Figure 6.15: Microscopic image of a two-color halftone with a coverage of 2 lines of Primary 1 (blue) for each line of Primary 5 (yellow).

6.5.3 Measurement configurations and spectral predictions

The spectral properties of the samples were measured in the following geometrical configurations by using the hyperspectral imaging system described in Chapter 5:

- Transmission front side (recto) at 0°/0°
- Transmission back side (verso) at 0°/0°
- Specular reflection front side at 15°/15°
- Specular reflection back side at 15°/15°
- Off-specular reflection front side at 45°/0°
- Off-specular reflection back side at 45°/0°

Figure 6.16 shows the measured and predicted spectra of the first halftoning patch, located in the first row and second column of the sample, for each of the different measurement configurations by using a parametric value of $n = 1$. For this halftone area the prediction accuracy, assessed with the CIE94 color difference between the measured and predicted colors by assuming a D65 illuminant, is rather good, considering that the just-noticeable-difference threshold of the human visual system is approximately 1 CIE94 unit.

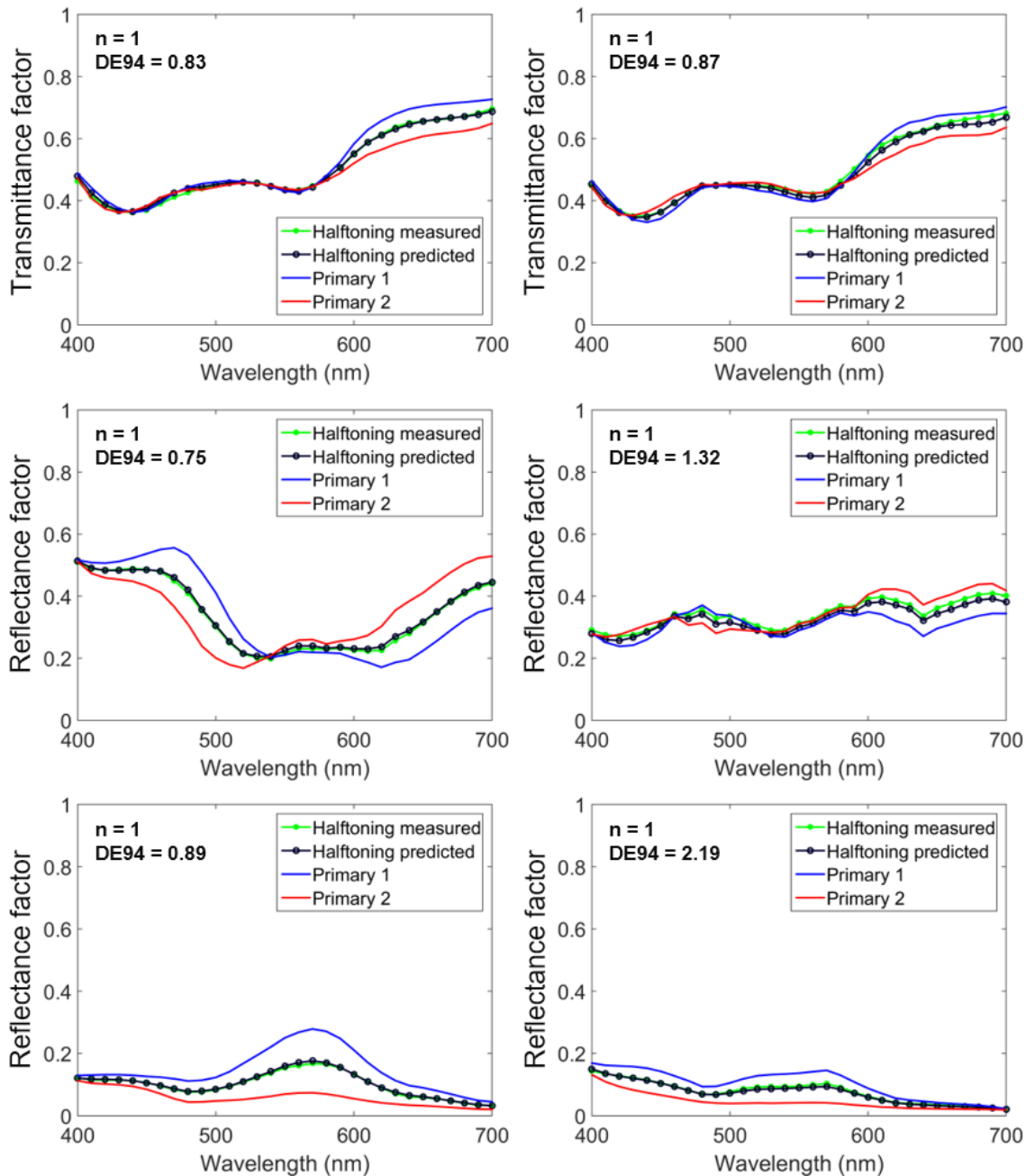


Figure 6.16: Measured and predicted spectra of the first halftoning square, located in the first row and second column of the sample, for the following configurations: (top row) transmission, (middle row) specular reflection, (bottom row) off-specular reflection. The left plots correspond to front side, while the right plots correspond to back side of the sample. The color differences between the measured and the predicted spectra, assuming a D65 illuminant, are displayed in the top-left corner of each plot.

The prediction accuracy for the Neugebauer model over the set of samples that we produced is shown in Figure 6.17. Similar to Figure 6.16, the quality of the prediction was assessed with the CIE94 color difference between the measured and predicted colors by assuming a D65 illuminant. The prediction accuracy is slightly poorer than the one usually achieved in color reproduction by digital printers (e.g. inkjet on photo-quality paper).⁸² However, the PICS LUP printing system is probably less reproducible than commercial digital printers because it is not yet a commercial printer but a laboratory

device in development. It also presents small artifacts which may have small but noticeable impact on the spectral properties of the prints. Moreover, the measurement process is also subject to some imprecision and noise. Being given these constraints, we can be satisfied with the prediction accuracy that is achieved.

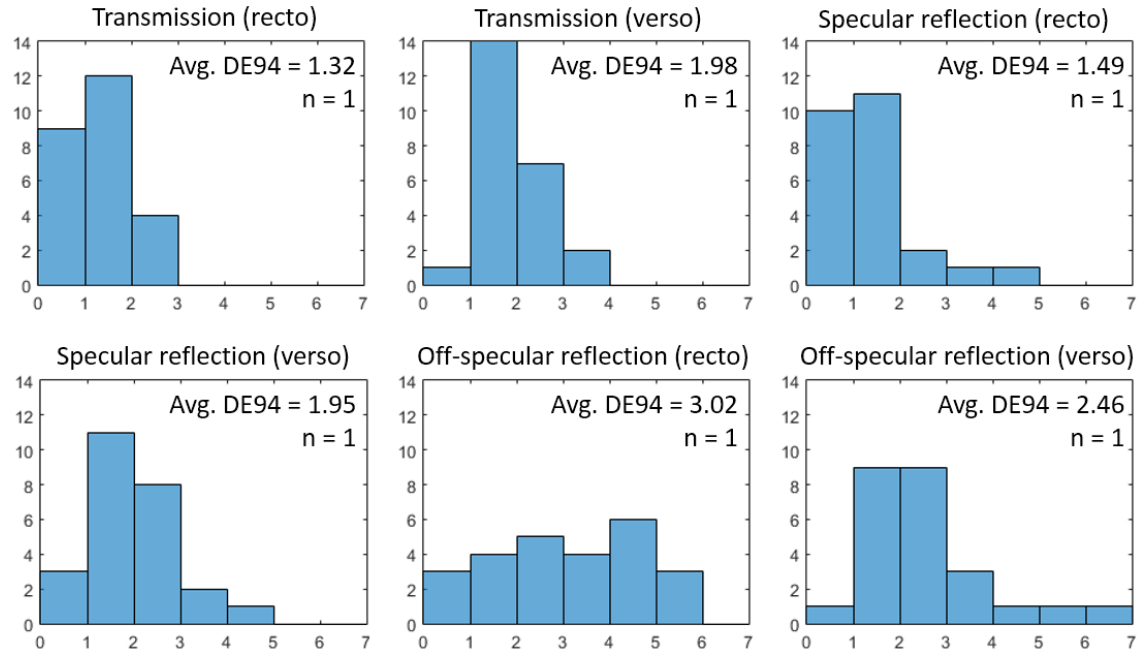


Figure 6.17: Histograms of the CIE94 color differences obtained between measured and predicted spectra using the Neugebauer model for the 25 primary combinations studied. A global average of 2.04 CIE94 units was obtained.

Even though the samples are non-scattering, we wanted to see whether the Yule-Nielsen modified Spectral Neugebauer model could be more accurate than the Neugebauer model, with an optimized n value (known to be correlated with the optical dot gain induced by the scattering within the printing support). A different n value was selected for each measurement configuration, in order to minimize the average CIE94 color difference obtained between the measured and predicted colors from the extracted spectra of all the 25 halftones in our set of samples. The optimization was done by means of an exhaustive evaluation of n parameters in the range between 0.1 and 10 units, in steps of 0.1. The results obtained are shown in Figure 6.18. The n values obtained are consistent with the ones obtained for non-scattering materials in previous studies.⁸⁵ The prediction accuracy remained nearly the same in all the measurement configurations compared to the Neugebauer model, except for the off-specular front-side mode, where the optimization led to an improvement from 3.09 to 2.53 CIE94 units. The global average accuracy (considering all the geometries) led to an improvement from 2.04 to 1.95 CIE94 units in comparison to the Neugebauer model.

We can conclude that the Spectral Neugebauer model is not much less accurate than its Yule-Nielsen modified version, and it is simpler and faster for further computations in color management.

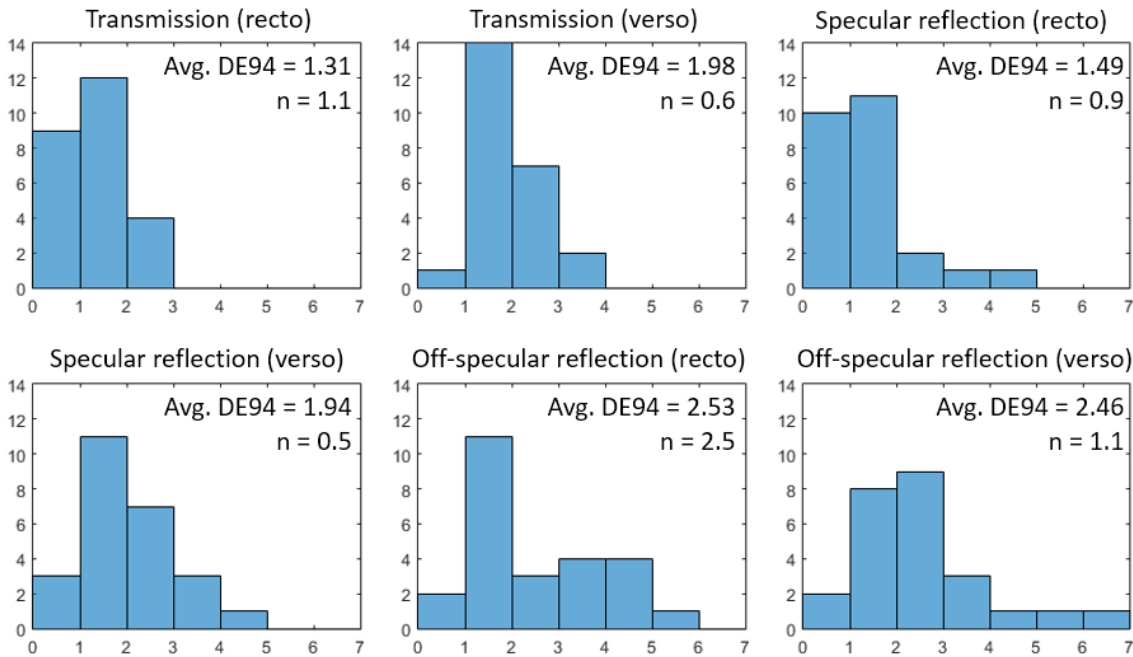


Figure 6.18: Histograms of the CIE94 color differences obtained between measured and predicted spectra for the 25 primary combinations studied, using the Yule-Nielsen modified Spectral Neugebauer model with optimized n parameter. A global average of 1.95 CIE94 units was obtained.

6.6 Color gamut extension by using halftoning

By using the Spectral Neugebauer model in each geometrical configuration, we can predict with the accuracy presented in the previous section, the colors that can be produced by the combination of the numerous primaries produced by the PICSLUP system, shown from Figure 6.3 to Figure 6.8.

To obtain the complete set of colors that can be produced with the PICSLUP system, we exhaustively predicted the colors produced by the halftoning mixture of every pair of primaries from the set of 330 squares defined in Section 6.1. For each pair of primaries, 10 different values between 0 and 1 were used in the Spectral Neugebauer model for a_1 (the surface coverage of the first primary), while the value a_2 corresponding to the coverage of the second primary was equivalent to $1 - a_1$.

From these predictions we found that in all the geometries, the predicted colors obtained by halftoning with each pair of primaries draw an almost straight line between them. An example of this can be seen in Figure 6.19, where the extended colors obtained in specular reflection mode form lines that make the volume of colors continuous and quasi convex. This volume of colors is very close to the convex hull of the set of primaries used, i.e., the minimum convex volume that contains all the primaries in a given configuration. The color gamut in each of the geometries can therefore be approximated in a simple manner as the convex hull defined by the primaries used.

The extended color gamuts obtained for each of the six measurement configurations thanks to use of halftoning are presented from Figure 6.20 to Figure 6.25.

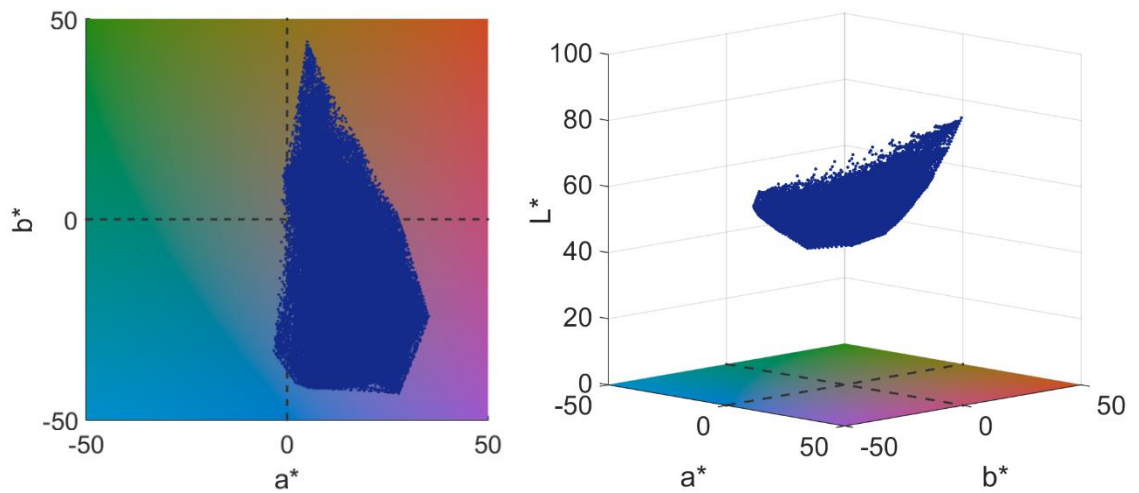


Figure 6.19: Colors obtained in specular reflection mode using the optimized YNSN model for the exhaustive halftoning mixture of primaries described above.

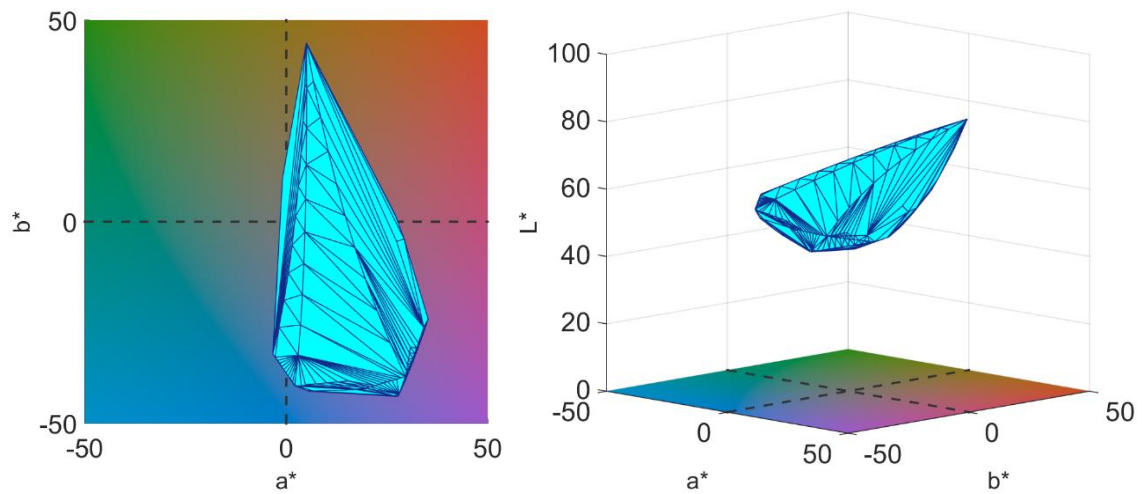


Figure 6.20: Estimated color gamut volume for the front side of PICSLUP samples in the $15^\circ:15^\circ$ specular reflection geometry.

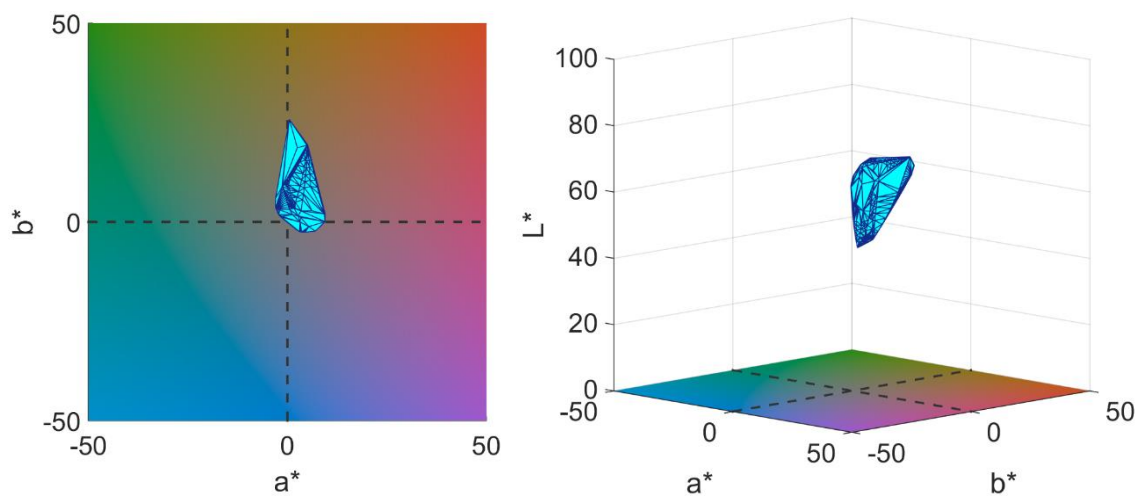


Figure 6.21: Estimated color gamut volume for the back side of PICSLUP samples in the $15^\circ:15^\circ$ specular reflection geometry.

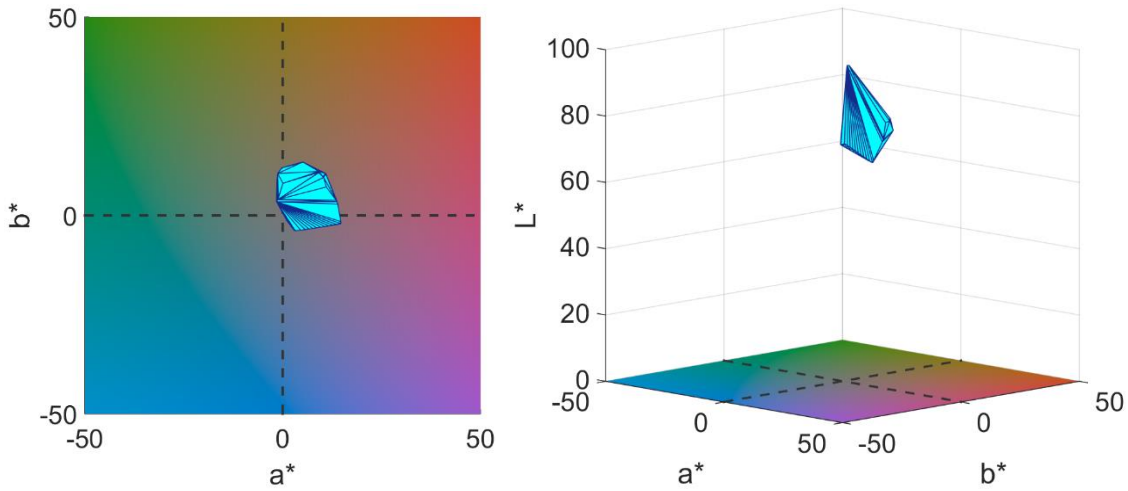


Figure 6.22: Estimated color gamut volume for the front side of PICSLUP samples in the $0^\circ:0^\circ$ transmission geometry.

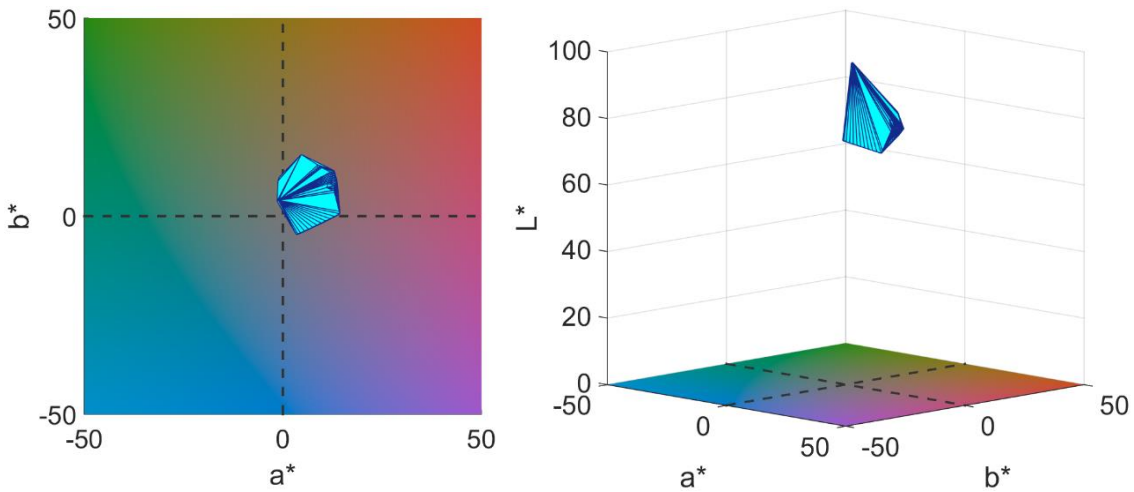


Figure 6.23: Estimated color gamut volume for the back side of PICSLUP samples in the $0^\circ:0^\circ$ transmission geometry.

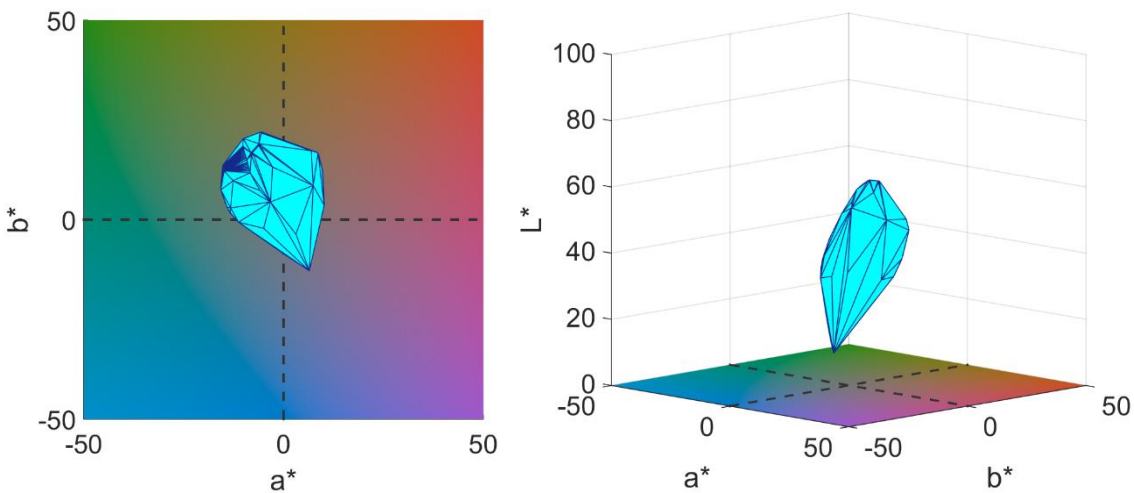


Figure 6.24: Estimated color gamut volume for the front side of PICSLUP samples in the $45^\circ:0^\circ$ off-specular reflection geometry.

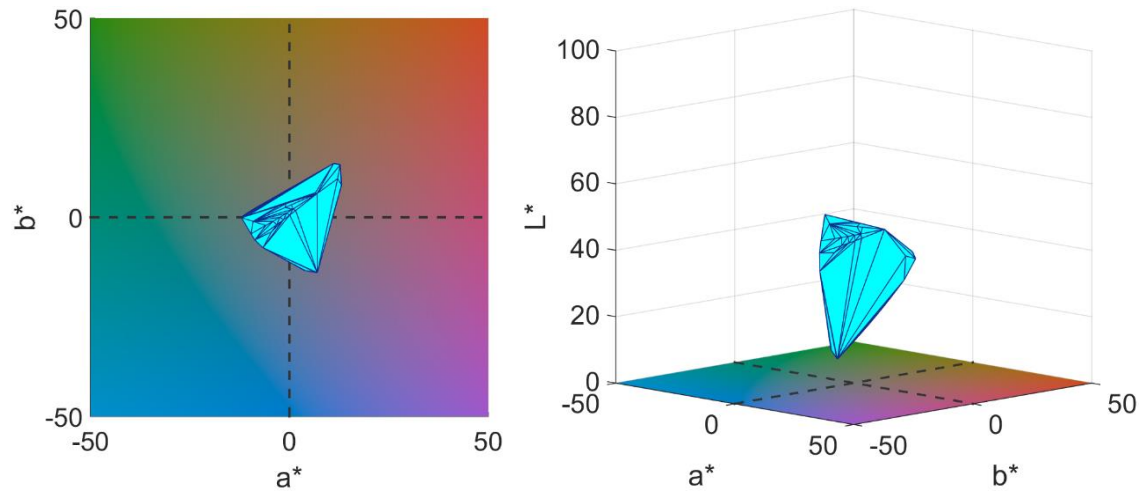


Figure 6.25: Estimated color gamut volume for the back side of PICSLUP samples in the $45^\circ:0^\circ$ off-specular reflection geometry.

6.7 Conclusion

Despite the photometric constraints and limitations that exist for characterizing the PICSLUP technology, we demonstrated that line halftoning was possible in our system by obtaining a satisfactory accuracy in the prediction of the colors that can be produced by mixing different primaries. The worst accuracy was obtained in the off-specular reflection mode where the intensity of reflected light was very low, which made the measurements prone to errors due to stray light or diffraction effects.

Comparing the color gamuts presented in Section 6.1 to the ones shown in Section 6.6, we can see that the volume of producible colors notably increased and became more convex and continuous. This is important for color imaging, where a continuous sets of colors are necessary to produce gradients present in real images.

Another advantage introduced by halftoning, is not only that the amount of colors available has increased, but also many more primaries which display different multi-geometry colors, such as the ones shown in Section 6.2, have now been created. Thanks to the large number of different primaries that can be created with halftoning, it is now easier to obtain parameters to print areas that visually match a given color *A* in one configuration while matching another target color *B* in a different configuration. This opens the possibility for some interesting imaging, design and security applications that will be discussed in Chapter 7.

7

CONCLUSIONS AND FUTURE WORK

This thesis addressed the challenging photometric and color characterization of the PICSLUP technology — a contactless printing system on functionalized glass plates which enables printing color images with multi-color properties similar to those of stained glasses and lusterwares, reproducing their transparency/specularity, and their ability to display different colors according to the respective positions of the observer and the light source. Additionally, the colors printed also depend on the polarization of light.

Many constrains described in Chapter 3, including the low availability of the printing material, its high specularity and strong goniochromaticity, posed difficult challenges for its photometric characterization. In order to have an exhaustive characterization of the colors that could be produced in the $0^\circ:0^\circ$ specular reflection geometry, a color calibration method¹³ especially suited for the microscopic observation of highly specular samples was presented in Chapter 4, whose accuracy is good in comparison to previous studies in the camera color calibration literature.^{68,73,74}

The microscope imaging system was very useful to study the properties of the colors displayed by the PICSLUP technology in the $0^\circ:0^\circ$ specular reflection mode. However, due to the gonioapparent nature of the samples studied, these measurements were not representative of the colors displayed in other illumination/observation configurations. In order to have a more complete assessment of the multi-color properties of the samples produced by the PICSLUP system, we assembled a geometry-adjustable hyperspectral imaging system, described in Chapter 5. With this system we measured a sample set representative of the colors that could be produced by the printing system on both recto and verso sides of the printed samples in the $0^\circ:0^\circ$ transmission, $15^\circ:15^\circ$ specular reflection and $45^\circ:0^\circ$ off-specular reflection configurations.

The colors obtained from these measurements in the different geometries were represented in the CIELAB color space to assess the volume of colors that could be produced, and it was noted that many of these volumes were concave and contained many

sparse regions with very few samples. In order to obtain more continuous, dense and convex color gamut volumes, in Chapter 6, we successfully tested the generation of new colors by juxtaposing printed lines of different primaries with halftoning techniques. We were able to predict with sufficient accuracy these newly produced colors thanks to the Yule-Nielsen modified Spectral Neugebauer model, which brings the advantage of allowing us to identify the parameters necessary to obtain a desired target color without the need to measure each of the numerous primaries combinations possible.

One of the most interesting characteristics of the PICSLUP system, presented in Section 6.2, is that its samples have a strong dependence on the illumination/observation geometry used, and a single printed patch can have widely different colors depending on the viewing conditions. Thanks to this multi-dimensional property of the samples, we can easily find parameters to print patches whose colors match visually in a given configuration while being completely different in other geometries. More generally, this allows us to find parameters that produce desired colors in specific geometrical configurations in the same printed area, which open the possibility for completely new visual effects for printed images that will be discussed in the following section.

7.1 Printing special effect images

The gonioapparent nature of the samples produced by the PICSLUP system introduces new visual effects for graphical arts. We propose here some examples already investigated, among the almost unlimited number of possible applications.

Simple goniochromatic imaging: This application is illustrated by the pictures shown in Figure 7.1 of one image printed with the PICSLUP system, where different colors are displayed in the transmission, specular reflection, and off-specular reflection configurations.



Figure 7.1: Image printed by the PICSLUP system captured in different geometrical configurations: (left) $0^\circ:0^\circ$ transmission, (center) $15^\circ:15^\circ$ specular reflection, and (right) $45^\circ:0^\circ$ off-specular reflection. The area of the image is 1×1 cm.

Hidden pattern: By selecting two sets of parameters that display the same color in one configuration and different colors in another configuration, we can print hidden patterns that can only be seen in a given geometrical configuration. This could be used for anti-counterfeiting and watermarking purposes. Figure 7.2 shows the colors of a

pattern designed with this objective by using colors already measured by our hyperspectral imaging system



Figure 7.2: Hidden pattern designed with colors measured from two squares from the ones printed in Section 6.1, displayed in the $0^\circ:0^\circ$ transmission recto (left) and $15^\circ:15^\circ$ specular reflection recto (right) configurations.

Hidden pattern with polarization: A similar effect can be produced even in the same geometrical configuration by the use of polarization. As shown in Section 4.12, there are many parameters that produce samples that are very sensitive to polarization. We can exploit this property by choosing two sets of parameters that display the same color without polarization to obtain a homogeneous appearance, and display the hidden pattern when polarization is applied

2-geometry or n-geometry patterns: A printed area can display different patterns in two or more geometrical configurations by carefully selecting the printing parameters used. For the 2-geometry case, consider the diagram shown in Figure 7.3

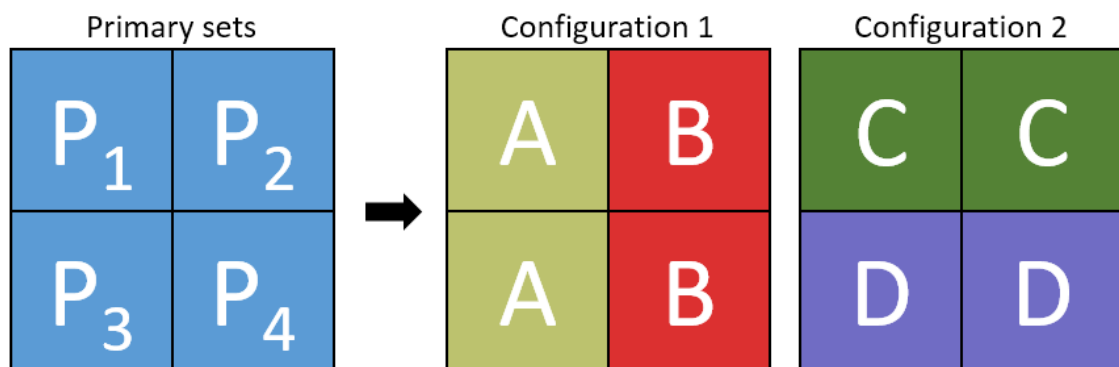


Figure 7.3: Diagram of printed areas with four sets of hypothetical parameters selected in order to produce two vertical rectangles on Configuration 1 and two horizontal rectangles in Configuration 2.

By selecting 4 sets of parameters: P_1 , P_2 , P_3 and P_4 , such that:

- P_1 and P_3 display color A in configuration 1
- P_2 and P_4 display color B in configuration 1
- P_1 and P_2 display color C in configuration 2
- P_3 and P_4 display color D in configuration 2

- A is perceptually different than B
- C is perceptually different than B

we can display different patterns in the two given configurations. To illustrate this application, we designed a 2-geometry pattern from samples measured by our hyperspectral imaging system. Figure 7.6 shows the colors produced in two different geometrical configurations by the four sets of parameters selected. These colors are then used to design the spatial arrangement of the areas that will be printed with each of the selected parameter sets. Figure 7.5 shows the spatial arrangement we designed to produce our 2-geometry pattern. The resulting colors produced displayed in the two configurations used is shown in Figure 7.6.

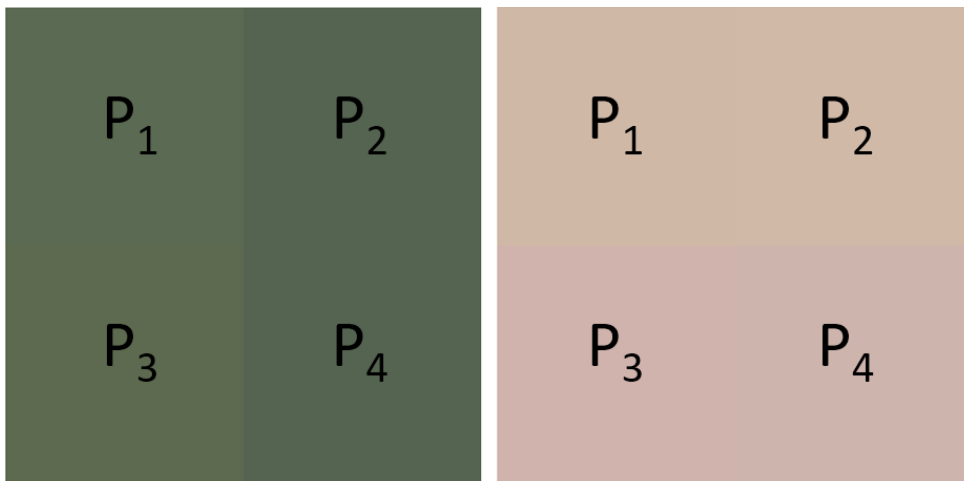


Figure 7.4: Colors produced by the four parameter sets selected in the 45°:0° off-specular reflection recto (left) and 0°:0° transmission recto (right) configurations.

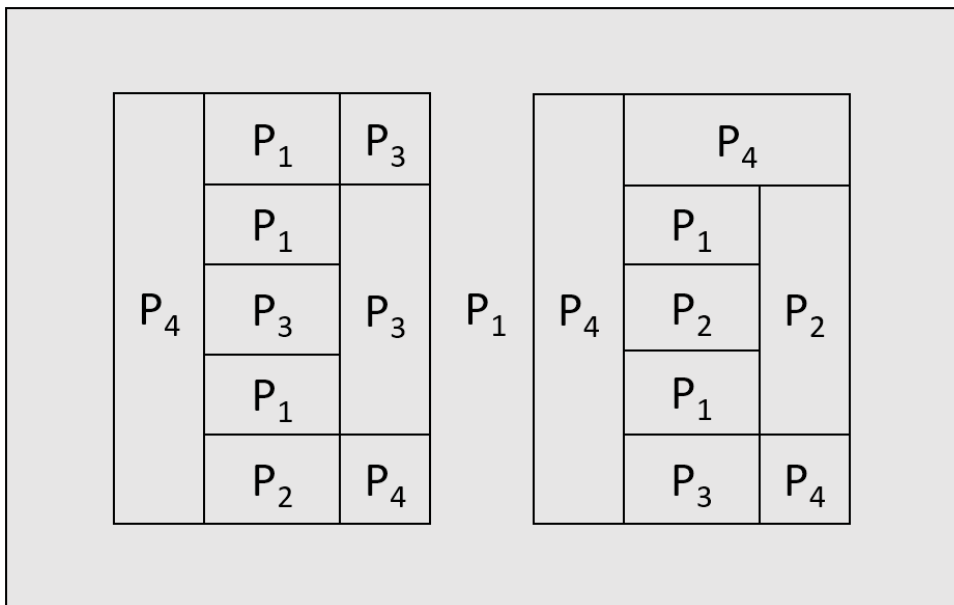


Figure 7.5: Spatial arrangement designed with the four parameter sets selected to produce our 2-geometry pattern.

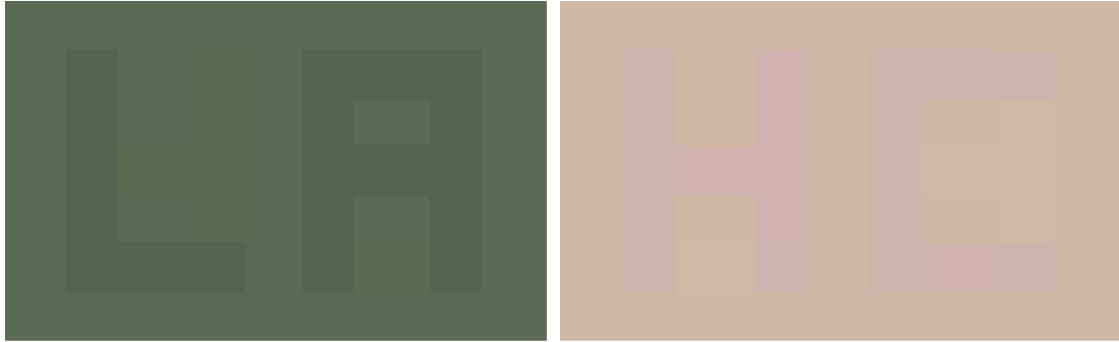


Figure 7.6: Resulting colors displayed by the 2-geometry pattern designed in the 45°:0° off-specular reflection recto (left) and 0°:0° transmission recto (right) configurations.

To produce n-geometry patterns, a similar parameter set selection process is performed by selecting the corresponding color matches and color mismatches in each of the configurations used.

Multi-view color imaging: The same idea described for the n-geometry patterns, can be further developed into multi-view imaging, where not just monochromatic patterns but full-color images are displayed in different geometrical configurations. In this case the color-matching parameter selection is performed in a pixel-per-pixel manner. Due to the increased numbers of colors required in this scenario, the difficulty to obtain parameters to fulfill the color requirements of every pixel is greater, and the primaries required to reproduce the images with perfect accuracy might not be available to the printing system. The process of selecting the printing parameters per pixel in order to produce the best approximation of the target images in each of the geometrical configurations desired can be expressed as an optimization problem, where the goal is to produce the images with the *best color appearance* in each of the geometries concerned. The different ways of approaching this problem depend on the precise meaning of the term *best color appearance*. As an initial approach, we can consider each pixel separately and assess its color appearance quality according to the Mean Square Error (MSE), considering the errors as the ΔE color differences (e.g. CIE94 or CIEDE2000) calculated in each of the geometries concerned between the target and produced colors for each pixel:

$$MsePixel_i = \frac{1}{n} \sum_{j=1}^n \Delta E(t_{i,j}, p_{i,j})^2 \quad (44)$$

where i is the current pixel, n is the number of geometries considered, $t_{i,j}$ is the target color in pixel i and geometry j , and $p_{i,j}$ is the color produced by the parameters selected in pixel i and geometry j . Since the pixels are evaluated independently according to this definition, the goal of the problem is to select the printing patterns for each pixel in order to minimize its MSE. An initial metric to evaluate the overall quality achieved for the image can be the average MSE obtained from all the pixels in the image:

$$AvgMse = \frac{1}{num\ pixels} \sum_{k=1}^{num\ pixels} MsePixel_k \quad (45)$$

This is a very simple initial approach. More advanced methods that take into account the spatial appearance of the images and use color gamut mapping techniques to address the reduced gamut volumes in some configurations, will be proposed as future work.

7.2 Future work

A color characterization of the PICS LUP printing system has been performed for several geometries. Nevertheless, given the complexity of the properties of the samples produced, there are several areas left to explore and improve based on the work presented in this study.

A direct continuation of the work presented here is to study and develop the different applications mentioned in Section 7.1, since some of them were discussed in a theoretical manner based on the measurements we performed with our hyperspectral imaging system and have not physically been produced yet due technical constraints and a lack of time.

An initial approach was presented to select printing parameters for the innovative multi-view color imaging application. Further studies focused on perception and color appearance are necessary in order to take into account the spatial distribution of colors when selecting the printing primaries in order to produce images with acceptable color appearance. These include evaluations of color gamut mapping algorithms in order to address the limited color gamut volumes in some geometries.

Since color-difference formulas depend on many viewing condition factors⁴³ and on the type of materials¹⁴ observed, a better understanding and modeling of perceived color differences could be achieved by performing psychophysical studies using a larger number of color pairs displayed in different geometrical configurations. These results could be useful for the automatic selection of patterns that are required to look perceptually similar or different in given configurations.

A further characterization of the complex color change with precise angle variations in specular reflection, off-specular reflection, and transmission configurations, would be of great interest. In addition, the colors obtained by the use of different angles of polarization in all these different geometries can be explored.

A particularly striking effect is produced in samples with grazing angles (small angle between the direction and the surface plane) of observation and illumination that requires further study and characterization. An example of these effects is shown in Figure 7.7. The appearance of this same sample in other configurations was shown in Figure 5.12, sample (b).

Finally, the PICS LUP printing system is currently also being developed for paper⁷ and plastic⁶ substrates, although with lower color capabilities at the moment. In Figure 7.8 we can see an image of the colors displayed in different geometrical configurations by samples printed in paper and plastic supports. As a future work, we propose to perform the same characterizations and explore similar applications as the ones studied for glass supports.

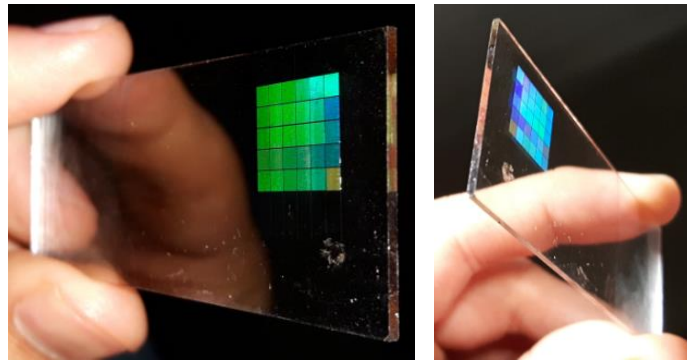


Figure 7.7: Same sample displayed in Figure 5.12 Sample (b), observed with small angles with respect to the surface plane in the following configurations: Off-specular reflection verso with the approximately the same position for illumination and observation (left), and transmission recto with diffuse illumination from behind (right).

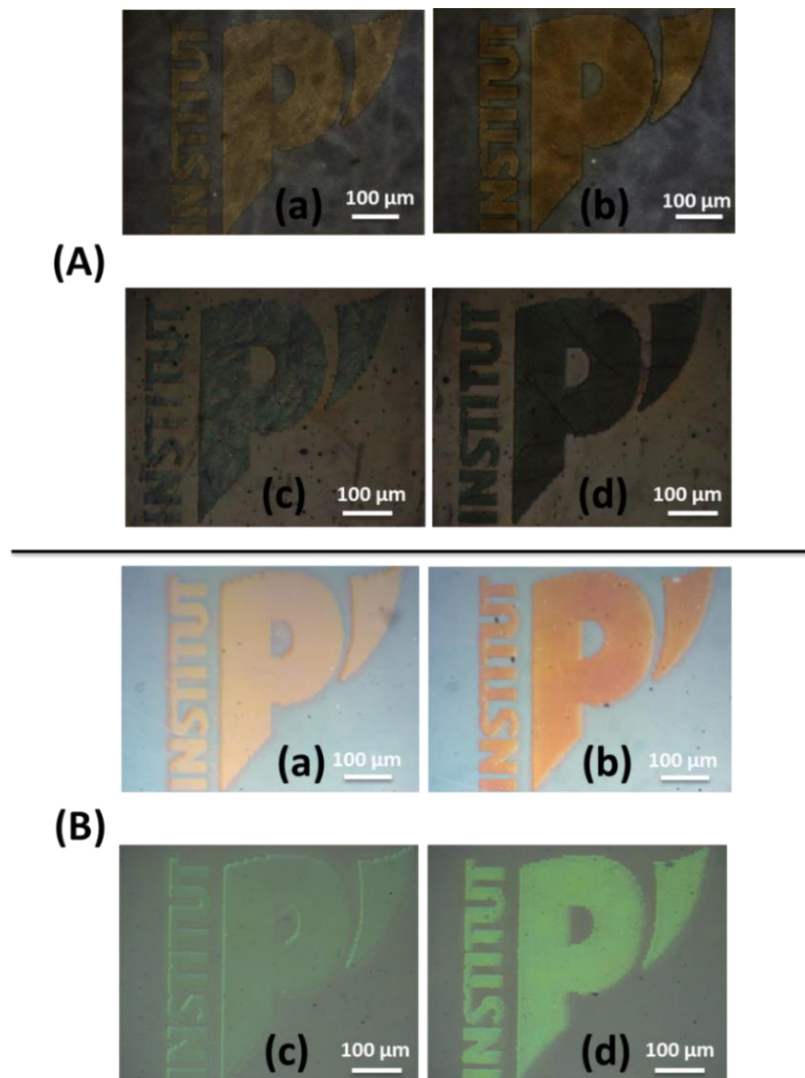


Figure 7.8: Microscope images of printed of samples printed on paper substrates (A): observed in off-specular reflection ((a) and (b)) and in specular reflection ((c) and (d)); and printed on plastic PET substrates (B): observed in regular transmission ((a) and (b)) and in specular reflection ((c) and (d)).

7.3 Potential applications

Special effects in printing, such as the display of multiple images by one print, are more and more appreciated by the security printing domain to avoid illicit copy of documents. The special effects can be based on goniochromatism, like optical variable devices (OVDs), or on the display of different images according to the illumination and/or observation conditions.

Only a few printing techniques can produce supports displaying different images according to the illumination and viewing conditions. We can mention lenticular prints,⁸⁶ where the displayed image varies with the viewing angle; a high resolution print is topped by a microlens array, focusing on different points of the print according to the viewing angle. Other techniques based on multi-image printing use a mixing of special and traditional inks: fluorescent inks enable displaying different images according to the spectral power distribution of the light source,⁸⁹ or the power of UV;⁹⁰ metallic inks, mixed with traditional inks, produce specular effects which can be used to display different images in the specular and out-of-specular directions.⁹¹ Recto-verso prints can also display different images according to whether they are illuminated on the observed side (reflection mode) or the other side (transmission mode).⁹² Similar effects can be produced by stacking printed transparency films.⁹³ In all these examples, the number of images which can be displayed is limited (except in lenticular printing where the number of images can be high but the resolution is reduced in proportion) and the colors displayed in one configuration often depend on the colors displayed on the other configuration, which limits the graphical possibilities.

In contrast with these existing techniques, the PICLSUP technology enables printing high-resolution multi-color images where the colors displayed in the different configurations are more independent of each other. The technology has also other advantages for security:

- **Numerous primaries and high resolution:** Unlike conventional printing systems that have three or four printing primaries, we can obtain a large number of primaries in the PICSLUP system by varying the printing parameters, allowing the selection of customizable subsets for specific applications. Halftoning is possible and enables increasing the color gamut in each configuration, or finding new color combinations to display in different configurations, but it is not mandatory. The printing resolution can therefore be as high as the laser resolution, which allows the printing of (invisible) micropatterns. The lines printed by the PICSLUP system produces lines with a width varying mostly between 20 and 40 μm , which gives it a printing resolution between 600 and 1200 lines per inch (LPI). This resolution is reduced if halftoning is required since the effective primary line size is increased by the combination of several lines. By using 4-line halftoning primaries, the resolution effective is reduced to between 150 and 300 LPI, which is still a good resolution in comparison with high quality glossy paper prints having up to 150 LPI.⁹⁴

- **Line continuity:** Even though the laser scanning process that is currently used enables only parallel line scanning, we can adapt it to draw custom curves, and create high resolution guilloches, used for a long time in banknotes as they are difficult to reproduce with standard digital printers.
- **Color palettes:** The high translucency and the mix between absorption and interferential colors also opens new (gonio)chromatic palettes for artists and designers. The possibility to reveal patterns by polarization is also rather new.

Beyond these applications for security, PICSLUP is a unique solution for coloring translucent materials such as glass or ceramics, which producing high-resolution images. We can imagine in the future innovative decorations for tableware or lighting. The custom coloration of glass with numerous sheen or reflection effects is also a new material for artists, especially stained glass manufacturers or sculptors who work the stacking of glass plates.⁹⁵

APPENDIX 1:

FILM ELABORATION AND PRINTING

The TiO₂ films are elaborated using a solgel synthesis method that was published previously.^{87,88} A mixed solution of titanium tetraisopropoxide (TTIP, Aldrich; 97%) and acetylacetone (AcAc, Aldrich; 99%) is used as precursor solution for the synthesis of titania films. A hydrochloric acid solution (HCl, Roth; 37%) is added to an ethanol (EtOH, Carlo Erba; absolute)/P123 (Aldrich; MW: 5000) solution and mixed with the precursor solution under vigorous stirring. The mixture is stirred for 30 min. Then, de-ionized water (H₂O) is slowly added to the well-mixed solution and aged with stirring at room temperature for about 6 h. Molar ratios of these reagents are controlled at TTIP/P123/ethanol/HCl/H₂O/AcAc = 1:0.025:28.5:0.015:29.97:0.5. The titania thin films are dipcoated at a drawing speed of 7 cm/min and annealed at 340°C for 4 h to remove the copolymer and form the mesoporous titania films. Their thickness is 230 ± 50 nm. Solgel synthesis and dip-coating are conducted in a clean room where the relative humidity is kept at 45% (±5%). Silver ions are then introduced within the mesoporosity by soaking the films for 1 h in an aqueous ammoniacal silver nitrate solution [Ag(NH₃)₂]⁺NO₃⁻ that is obtained as follows: a silver nitrate solution is prepared in an EtOH/H₂O (1:1 v/v) mixture at a concentration fixed at 1.5 M; then a NH₃ solution is added until a clear solution is obtained. The films are then rinsed with water and dried at room temperature for 12 h.

At this stage, the films are transparent and colorless. Their transmission spectrum is flat without measurable absorption. However, they contain numerous small silver nanoparticles that are about 1–3 nm in diameter; these have been fully characterized in previous studies by high resolution transmission electron microscopy and low-frequency Raman scattering.⁸⁸ Due to the localized surface plasmon resonance (LSPR) of these nanoparticles, the film absorption is not null even though it is not measurable. And, it leads to a temperature increase that can exceed several hundreds of degrees in the film when the incident laser intensity is high enough.⁸ This temperature rise only occurs above an intensity threshold that must be exceeded to generate the self-organized growth of silver nanoparticles and to produce the film color. This intensity threshold depends on the laser wavelength and intensity as well as on intrinsic parameters of the film.

The samples are colored with an Ar–Kr continuous wave laser emitting at various wavelengths in the visible range. The experiments are carried out at 488, 514, 530, and 647 nm wavelengths. The laser beam, whose power can be tuned, is weakly focused on the sample with a 10× objective lens (MPLN 10× from Olympus) under normal incidence. The laser focusing can be degraded by shifting the sample from the focal plane to decrease the laser intensity and widen the spot diameter on the sample from approximately 10 μm half-intensity at the minimum up to typically 50 μm . The latter is moved during illumination at a constant speed varying from 50 $\mu\text{m/s}$ to 30 mm/s in order to draw linear patterns.

APPENDIX 2:

CALCULATION OF RGB TO XYZ TRANSFORMATION MATRICES

The matrix \mathbf{M} that performs a linear transformation between the RGB and the XYZ color spaces can be obtained from the (x,y) chromaticity coordinates of the primaries of the RGB system (x_r, y_r), (x_g, y_g), and (x_b, y_b), and the XYZ tristimulus values of the white reference (X_w, Y_w, Z_w) as follows:

$$[\mathbf{M}] = \begin{bmatrix} S_r X_r & S_g X_g & S_b X_b \\ S_r Y_r & S_g Y_g & S_b Y_b \\ S_r Z_r & S_g Z_g & S_b Z_b \end{bmatrix}$$

where

$$X_r = x_r/y_r \quad , \quad Y_r = 1 \quad , \quad Z_r = (1 - x_r - y_r)/y_r \quad (46)$$

$$X_g = x_g/y_g \quad , \quad Y_g = 1 \quad , \quad Z_g = (1 - x_g - y_g)/y_g \quad (47)$$

$$X_b = x_b/y_b \quad , \quad Y_b = 1 \quad , \quad Z_b = (1 - x_b - y_b)/y_b \quad (48)$$

$$\begin{bmatrix} S_r \\ S_g \\ S_b \end{bmatrix} = \begin{bmatrix} X_r & X_g & X_b \\ Y_r & Y_g & Y_b \\ Z_r & Z_g & Z_b \end{bmatrix}^{-1} \begin{bmatrix} X_w \\ Y_w \\ Z_w \end{bmatrix} \quad (49)$$

To obtain the XYZ tristimulus values, the matrix transformation \mathbf{M} is applied to RGB tristimulus values as follows:

$$\begin{bmatrix} X \\ Y \\ Z \end{bmatrix} = [\mathbf{M}] \begin{bmatrix} R \\ G \\ B \end{bmatrix} \quad (50)$$

BIBLIOGRAPHY

- [1] I. Freestone, N. Meeks, M. Sax, and C. Higgitt, “The Lycurgus cup: a roman nanotechnology,” *Gold Bulletin*, vol. 40, no. 4, pp. 270–277, 2007.
- [2] D. Barber and I. Freestone, “An investigation of the origin of the colour of the Lycurgus cup by analytical transmission electron microscopy,” *Archaeometry*, vol. 32, no. 1, pp. 33–45, 1990.
- [3] J. Lafait, S. Berthier, C. Andraud, V. Reillon, and J. Boulenguez, “Physical colors in cultural heritage: surface plasmons in glass,” *Comptes Rendus Physique*, vol. 10, no. 7, pp. 649–659, 2009.
- [4] V. Reillon, S. Berthier, and C. Andraud, “Optical properties of lusted ceramics: complete modelling of the actual structure,” *Applied Physics A*, vol. 100, no. 3, pp. 901–910, 2010.
- [5] P. Sciau, *Nanoparticles in Ancient Materials: The Metallic Lustre Decorations of Medieval Ceramics*. INTECH Open Access Publisher, 2012, vol. 115.
- [6] F. Tricot, F. Vocanson, D. Chaussy, D. Beneventi, S. Reynaud, Y. Lefkir, and N. Destouches, “Flexible photochromic $\text{TiO}_2\text{:Ag}$ thin film elaborated by printing techniques.” in *E-MRS 2015, Spring Meeting, symposium H, Nanoparticles in dielectric matrix for electronics and optics: from the fabrication to the devices*, 2015.
- [7] D. K. Diop, L. Simonot, N. Destouches, G. Abadias, F. Pailloux, P. Guérin, and D. Babonneau, “Magnetron sputtering deposition of Ag/TiO_2 nanocomposite thin films for repeatable and multicolor photochromic applications on flexible substrates,” *Advanced Materials Interfaces*, vol. 2, no. 14, 2015.
- [8] N. Crespo-Monteiro, N. Destouches, L. Saviot, S. Reynaud, T. Epicier, E. Gamet, L. Bois, and A. Boukenter, “One-step microstructuring of TiO_2 and Ag/TiO_2 films by continuous wave laser processing in the uv and visible ranges,” *The Journal of Physical Chemistry C*, vol. 116, no. 51, pp. 26857–26864, 2012.
- [9] N. Destouches, N. Crespo-Monteiro, G. Vitrant, Y. Lefkir, S. Reynaud, T. Epicier, Y. Liu, F. Vocanson, and F. Pigeon, “Self-organized growth of metallic nanoparticles in a thin film under homogeneous and continuous-wave light excitation,” *Journal of Materials Chemistry C*, vol. 2, no. 31, pp. 6256–6263, 2014.
- [10] N. Destouches, N. Crespo-Monteiro, T. Epicier, Y. Lefkir, F. Vocanson, S. Reynaud, R. Charrière, and M. Hebert, “Permanent dichroic coloring of

- surfaces by laser-induced formation of chain-like self-organized silver nanoparticles within crystalline titania films,” in *SPIE LASE*. International Society for Optics and Photonics, 2013, pp. 860905–860905.
- [11] N. Destouches, J. Martnez-García, M. Hébert, N. Crespo-Monteiro, G. Vitrant, Z. Liu, A. Trémeau, F. Vocanson, F. Pigeon, S. Reynaud *et al.*, “Dichroic colored luster of laser-induced silver nanoparticle gratings buried in dense inorganic films,” *JOSA B*, vol. 31, no. 11, pp. C1–C7, 2014.
- [12] J. Martnez-García, M. Hébert, A. Trémeau, N. Crespo-Monteiro, and N. Destouches, “Multi-color properties of silver glaze images photo-engraved on glass plates,” in *Color and Imaging Conference*, vol. 2015, no. 1. Society for Imaging Science and Technology, 2015, pp. 116–120.
- [13] J. Martínez-García, M. Hébert, and A. Trémeau, “Color calibration of an RGB digital camera for the microscopic observation of highly specular materials,” in *IS&T/SPIE Electronic Imaging*, no. 93980I. International Society for Optics and Photonics, 2015.
- [14] M. Melgosa, J. Martnez-García, L. Gómez-Robledo, E. Perales, F. M. Martnez-Verdú, and T. Dauser, “Measuring color differences in automotive samples with lightness flop: A test of the audi2000 color-difference formula,” *Optics express*, vol. 22, no. 3, pp. 3458–3467, 2014.
- [15] O. E. Dictionary, “Oxford english dictionary online,” *Mount Royal College Lib., Calgary*, vol. 14, 2004.
- [16] J. Hardeberg, Acquisition and reproduction of color images: colorimetric and multispectral approaches. Universal-Publishers, 2001.
- [17] “Zami, Zuly: The Electromagnetic Spectrum. Accessed on 2016-05-27.” [Online]. Available: <http://www.zulyzami.com/The+Electromagnetic+Spectrum>
- [18] I. Newton, “New theory about light and colors,” *Philosophical Transactions of the Royal Society of London*, 1671.
- [19] R. S. Berns, Billmeyer and Saltzman’s Principles of Color Technology. New York, John Wiley & Sons, 2000.
- [20] Joint ISO/CIE Standard, “CIE Standard Illuminants for Colorimetry,” ISO 10526 (1999) / CIE S 005 E (1998).
- [21] K. B. Wolf and G. Krotzsch, “Geometry and dynamics in refracting systems,” *European Journal of Physics*, vol. 16, no. 1, p. 14, 1995.
- [22] M. Born and E. Wolf, Principles of optics: electromagnetic theory of propagation, interference and diffraction of light. CUP Archive, 2000.
- [23] P. Bouguer, Essai d’optique sur la gradation de la lumière. Jombert, 1729.
- [24] S. K. Shevell, *The science of color*. Elsevier, 2003.
- [25] S. Kinoshita, *Structural colors in the realm of nature*. World Scientific, 2008, vol. 368.

-
- [26] D. B. Judd, "Terms, definitions, and symbols in reflectometry," *JOSA*, vol. 57, no. 4, pp. 445–450, 1967.
- [27] F. Nicodemus, J. Richmond, J. Hsia, I. Ginsberg, and T. Limperis, *Geometrical considerations and nomenclature for reflectance*. US Department of Commerce, National Bureau of Standards, 1977, vol. 160.
- [28] CIE Central Bureau, "Absolute methods for reflection measurements"; CIE Technical Report (1979). CIE, 1979.
- [29] L. Simonot, M. Hébert, and D. Dupraz, "Goniocolorimetry: from measurement to representation in the ciela color space," *Color Research & Application*, vol. 36, no. 3, pp. 169–178, 2011.
- [30] N. Ohta and A. Robertson, *Colorimetry: fundamentals and applications*. John Wiley & Sons, 2006.
- [31] A. Stockman, D. I. MacLeod, and N. E. Johnson, "Spectral sensitivities of the human cones," *JOSA A*, vol. 10, no. 12, pp. 2491–2521, 1993.
- [32] S. CIE, "017/e: 2011," *ILV: International Lighting Vocabulary*, vol. 17.
- [33] ASTM E284-13b, Standard Terminology of Appearance, ASTM International, West Conshohocken, PA, 2013, www.astm.org, Tech. Rep.
- [34] G. Wyszecki and W. S. Stiles, *Color Science*. Wiley New York, 1982, vol. 8.
- [35] R. W. G. Hunt, *The reproduction of colour*. John Wiley & Sons, 2005.
- [36] CIE Central Bureau, "Colorimetry," CIE Pub. 15, Vienna (2004).
- [37] W. D. Wright, "A re-determination of the trichromatic coefficients of the spectral colours," *Transactions of the Optical Society*, vol. 30, no. 4, p. 141, 1929.
- [38] J. Guild, "The colorimetric properties of the spectrum," *Philosophical Transactions of the Royal Society of London. Series A, Containing Papers of a Mathematical or Physical Character*, vol. 230, pp. 149–187, 1932.
- [39] H. S. Fairman, M. H. Brill, H. Hemmendinger *et al.*, "How the cie 1931 color-matching functions were derived from wright-guild data," *Color Research & Application*, vol. 22, no. 1, pp. 11–23, 1997.
- [40] D. L. MacAdam, "Visual sensitivities to color differences in daylight*," *JOSA*, vol. 32, no. 5, pp. 247–274, 1942.
- [41] M. Luo and B. Rigg, "Chromaticity-discrimination ellipses for surface colours," *Color Research & Application*, vol. 11, no. 1, pp. 25–42, 1986.
- [42] CIE Publ. No. 101, "Parametric effects in colour-difference evaluation", Central Bureau of the CIE, Vienna. Technical Report 4, August 1993.
- [43] S.-S. Guan and M. R. Luo, "Investigation of parametric effects using small colour differences," *Color Research & Application*, vol. 24, no. 5, pp. 331–343, 1999.

- [44] R. S. Berns, D. H. Alman, L. Reniff, G. D. Snyder, and M. R. Balonon-Rosen, "Visual determination of suprathreshold color-difference tolerances using probit analysis," *Color Research & Application*, vol. 16, no. 5, pp. 297–316, 1991.
- [45] R. G. Kuehni, "Variability in estimation of suprathreshold small color differences," *Color Research & Application*, vol. 34, no. 5, pp. 367–374, 2009.
- [46] CIE Central Bureau, "Industrial colour-difference evaluation," CIE Pub. 116, Vienna (1995).
- [47] F. Clarke, R. McDonald, and B. Rigg, "Modification to the jpc79 colour–difference formula," *Journal of the Society of Dyers and Colourists*, vol. 100, no. 4, pp. 128–132, 1984.
- [48] CIE Publication 142. "Improvement to industrial colour-difference evaluation". CIE Central Bureau, Vienna. Technical report, 2001.
- [49] M. Luo, G. Cui, and B. Rigg, "Further comments on ciede2000," *Color Research & Application*, vol. 27, no. 2, pp. 127–128, 2002.
- [50] R. G. Kuehni, "Ciede2000, milestone or final answer?" *Color Research & Application*, vol. 27, no. 2, pp. 126–127, 2002.
- [51] G. Sharma, W. Wu, and E. N. Dalal, "The ciede2000 color-difference formula: Implementation notes, supplementary test data, and mathematical observations," *Color Research & Application*, vol. 30, no. 1, pp. 21–30, 2005.
- [52] I. E. Commission *et al.*, "Multimedia systems and equipment–colour measurement and management–part 2-1: Colour management–default rgb colour space–srgb," IEC 61966-2-1, Tech. Rep., 1999.
- [53] K. Lam, "Metamerism and colour constancy." Ph.D. dissertation, University of Bradford, 1985.
- [54] M. E. Chevreul, *The principles of harmony and contrast of colours, and their applications to the arts.* Longman, Brown, Green, and Longmans, 1855.
- [55] M. White, "The effect of the nature of the surround on the perceived lightness of grey bars within square-wave test gratings," *Perception*, vol. 10, no. 2, pp. 215–230, 1981.
- [56] R. W. Burnham, "Bezold's color-mixture effect," *The American journal of psychology*, vol. 66, no. 3, pp. 377–385, 1953.
- [57] R. W. G. Hunt, "Light and dark adaptation and the perception of color," *JOSA*, vol. 42, no. 3, pp. 190–199, 1952.
- [58] F. W. Billmeyer, "Quantifying color appearance visually and instrumentally," *Color Research & Application*, vol. 13, no. 3, pp. 140–145, 1988.
- [59] D. M. Purdy, "The bezold-brücke phenomenon and contours for constant hue," *The American Journal of Psychology*, vol. 49, no. 2, pp. 313–315, 1937.

-
- [60] W. d. W. Abney, "On the change in hue of spectrum colours by dilution with white light," *Proceedings of the Royal Society of London. Series A, Containing Papers of a Mathematical and Physical Character*, pp. 120–127, 1909.
- [61] C. Padgham, "The direct estimation of the luminosity of coloured light sources," *Vision research*, vol. 11, no. 6, pp. 577–590, 1971.
- [62] M. Hébert, "Optical models for color reproduction," Institut d'Optique Graduate School, Saint-Etienne, Tech. Rep., 2013.
- [63] M. Hébert, R. D. Hersch, and P. Emmel, "Fundamentals of optics and radiometry for color reproduction," *Handbook of Digital Imaging*, 2015.
- [64] DIN - German Institute for Standardization, "Colorimetry - Part 7: Measuring conditions for object colours," DIN 5033-7:2014-10 (2014).
- [65] G. Sharma and R. Bala, *Digital Color Imaging Handbook*. CRC press, 2002.
- [66] Joint ISO/CIE Standard, "CIE Colorimetry – Part 4: 1976 L*a*b* Colour Space," ISO 11664-4 E (2008) / CIE S 014-4 E (2007).
- [67] V. Cheung, S. Westland, D. Connah, and C. Ripamonti, "A comparative study of the characterisation of colour cameras by means of neural networks and polynomial transforms," *Coloration technology*, vol. 120, no. 1, pp. 19–25, 2004.
- [68] R. Charrière, M. Hébert, A. Trémeau, and N. Destouches, "Color calibration of an RGB camera mounted in front of a microscope with strong color distortion," *Applied optics*, vol. 52, no. 21, pp. 5262–5271, 2013.
- [69] J. D. Murray and W. VanRyper, *Encyclopedia of graphics file formats*, 2nd ed. O'Reilly, 1996, vol. 1.
- [70] A. Artusi and A. Wilkie, "Novel color printer characterization model," *Journal of Electronic Imaging*, vol. 12, no. 3, pp. 448–458, 2003.
- [71] P.-C. Hung, "Colorimetric calibration for scanners and media," in *Electronic Imaging '91, San Jose, CA*. International Society for Optics and Photonics, 1991, pp. 164–174.
- [72] D. Nébouy, M. Hébert, T. Fournel, N. Larina, and J.-L. Lesur, "Prediction of the spectral reflectance of laser-generated color prints by combination of an optical model and learning methods," *JOSA A*, vol. 32, no. 9, pp. 1661–1671, 2015.
- [73] J. Quintana, R. Garcia, and L. Neumann, "A novel method for color correction in epiluminescence microscopy," *Computerized Medical Imaging and Graphics*, vol. 35, no. 7, pp. 646–652, 2011.
- [74] P. Jackman, D.-W. Sun, and G. ElMasry, "Robust colour calibration of an imaging system using a colour space transform and advanced regression modelling," *Meat science*, vol. 91, no. 4, pp. 402–407, 2012.
- [75] M. Lequime, M. Zerrad, C. Deumié, and C. Amra, "A goniometric light scattering instrument with high-resolution imaging," *Optics Communications*, vol. 282, no. 7, pp. 1265–1273, 2009.

- [76] P. Seroul, M. Hébert, and M. Jomier, “Hyperspectral imaging system for in-vivo quantification of skin pigments,” in *IFSCC*, pp. 123–132, 2014.
- [77] R. Jolivot, Y. Benezeth, and F. Marzani, “Skin parameter map retrieval from a dedicated multispectral imaging system applied to dermatology/cosmetology,” *Journal of Biomedical Imaging*, vol. 2013, p. 26, 2013.
- [78] J. Canny, “A computational approach to edge detection,” *IEEE Transactions on pattern analysis and machine intelligence*, no. 6, pp. 679–698, 1986.
- [79] E. R. Dougherty, “An introduction to morphological image processing,” *Tutorial texts in optical engineering*, 1992.
- [80] H. R. Kang, *Digital color halftoning*. SPIE press, 1999.
- [81] J. S. Viggiano, “Modeling the color of multi-colored halftones,” in *Proc. TAGA*, vol. 42, 1990, pp. 44–62.
- [82] M. Hébert and R. Hersch, “Review of spectral reflectance models for halftone prints: Principles, Calibration, and prediction accuracy,” *Color Res. Appl.*, vol. 40, no. 4, pp. 383–397, 2015.
- [83] M. Hébert and R. D. Hersch, “Yule–Nielsen based recto–verso color halftone transmittance prediction model,” *Applied Optics*, vol. 50, no. 4, pp. 519–525, 2011.
- [84] R. D. Hersch and M. Hébert, “Base models for color halftone reproduction,” *Handbook of Digital Imaging*, 2015.
- [85] J. Machizaud and M. Hébert, “Spectral reflectance and transmittance prediction model for stacked transparency and paper both printed with halftone colors,” *JOSA A*, vol. 29, no. 8, pp. 1537–1548, 2012.
- [86] T. Baar, M. Shahpaski, and M. V. O. Segovia, “Image ghosting reduction in lenticular relief prints,” in *IS&T/SPIE Electronic Imaging*. International Society for Optics and Photonics, 2014, pp. 90180N–90180N.
- [87] L. Nadar, R. Sayah, F. Vocanson, N. Crespo-Monteiro, A. Boukenter, S. Sao Joao, and N. Destouches, “Influence of reduction processes on the colour and photochromism of amorphous mesoporous tio₂ thin films loaded with a silver salt,” *Photochemical & Photobiological Sciences*, vol. 10, no. 11, pp. 1810–1816, 2011.
- [88] L. Nadar, N. Destouches, N. Crespo-Monteiro, R. Sayah, F. Vocanson, S. Reynaud, Y. Lefkir, and B. Capoen, “Multicolor photochromism of silver-containing mesoporous films of amorphous or anatase tio₂,” *Journal of nanoparticle research*, vol. 15, no. 11, pp. 1–10, 2013.
- [89] R. Rossier and R. D. Hersch, “Hiding patterns with daylight fluorescent inks,” in *Color and Imaging Conference*, vol. 2011, no. 1. Society for Imaging Science and Technology, 2011, pp. 223–228.

-
- [90] R. D. Hersch, P. Donzé, and S. Chosson, “Color images visible under uv light,” in *ACM Transactions on Graphics (TOG)*, vol. 26, no. 3. ACM, 2007, p. 75.
- [91] R. D. Hersch, F. Collaud, and P. Emmel, “Reproducing color images with embedded metallic patterns,” in *ACM Transactions on Graphics (TOG)*, vol. 22, no. 3. ACM, 2003, pp. 427–434.
- [92] S. Mazauric, M. Hébert, and T. Fournel, “Model-based design of recto-verso prints displaying different images according to the illuminated face,” in *Color and Imaging Conference*, vol. 2015, no. 1. Society for Imaging Science and Technology, 2015, pp. 7–11.
- [93] J. Machizaud and M. Hébert, “Spectral transmittance model for stacks of transparencies printed with halftone colors,” in *IS&T/SPIE Electronic Imaging*. International Society for Optics and Photonics, 2012, pp. 829212–829212.
- [94] H. Kipphan, *Handbook of print media: technologies and production methods*. Springer Science & Business Media, 2001.
- [95] “Sculptor Thomasine Giesecke. Accessed on 2016-07-12.” [Online]. Available: <http://www.thomasinegiesecke.com/>